



THE UNIVERSITY
of ADELAIDE

Diagnostics of particles and droplets
under high-flux radiation

Wanxia Zhao

School of Chemical Engineering and Advanced Materials

A thesis submitted for the degree of Doctor of Philosophy at
The University of Adelaide

February 2021

Table of Contents

Abstract	I
Declaration.....	III
Acknowledgments	IV
Chapter 1 Introduction	1
1.1 Motivations	2
1.2 Aims	5
1.3 Outline of the thesis	6
References	8
Chapter 2 Literature Review	11
2.1 Radiation heating	12
2.1.1 Electric-arc lamps	12
2.1.2 Fiber-optic based laser heating systems.....	14
2.2 Target temperature measurement under high-flux radiation.....	17
2.2.1 Laser-induced phosphorescence using phosphors	18
2.2.2 Infrared thermometry	21
2.3 Research targets used in the application of high-flux radiation.....	24
2.3.1 Phosphor aggregates	24
2.3.2 Biomass tablets	27
2.3.3 Hydrochar slurry	29
2.3.4 Solid particles used in solar particle receivers.....	30
2.4 Levitation systems.....	33
2.4.1 Electrodynamic (ED) balances	33
2.4.2 Acoustic levitators using acoustic force	34
2.5 Research gaps.....	36
References	38

Chapter 3 Temperature Imaging of Mobile BaMgAl ₁₀ O ₁₇ :Eu Phosphor Aggregates under High Radiation Flux.....	50
Chapter 4 Optical Properties and Scattering Distribution of Thermographic Phosphor Suspensions.....	61
Chapter 5 Contactless Thermal Diagnostics of Acoustically Levitated Biomass under Uniform High Flux Radiation.....	92
Chapter 6 Development and Characterization of a Grape Marc Hydrochar Slurry Fuel	99
Chapter 7 Emissivity and Absorption Function Measurements of Al ₂ O ₃ and SiC Particles at Elevated Temperature for the Utilization in Concentrated Solar Receivers.....	110
Chapter 8 Conclusions and Future Works	121
8.1 Conclusions	122
8.2 Future works.....	126
Appendix.....	129

Abstract

Radiation heating is important in many engineering processes including gasification, fuel production, materials processing, and concentrated radiation collection. Its high efficiency enables it to consistently drive thermal reactions operated under extreme conditions. High-flux radiation delivers energy directly to the target bodies and improves heat transfer efficiency. Traditional radiation simulators, which have been normally used to radiatively heat the targets, usually have some major difficulties with the power control and projection. Therefore, this thesis utilizes a multi-diode laser system to provide a uniform and well-controlled radiation flux up to 28.87 MW/m^2 . It serves to demonstrate the radiation heating of particles, aggregates, tablets, and droplets. Laser, optical, and conventional techniques are applied to reliably record the temperature changes in the target bodies, determine the thermal characteristics such as heating rates, and investigate the heat transfer process and optical properties of the selected targets. According to the researched targets, this thesis is divided into four parts:

In the first part, the well-controlled radiation was employed on two types of phosphors, $\text{BaMg}_2\text{Al}_{10}\text{O}_{17}:\text{Eu}$ (BAM) and $\text{ZnO}:\text{Zn}$, to investigate temperature imaging of mobile aggregates under high fluxes and to evaluate the radiation trapping at room temperature. For temperature imaging, the real-time temperatures of fluidized BAM aggregates were recorded using the planar laser-induced phosphorescence technique. The maximum temperature of an aggregate was 1063 K, and the largest average temperature was 723 K. For non-thermal radiation trapping, the optical properties of BAM and $\text{ZnO}:\text{Zn}$ were derived from the developed collision-based Monte Carlo ray-tracing model. The extinction coefficient of $\text{ZnO}:\text{Zn}$ was 50% smaller than that of BAM. Radiation trapping

was predicted in the direction of the radiation path. For ZnO:Zn, 70% of flux was scattered when the distance increases to 0.5, while for BAM, the distance was 0.15.

In the second part, the high-flux radiation was applied on biomass tablets to investigate the thermal processes and improve the efficiency of biomass utilization. To avoid any physical contact, each biomass tablet was suspended using a home-built acoustic levitator. Three different thermal processes, *i.e.*, the initial fast-heating process within 1 s, the secondary slow-heating process from 1 to 3 s, and the final ignition starting at 3 s, were identified from the time-resolved temperature profiles. The ignition temperature was determined around 430 to 450 K.

In the third part, the high-flux radiation was tested on acoustically levitated liquid droplets. A newly developed hydrochar slurry fuel was proved to be pseudo-plastic and desirable for potential liquid fuel applications. The maximum heating rate of a single 50 wt.% slurry droplet within the first 0.15 s was measured above 400 K/s. The maximum surface ignition time of suspended and irradiated hydrochar slurry droplets was 0.37 ± 0.01 s, and the surface ignition temperature was 375 ± 15 K, independent of heat flux.

In the fourth part, the high-flux radiation was employed in the measurement of emissivity and absorption function of two solid particles, Al₂O₃ and SiC, at elevated temperatures. The values of emissivity were determined to be 0.75 ± 0.015 for Al₂O₃ and 0.92 ± 0.012 for SiC from 300 to 1200 K. The absorption function of Al₂O₃ at 910 nm was nonlinearly increased with the temperature, while that of SiC dropped slightly. The modeling results of micro-sized particles suggest that the temperature rise-time of the two materials have significantly different dependencies on the radiation flux.

The outcomes of this thesis will benefit studies done on heat transfer, optical properties, and thermal processing in the energy field, especially those high-temperature reactions associated with high-flux radiation heating.

Declaration

I certify that this work contains no material which has been accepted for the award of any other degree or diploma in my name in any university or other tertiary institution and, to the best of my knowledge and belief, contains no material previously published or written by another person, except where due reference has been made in the text. In addition, I certify that no part of this work will, in the future, be used in a submission in my name for any other degree or diploma in any university or other tertiary institution without the prior approval of the University of Adelaide and where applicable, any partner institution responsible for the joint award of this degree.

The author acknowledges that copyright of published works contained within this thesis resides with the copyright holder(s) of those works.

I give permission for the digital version of my thesis to be made available on the web, via the University's digital research repository, the Library Search and also through web search engines, unless permission has been granted by the University to restrict access for a period of time.

I acknowledge the support I have received for my research through the provision of an Australian Government Research Training Program Scholarship.

Signature:

Date: 2/02/2021

Acknowledgments

I would like to take this opportunity to thank all the people who helped and supported me during my four-year Doctor of Philosophy study at the University of Adelaide. It is their impressive kindness and advice that made this thesis possible.

First and foremost, I would like to express my deepest gratitude to my principal supervisor Associate Professor Zeyad Alwahabi and co-supervisor Dr. Philip Kwong for their valuable guidance, patience, and encouragement in every stage of my study. Their effective suggestions, shrewd comments, and vigorous academic observation have enlightened me not only in this thesis but also in my future study and career.

I shall extend my thanks to Professor Gus Nathan, Dr. Zhiwei Sun, Dr. Kimberly Kueh in our research group, who has given me generous help and suggestions in my experiments and publications.

I would also like to thank Dr. Md Abdul Wakil, Dr. Safa Algoraini as well as other research group members from the School of Chemical Engineering and Centre of Energy Technology for their help and support for my work. They offer me not only useful discussions and suggestions but also valuable friendships.

Last but not least, my greatest gratitude must go to Dad and Mum, and my *fiancé*, Dr. Chaochen Xu. Thank you for your constant encouragement and endless love throughout my life.

Chapter 1

Introduction

1.1 Motivations

Demand for energy-intensive processes has grown considerably in recent times to meet the requirements of economic development. A wide range of industries from transportation to production and material processing rely on energy-intensive processes and this reliance can only increase due to the growth of the world's population and the global economy.¹ Of these energy-intensive processes, a large amount of external energy is required to provide high-temperature process heat and enable the reactor to reach high operating temperatures.² Currently, most such processes rely heavily on the utilization of conventional energy sources, such as fossil fuels, which have the disadvantages of high cost and environmental pollution. Combustion of traditional fossil fuels is also the major source of greenhouse gases and contributes around 41% to CO₂ emissions.³

To overcome this problem, a possible solution is to employ radiation as a heat source to drive chemical reactions that operate at extreme conditions in terms of temperature and radiative flux, i.e. temperatures > 1000 K and average radiative fluxes > 100 kW/m².⁴ This renewable option has been considered for many decades and proven to be a feasible and environmental-friendly strategy of driving high-temperature reactions. Radiation heating can provide a non-contact mode of heat transfer, and compared with convective heat transfer, radiation heating is more effective at high temperatures because it scales with the fourth power of temperature difference instead of the first power. The advantages of using radiation as a heating source, such as concentrating solar radiation, in engineering thermal processes are summarized below:⁵

- The high heating rates are easy to achieve.
- Products are not contaminated by the by-products from conventional fuel combustion.
- The discharge of pollutants to the environment is reduced.
- The need for energy-intensive processing of pure oxygen is eliminated.

While radiation heating has traditionally been more expensive than conventional flames, it is still receiving growing interest in the context of the need to curtail CO₂ emissions because radiation heating is compatible with renewable energy. The application of high-flux radiation heating offers a great opportunity for future sustainable energy development. Radiation heating is now the dominant mode of heat transfer in many engineering processes related to the area of fuel and energy, especially those associated with time-dependent heat transfer during flow and reaction. Such processes include biomass gasification,⁶⁻⁷ combustion,⁸ fuel production,⁹ materials processing,¹⁰⁻¹² and solar receivers.¹³⁻¹⁵

In the literature, most of the reported applications of high-flux radiation are focused on thermochemical processes. According to Gallo *et al.*,¹⁶ to maximize efficiency the optimum temperature for thermochemical reactions ranges between 1000 to 2500 K with radiation flux between 1 to 20 MW/m². For example, Nikulshina *et al.*¹⁷ presented a design of a high-flux reactor for a thermochemical process of CaO-carbonation and CaCO₃-calcination cycles to continuously remove CO₂ from ambient air. They used a fluidized bed reactor to perform the reaction at 1073 to 1148 K, with reacting particles directly heated by high-flux radiation.

Another important example is the gasification of carbonaceous materials, e.g. coal, biomass, coke, etc., to synthesis syngas. In such processes, carbonaceous feedstocks are heated with steam and/or CO₂ using concentrated radiation. The resulting syngas can be directly used for combustion or be transformed into liquid fuels for more economical applications.¹⁸ With avoiding the conductive heat transport through the reactor walls, the utilization of high-flux radiation can transfer energy directly to the reaction site by irradiation of carbonaceous feedstocks and improve heat transfer efficiency. Epstein *et al.*¹⁹ reviewed different gasifiers and studied the reactor design for the gasification of biomass, oil, and coal. They concluded that high-flux radiation-assisted gasification was a promising approach to

process carbonaceous materials and its cost was in the same range as traditional gasification using fossil fuels.

Radiation heating is widely applied in the research on concentrated radiation receivers for the development of renewable energy systems. For example, solar receivers collect high-flux concentrated radiation via parabolic reflectors and convert the radiation into thermal energy or chemical energy, which are further transferred into electrical energy. The temperature inside the reactor can be over 2000 K, and the high quality of thermal energy is achieved because the solar receiver could be assumed as a blackbody.²⁰ Sandia National Laboratories (SNL) has studied solar receivers for years.¹⁵ Their recent researches reported a new generation of the solar receiver,²¹ which could increase the particle temperature from 900 K to 1200 K under the high-flux radiation of 800 kW/m². The high efficiency of power conversion was achieved at 70%. Because of the high temperature and high flux achieved inside the solar receiver, it has been used in various applications, for instance, the production of hydrogen, treatment of waste materials, and production of new energy.²⁰

More recently, radiation heating has been employed in materials processing for substituting fossil fuel and electrical energy. These industrial processes include the melting of glass for manufacture,²² production of lime from limestone,²³ and purification of zinc from its oxidic materials.²⁴ For example, Ahmad *et al.*²² studied the process of melting glass using high-flux radiation. The soda-lime-silica glass sample was successfully melted when maintained at a temperature around 1750 K for an hour.

It is evident that radiation has been considered sufficiently mature as the heating source in wide heat-related flows and reactions. Applying radiation heating is essential and significant in various engineering processes for heat transfer and thermal diagnostics. Delivering high flux radiation into a small target area is also important to investigate the heat

transfer of small objectives. Therefore, this thesis utilized a multi-diode laser system to provide a uniform and well-controlled radiation flux up to 28.87 MW/m^2 in a focal spot area with a diameter of 10 mm. This heating source was employed to investigate the radiation heating of particles, aggregates, and droplets, whose sizes are less than 5 mm. Laser, optical and conventional techniques were applied to reliably record the temperature change of the target bodies.

1.2 Aims

This thesis aims to demonstrate the application of high-flux radiation heating to different heat-related engineering processes for small target objects ($< 5 \text{ mm}$). The high-flux heating source was used to evaluate the thermal characteristics, heat transfer, and optical properties of particles, tablets, aggregates, and droplets. The specific investigation aims include:

- Perform *in-situ* temperature imaging of fluidized $\text{BaMg}_2\text{Al}_{10}\text{O}_{17}:\text{Eu}$ (BAM) aggregates.
- Evaluate the radiation trapping effect of BAM and $\text{ZnO}:\text{Zn}$ phosphors.
- Diagnose the temperature and thermal processes of acoustically levitated biomass tablets.
- Investigate combustion behaviors, including heating rates and ignition temperatures, of newly developed hydrochar slurry droplets.
- Determine the values of emissivity and absorption functions of solid particles used in solar particle receivers, i.e. Al_2O_3 and SiC particles.

The outcomes of this thesis will benefit studies done on heat transfer, optical properties, and thermal processing in the energy field, especially those high-temperature reactions associated with high-flux radiation heating.

1.3 Outline of the thesis

This thesis is organized as follows:

Chapter 1 Here the research background is introduced, followed by the research aims and the outline of the thesis.

Chapter 2 In this chapter, a literature review is presented, and the research gaps are defined. Different heating sources are first reviewed, followed by two temperature measurement techniques, namely laser-induced phosphorescence (LIP) and infrared thermometry, to identify suitable methods for non-intrusive measurement under radiation conditions. Four target objectives used in the application of high-flux radiation are systematically discussed to identify their research gaps in each work. Also, contactless levitation systems are reviewed to eliminate undesired conductive heat transfer in the study involving radiation heating.

Chapter 3 This chapter introduces a non-intrusively temperature measurement of mobile phosphors particles conducted in multiphase flow using a laser diagnostic method with high resolution. In this work, the particles were heated under well-characterized laser radiation to reach high temperature within a short time in a fluidized bed. Representative results are shown and discussed by highlighting the spatially and temporally resolved particle temperature images under different radiation fluxes.

Chapter 4 In this chapter, the phosphor particles were mixed homogeneously with transparent epoxy resin to study their radiation trapping. The samples were prepared at different loadings. Optical properties are determined for sample porosities between 0.972 and 0.995 and thicknesses ranging between 0.13 to 1.52 mm. The light scattering and wavelength study was conducted at 6 forward angles and 5 backward angles, together with 4 wavelengths, specifically 532, 635, 808, and 980 nm. The scattering properties of phosphor particles were determined using combined experimental and numerical methods.

Chapter 5 For this chapter, contactless thermal diagnostic of acoustically levitated biomass was done under uniform high flux radiation. To avoid potential and complicated heat conduction between biomass samples and the contact system, an innovative contactless apparatus was developed to levitate biomass particles by acoustic force. Several key thermal parameters of the biomass are reported in this chapter, including the time-resolved heating rate and the ignition temperature under high fluxes.

Chapter 6 This chapter discusses a new hydrochar slurry prepared from hydrothermal carbonization of grape marc. The high-flux radiation was used to heat a single droplet of hydrochar slurry to determine its temperatures, heating rates, and combustion behaviors. The acoustic levitation system, which was previously used in research on biomass combustion, was also employed to suspend the slurry droplet without any physical contact.

Chapter 7 In this chapter, the values of emissivity and absorption functions of radiatively heated solid particles used in solar receivers, i.e. aluminum oxide (Al_2O_3 , ~ 95% purity) and silica carbide (SiC, ~ 99% purity), were measured at elevated temperatures up to 1200 K. The emissivity and absorption function were determined according to a heat transfer model of a single particle in the presence of high radiation. Furthermore, the temperature rise-time and equilibrium temperature of micro-sized (200 – 1000 μm) particles were evaluated.

Chapter 8 This is the final chapter of the thesis, and it presents the results and conclusion of what this research set out to do, followed by the suggested future extensions.

References

1. Koepf, E.; Alxneit, I.; Wieckert, C.; Meier, A., A review of high temperature solar driven reactor technology: 25 years of experience in research and development at the Paul Scherrer Institute. *Applied Energy* **2017**, *188*, 620-651.
2. Sharma, A.; Pareek, V.; Zhang, D., Biomass pyrolysis—A review of modelling, process parameters and catalytic studies. *Renewable and Sustainable Energy Reviews* **2015**, *50*, 1081-1096.
3. Song, C., Global challenges and strategies for control, conversion and utilization of CO₂ for sustainable development involving energy, catalysis, adsorption and chemical processing. *Catalysis Today* **2006**, *115* (1–4), 2-32.
4. Levêque, G.; Bader, R.; Lipiński, W.; Haussener, S., High-flux optical systems for solar thermochemistry. *Solar Energy* **2017**, *156*, 133-148.
5. Z'Graggen, A.; Steinfeld, A., Heat and mass transfer analysis of a suspension of reacting particles subjected to concentrated solar radiation – Application to the steam-gasification of carbonaceous materials. *International Journal of Heat and Mass Transfer* **2009**, *52* (1), 385-395.
6. Nzihou, A.; Flamant, G.; Stanmore, B., Synthetic fuels from biomass using concentrated solar energy – A review. *Energy* **2012**, *42* (1), 121-131.
7. Piatkowski, N.; Wieckert, C.; Weimer, A. W.; Steinfeld, A., Solar-driven gasification of carbonaceous feedstock-a review. *Energy & Environmental Science* **2011**, *4* (1), 73-82.
8. Nathan, G. J.; Jafarian, M.; Dally, B. B.; Saw, W. L.; Ashman, P. J.; Hu, E.; Steinfeld, A., Solar thermal hybrids for combustion power plant: A growing opportunity. *Progress in Energy and Combustion Science* **2018**, *64*, 4-28.
9. Hirsch, D.; Epstein, M.; Steinfeld, A., The solar thermal decarbonization of natural gas. *International Journal of Hydrogen Energy* **2001**, *26* (10), 1023-1033.

10. Lipiński, W.; Davidson, J. H.; Haussener, S.; Klausner, J. F.; Mehdizadeh, A. M.; Petrasch, J.; Steinfeld, A.; Venstrom, L., Review of Heat Transfer Research for Solar Thermochemical Applications. *Journal of Thermal Science and Engineering Applications* **2013**, 5 (2), 021005-021005-14.
11. Schaffner, B.; Hoffelner, W.; Sun, H.; Steinfeld, A., Recycling of Hazardous Solid Waste Material Using High-Temperature Solar Process Heat. 1. Thermodynamic Analysis. *Environmental Science & Technology* **2000**, 34 (19), 4177-4184.
12. Meier, A.; Bonaldi, E.; Cella, G. M.; Lipinski, W.; Wuillemin, D., Solar chemical reactor technology for industrial production of lime. *Solar Energy* **2006**, 80 (10), 1355-1362.
13. Maag, G.; Lipiński, W.; Steinfeld, A., Particle–gas reacting flow under concentrated solar irradiation. *International Journal of Heat and Mass Transfer* **2009**, 52 (21), 4997-5004.
14. Schunk, L. O.; Lipiński, W.; Steinfeld, A., Heat transfer model of a solar receiver-reactor for the thermal dissociation of ZnO—Experimental validation at 10kW and scale-up to 1MW. *Chemical Engineering Journal* **2009**, 150 (2), 502-508.
15. Ho, C. K.; Iverson, B. D., Review of high-temperature central receiver designs for concentrating solar power. *Renewable and Sustainable Energy Reviews* **2014**, 29, 835-846.
16. Gallo, A.; Marzo, A.; Fuentealba, E.; Alonso, E., High flux solar simulators for concentrated solar thermal research: A review. *Renewable and Sustainable Energy Reviews* **2017**, 77, 1385-1402.
17. Nikulshina, V.; Gebald, C.; Steinfeld, A., CO₂ capture from atmospheric air via consecutive CaO-carbonation and CaCO₃-calcination cycles in a fluidized-bed solar reactor. *Chemical Engineering Journal* **2009**, 146 (2), 244-248.
18. Loutzenhiser, P. G.; Muroyama, A. P., A review of the state-of-the-art in solar-driven gasification processes with carbonaceous materials. *Solar Energy* **2017**, 156, 93-100.

19. Epstein, M.; Spiewak, I.; Funken, K. H.; Ortner, J. In *Review of the technology for solar gasification of carbonaceous materials*, International Solar Energy Conference, San Francisco, CA, The ASME/JSME/JSES: San Francisco, CA, 1994; pp 79-91.
20. Wang, M.; Siddiqui, K., The impact of geometrical parameters on the thermal performance of a solar receiver of dish-type concentrated solar energy system. *Renewable Energy* **2010**, *35* (11), 2501-2513.
21. Siegel, N. P.; Ho, C. K.; Khalsa, S. S.; Kolb, G. J., Development and Evaluation of a Prototype Solid Particle Receiver: On-Sun Testing and Model Validation. *Journal of Solar Energy Engineering* **2010**, *132* (2), 021008.
22. Ahmad, S. Q. S.; Hand, R. J.; Wieckert, C., Use of concentrated radiation for solar powered glass melting experiments. *Solar Energy* **2014**, *109*, 174-182.
23. Meier, A.; Bonaldi, E.; Cella, G. M.; Lipinski, W., Multitube Rotary Kiln for the Industrial Solar Production of Lime. *Journal of Solar Energy Engineering* **2005**, *127* (3), 386-395.
24. Tzouganatos, N.; Matter, R.; Wieckert, C.; Antrekowitsch, J.; Gamroth, M.; Steinfeld, A., Thermal Recycling of Waelz Oxide Using Concentrated Solar Energy. *JOM* **2013**, *65* (12), 1733-1743.

Chapter 2

Literature Review

2.1 Radiation heating

A suitable radiation heating source is critical in radiative heat transfer studies. The heating source is required to provide uniform illumination, stable flux, satisfied collimation conditions, and high spectral quality.¹ Radiation heating has been used to drive a range of thermal reactions, which require high-temperature heat as process heat. For example, the material processing of calcination operates at the temperature of 1200 K, dry-gasification requires the temperature above 1200 K, and superheating of heat transfer fluids for power production generally runs between 700 to 1400 K.² To achieve efficient and intensive heating, the desired heating source is expected to produce an irradiance output greater than 700 W/m² on the target place with a deviation within the range of ± 50 W/m².³ As well, although thermal applications require lower sensitivity to the spectrum of heating source, high spectral quality is still necessary because the absorption, reflectance, and transmittance of target materials may vary with the incident radiation.⁴ Recently, various devices have been investigated and developed to deliver high-flux thermal radiation with high spectral quality to the target place for high-temperature thermal applications.

2.1.1 Electric-arc lamps

High-power electric-arc lamps are often used as the radiation source because they can deliver continuous and intensive thermal radiation. To date, two types of lamps have been employed and these are the metal halide and xenon arc lamps.

In metal halide lamps, the electric-arc is generated by a mixture of metal halide compounds and vaporized mercury under a pressure of 10 to 35 bar.³ Metal halide lamps have been widely selected by researchers because they have the advantages of high efficiency, long lifetime, and high spectral quality.⁵⁻⁷ For example, Codd *et al.*⁸ built and characterized a low-cost and high flux solar simulator to study the heat absorption behaviors

of molten salts under high-flux radiation. In their design, seven 1500 W metal halide lamps were employed as the light source to simulate the output of real solar radiation. This device could produce peak fluxes of approximately 60 kW/m^2 at an output aperture of 38 cm in diameter. Elsewhere, Kim *et al.*⁹ used a solar simulator, one which consisted of 35 metal halide lamps, to evaluate the performance of their flat plate solar collector through the heat transfer analysis. In their work, each lamp was equipped with a rotating reflector to deliver collimated radiation. The maximum intensity was estimated at 1.2 kW/m^2 .

The xenon arc lamp is a kind of gas discharge lamp, which generates the electric-arc by transmitting electricity through ionized xenon gas under high pressure.¹⁰ Compared with the radiation sources using metal halide lamps, xenon arc lamps are more costly, however, xenon lamps generate a shorter arc than metal halide lamps, which gives xenon lamps the ability to generate a higher flux output than metal halide lamps.^{3, 11} For example, a high-power xenon arc lamp (up to 30-kW electrical input) was designed at Lawrence Berkeley Laboratory and employed to investigate fast thermal reductions of metal oxides which were driven by direct irradiation.¹² A xenon lamp was placed around the focus of an aluminum-coated ellipsoidal mirror with a diameter of 80 cm. Their device could deliver continuous power of about 3 kW at the focal plane with peak fluxes up to 16 MW/m^2 . Additionally, Li *et al.*¹⁰ reported a high-flux radiation heating device containing seven 6 kW xenon short-arc lamps representing the spectrum of solar radiation. These lamps were adjusted to focus their hot spot into a line and provided a total flux distribution with approximately 100 mm in the horizontal width and 300 mm in the vertical direction. The peak flux was obtained at around 1.4 MW/m^2 . More recently, Li *et al.*¹³ constructed and characterized a multi-source high-flux solar simulator, which consisted seven 4-kWe xenon short-arc lamps, as a lab-scale high-temperature solar reactors. In their design, the optical alignment of the xenon arc lamps could be precisely adjusted. The measured peak flux of the solar simulator was 7.74 MW/m^2 ,

and the electricity-to-target transfer efficiency in a target spot with 60 mm diameter was 29.6%.

However, both types of these electric-arc lamps suffer the disadvantages that their spectra are further from the real solar spectrum. They usually produce radiation at visible wavelengths with additional power in the infrared and ultraviolet ranges.¹² The spectra of different lamps have been compared by Tawfik *et al.*³ based on the measurements of emitted irradiance distributions. They identified the differences between the spectra of lamps and the standard solar spectrum (AM1.5). Compared with real sunlight, the artificial xenon light has a strong spectrum intensity in the range between 800 and 1000 nm and extra spectra in the range of far ultraviolet. Metal halide lamps have a good quality spectrum distribution of less than 900 nm but present a discrepancy with the solar spectrum when the range of the wavelength is longer than 900 nm. Moreover, the lamps cannot provide a true point heat source.¹⁴ Consequently, it is difficult to get a specific flux distribution of the radiation source or to perform any corrections for other phenomena, like attenuation in flux intensity. Additionally, conventional xenon arc lamps usually have the problem of “hot-spots”, which is caused by radiation overlap. These “hot-spots” might damage the reactors when the heat flux is high.¹⁴

2.1.2 Fiber-optic based laser heating systems

Fiber lasers can provide coherence radiation with specified wavelengths and well-defined spectral distributions. In thermal applications, heating radiation can be conveniently delivered through an optical fiber by coupling the output of laser diodes. Fiber-coupled diode lasers have the advantages of high brightness, low-temperature dependence, high optical efficiency, high stability, and are easy to control.¹⁵ The light from the fiber has a homogenized intensity profile and well-characterized beam quality. Each diode laser module is easy to be replaced without changing the optical alignment of the radiation beam, which

is convenient in many cases. The heat flux can be adjusted easily by changing the laser current and delivered to a small target point. Besides, fiber-coupled devices can potentially be combined with other fiber-optic components.

Nowadays, high-power diode lasers can deliver watt-level output power as every single emitter has good beam quality and achieves efficiencies of more than 70%, while a diode laser bar consisting of several emitters can provide a power level up to tens of watts.¹⁶ For example, Jaramillo *et al.*¹⁷ did a theoretical study on transferring concentrated solar radiation using optical fibers. They found the equation for heat radiation and conduction through fibers and determined that the heat flux was 26 W at the end of 10 m fiber with the transfer efficiency of 88 %. Liang *et al.*¹⁸ built two flexible fiber-optic bundles to deliver the radiation energy of 200 W. In their design, each bundle contained 19 optical fibers with 1.5 mm in diameter. The transmission efficiency of each bundle amounted to 70%. More recently, Vijayakumar *et al.*¹⁶ demonstrated spectral beam combining of a 980 nm tapered diode laser bar, which consisted of 12 single emitters. At the operating current of 30 A, the laser bar produced a power level of 9.3 W. Additionally, Werner *et al.*¹⁵ reported a high power fiber-coupled diode laser module where each single diode laser could provide 60 W output power. The spectrum had a maximum absorption intensity at 976 nm and the optical efficiency achieved was more than 80%. Furthermore, the cost reduction in light-emitting diodes makes the fiber laser competitive with other radiation heating sources, such as electric-arc lamps.¹⁴

In our work, a new and efficient 3.168 kW radiation source coupled to a fiber optical head was introduced. The heating was supplied by a high radiation multi-diode laser system which provides well-characterized high-flux radiation up the power level of MW. Figure 2.1 below depicts a schematic diagram of the radiation source.

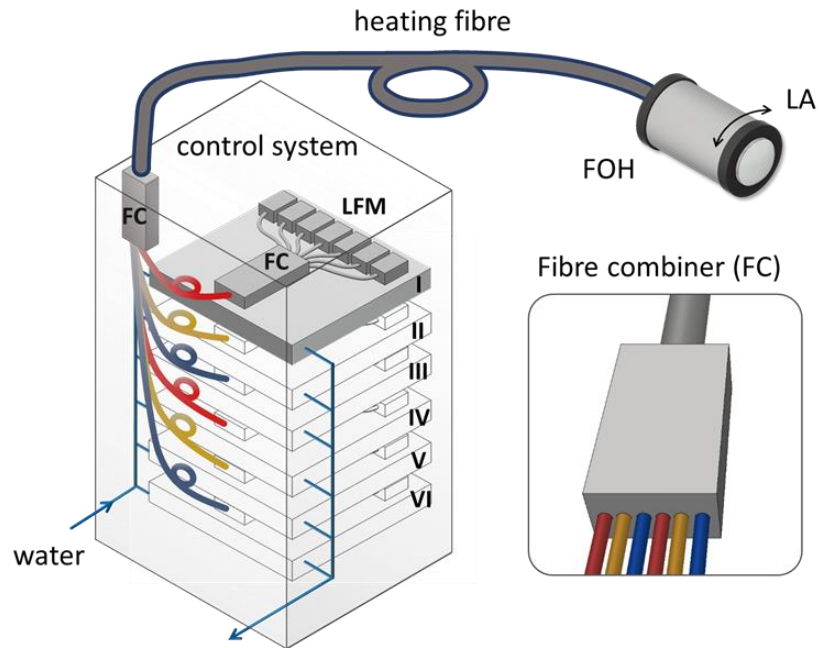


Figure 2.1: Schematic diagram of the high radiation multi-diode laser system. The system contained 6 groups (I-VI) of 7 individual Laser Fiber Modules (LFM). FOH: fiber optical head. LA: lens adjustment.

The system contained a total of 42 lasers, which are 41 fiber-coupled diode laser modules (Nlight, Model e06.0900915200) allocated in 6 group layers (I-VI) and one pilot guide laser.¹⁴ The 7 diode laser modules on each layer were spliced into a fiber combiner with a splicing efficiency higher than 99%. Then, the outputs of the combiner from 6 groups were combined into another fiber combiner with a 1500 μm output heating fiber, which could provide a focused radiation region with a 10.5 mm diameter at 500 mm away from the fiber optical head. The peak wavelength of the laser system varied slightly from 904.0 nm to 918.5 nm. The device delivers high output power with an excellent beam profile and provides a uniform heating region on the target place. The focused radiation had an intensive flux of up to 32.8 MW/m^2 , i.e. $\sim 30,000$ suns.

In this thesis, this high radiation multi-diode laser system was employed as a high-flux heating source to study the following: *in-situ* temperature of fluidized phosphor aggregates in **Chapter 3**; thermal behaviors of biomass tablets in **Chapter 5**; hydrochar slurry droplets in **Chapter 6**; and optical properties of solid particles used in solar thermal receivers in **Chapter 7**. Added to the analyses conducted in this thesis, the non-thermal radiation trapping effect and radiation scattering distribution of phosphors at room temperature were investigated in **Chapter 4**.

2.2 Target temperature measurement under high-flux radiation

A key to advancing our understanding of radiation heat transfer in energy-related systems is the capacity to provide an accurate and well-resolved measurement of temperature, both spatially and temporally. Traditional methods widely rely on the measurement devices such as thermocouples, Langmuir probes, resistance temperature detectors, and thermistors.¹⁹ However, such devices require direct physical contact with measured objects, which limits their applicability in the temperature measurement of moving surfaces, for instance, particles inside a fluidized reactor. Any contact between the temperature sensor and heating radiation always results in an undesired temperature increase. Regarding these points, numerous non-intrusive diagnostic techniques are emerging with strong potential to achieve contactless and *in situ* temperature measurements in radiation-heated reactors.²⁰⁻²² One of these techniques is laser-induced phosphorescence (LIP), which utilizes thermographic phosphors (TPs) to offer a non-invasive temperature measurement for both static and moving surfaces with high accuracy. Another available technique is infrared thermography. It is a process of using an infrared (IR) camera to spatially quantify the thermal field on a measured surface with quick response time and high sensitivity.

2.2.1 Laser-induced phosphorescence using phosphors

The principle of LIP is based on the luminescence properties of phosphors. Phosphors mostly exist as a powder and different phosphors are suitable for various temperature ranges. After laser excitation, they will release electrons from the excited state to the ground state. Meanwhile, the long afterglow is emitted, and this is known as phosphorescence. Unlike fast fluorescence, phosphorescence lasts longer due to the forbidden transitions from triplet-to-singlet states, while fluorescence is only caused by singlet-to-singlet transitions.²³ Figure 2.2 illustrates the formation process of phosphorescence comparing with fluorescence following light absorption, where S_0 is the ground electronic state, S_1 is the first excited singlet state, and T_1 is the first excited triplet state. Generally, phosphors can offer the precision surface thermometry over the broad temperature range up to more than 1900 K.²⁴ The calibration of phosphors needs to be done within their specified temperature range before measuring the unknown temperature in an experiment.²⁵

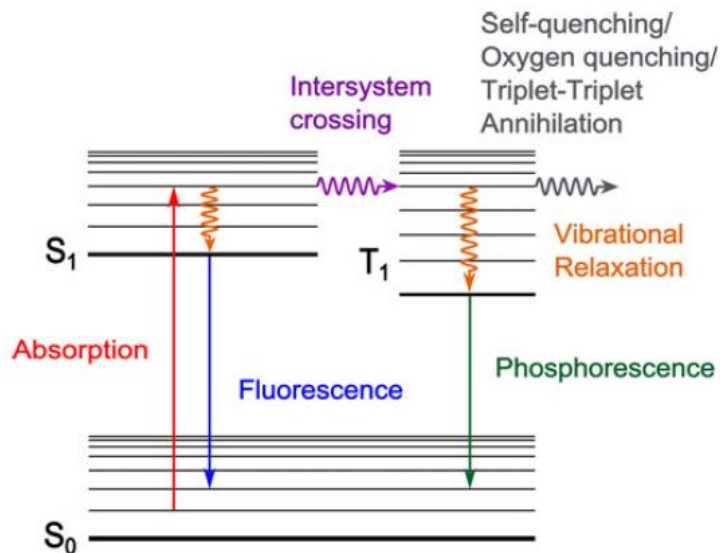


Figure 2.2: Formation process of fluorescence and phosphorescence following light absorption.²³

Compared with other non-invasive particle temperature measurement techniques identified to date, LIP using phosphors can provide more accurate results due to its low sensitivity of the particle surface properties to temperature and low interferences from

chemiluminescence or scattering light.²⁶ For example, pyrometry is another method that can provide non-invasively two-dimensional particle temperature measurement. However, its accuracy is affected by the emissivity of the target surface and interfering light from surrounding objects or backgrounds. Pyrometry is unable to differentiate the temperature signal was from the particle surface only or was interfered with the surrounding noises.²⁷⁻²⁸ To compare the characteristics of different non-invasive temperature measurements using laser techniques, Table 2.1 below summarizes the advantages and disadvantages for each of them.

Table 2.1: Advantages and disadvantages of different non-invasive temperature measurement methods.^{19, 29-30}

Techniques	Advantages	Disadvantages
Temperature-sensitive coating, e.g. thermal paints	non-contact	- Limitation of temperature <380 K - Inappropriate for time-resolved measurements: irreversible color change at the peak temperature
Pyrometry	Enable two-dimensional imaging	Poor accuracy due to: - emissivity of particle surface - interfering light
laser-induced phosphorescence (LIP)	Suitable for both turbulent and laminar flows Low sensitivity to the background Suitable in high-temperature conditions	- low signal intensity and strong blackbody radiation effect at extremely high temperatures (> 1700 K)

The emission of phosphors will change along with the increasing temperature. Since the emission properties from different phosphors are different, mainly, two properties can be exploited to extract temperature information in phosphor thermometry. These are lifetime of the phosphorescence decay and intensity ratio between two emission lines in the phosphorescence spectrum. Both methods are can be done in one-point and 2D measurement. The lifetime method is more detectable than the intensity ratio method as its system is easier

to be controlled than the intensity ratio whose accuracy is highly dependent on the system's alignment. However, for fast-moving objects like moving particles, fluids, and sprays, the intensity ratio method can be a viable alternative to the lifetime method, since the errors contributed by the fast movement can be reduced by the quotient formation of the intensity method. Furthermore, the intensity ratio method can conduct the 2D single-shot temperature measurement just using standard cameras instead of high-speed ones.¹⁹

For the LIP technique using the intensity ratio method, the integrated intensity ratio of two spectral positions serves to indicate the temperature of heated particles. This approach is applicable for phosphors that have two or more broad or large shifted emission lines when the temperature increases. For example, YAG:Dy is a widely used phosphor in thermometry. Figure 2.3 presents its emission spectrum with temperature and the intensity ratios of 458 nm and 497 nm. It is clear to see that YAG:Dy has two spectral lines at 458 nm and 497 nm, and the intensity ratio of these two lines are strongly temperature-dependent from 400 to 1600 K. The intensity ratio is calculated by dividing the average normalized emission intensity at 497 nm with the average normalized emission intensity at 458 nm.

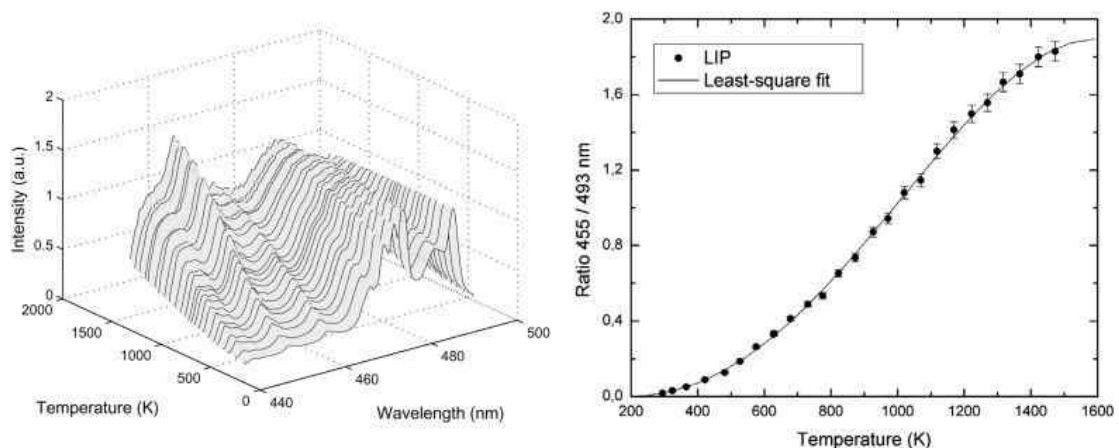


Figure 2.3: YAG:Dy emission spectrum with temperature and the intensity ratio of 458 nm and 497 nm.²¹

The LIP intensity ratio method is also suitable for two-dimensional (2D) temperature measurement. The 2D temperature images can be obtained simultaneously by two cameras

or some double imaging devices, like a stereoscope. Through two spectral bandpass filters, two individual images in the desired spectral area can be separated and retrieved at the same time. After background corrections, the temperature will be derived by overlapping two images on the pixel to pixel basis followed by evaluating the intensity ratios.²⁵ Goss and co-workers³¹ were the first to measure the temperature by the intensity ratio method based on YAG:Dy samples. A CO₂ laser was employed as the heat source, and the measurement of temperature distribution was conducted on a thermosetting plastic. The YAG:Dy phosphors presented the sensitivity over the temperature range of 300 to 1500 K, with the observed uncertainty around ± 9 to 50 K. Most recently, Jaber *et al.*³² coated the surface of porous media burner (PMB) through a mixture of YAG:Dy phosphors and binder materials. After comparing the obtained surface temperature, the intensity ratio method provided more precise results than thermocouples. The inaccuracy detected by the intensity method was only 5.3% while the inaccuracy found when using thermocouples could be up to 20%.

In this thesis, the LIP technique with the intensity ratio method was used to measure the temperature of mobile phosphor aggregates in **Chapter 3**. The phosphor aggregates were heated under high-flux radiation and experienced fast movement in a fluidized bed.

2.2.2 Infrared thermometry

Infrared thermometry is a contactless measurement technique that quantifies the thermal field on a measured surface for research purposes. The fully two-dimensional infrared (IR) camera applied in infrared thermometry can offer color images and spatially identify surface temperature fields with quick response time and high sensitivity. It has the advantages of non-intrusive measurement, suitable in high-temperature conditions, and suitable in both static conditions and fluid flows. When compared with other non-intrusive methods, infrared thermography with an IR camera is more flexible, repeatable, and easier to operate.³³

Recently, infrared thermometry has wide applications in temperature measurement. For example, Mikielewicz *et al.*³⁴ studied the dryout heat flux of four fluids in a minichannel using infrared thermometry. The IR camera determined the temperature of the channel's wall and the location of the liquid film in the flow derived from thermal images. It worked in the spectral range of 7.5 to 13 μ and could measure the temperature from 0 to 350 °C with an accuracy of $\pm 2\%$. Their work demonstrated the feasibility of using infrared thermometry to investigate the thermo-hydrodynamics of laminar flows in a minichannel. As well, infrared thermography with an IR camera can provide a high-resolution measurement of local temperatures. Mehta and Khandekar³³ employed an IR camera to study the heat transfer of water flow through a square channel. The IR camera they used had an operational spectral range of 3 to 5 μ m and the measurement uncertainty was less than 0.02 K. By capturing the high-resolution thermal images of wall temperatures, they successfully developed the heat transfer model of laminar flows and determined the heat transfer coefficient. Moreover, Klassen *et al.*³⁵ used the infrared thermometry technique to obtain the transient solid surface temperature distribution of a droplet, in an effort to investigate its evaporative cooling process. Astarita *et al.*³⁶ analyzed the capability of infrared thermography in their investigation of convective flow behaviors, such as jet over rotating disks.

The accuracy of infrared thermometry using an IR camera mainly depends on the emissivity of the object's surface, measurement distance, the angle of observation, the media gas, and interference from heating sources, such as the lamp lighting.³⁷ Emissivity is the ratio of the thermal radiation from the surface of the measured object to the radiation emitted from a black surface at the same temperature. When using an IR thermal measurement system, a uniform emissivity value, varying from 0 to 1, is required in the parameter setup. Recently, Salem *et al.*³⁸ studied the optimal emissivity values of the surface coating and used infrared thermometry to measure the thermal capability of the high-voltage power electronic components. The emissivity coefficient was adjusted through the range from 0.88 to 1.00 in

an interval of 0.02. They discovered that the optimal emissivity value was 0.98 for the black paint coating and 0.88 for the boron nitride. Their IR camera had an accuracy of ± 2 °C. However, in most cases, emissivity only contributed a small error to temperature measurement.³⁶ Furthermore, calibration procedures and a model of measurement error were developed to evaluate the accuracy of the IR camera.³⁹ Currently, most potential errors can be eliminated or considered when processing data. The new data processing software makes the system easy to operate. An image averaging function can decidedly improve the image quality under harsh environments, such as high temperature or turbulent flow.³⁶

In this thesis, infrared thermometry with an IR camera (Jenoptik, VarioCAM HD) was employed to measure the temperature of levitated biomass particles and hydrochar slurry droplets under high-flux radiation in **Chapter 5** and **Chapter 6**, respectively. The IR camera was operated at a frame rate of 50 Hz, corresponding to a temporal resolution of 20 ms, and a spatial resolution of 0.5 mm per pixel. For the setting of camera parameters, the emissivity of biomass particles was assumed to be 0.95 while that of the black slurry droplet was set to 0.98. The spectral range of the IR camera is from 7.5 to 14 μm . As the spectral wavelength of heating laser radiation is centered at 910 nm, no interference of the heating radiation to the thermometry camera can be observed. Moreover, the IR camera was employed to check the surface temperature of the static solar particles which were heated by laser radiation in **Chapter 7**. The accuracy of infrared temperature measurement has been verified with a thermocouple and the high accuracy of using the infrared camera is maintained within ± 5 K at temperatures ranging from 300 to 800 K.

2.3 Research targets used in the application of high-flux radiation

In this thesis, the high-flux radiation heating source was used to investigate and characterize radiation heating of particles, aggregates, pellets, and droplets. The selected research targets include phosphor aggregates, biomass tablets, hydrochar slurry droplets, and solid particles used in solar thermal receivers.

2.3.1 Phosphor aggregates

The primary consideration in selecting phosphors is that the temperature sensitivity of the selected phosphors must be in the desired temperature range. Their chemical and physical interaction with the environment and interference of blackbody radiation should be minimized.²¹ In this research, $\text{BaMg}_2\text{Al}_{10}\text{O}_{17}:\text{Eu}$ (BAM) and $\text{ZnO}:\text{Zn}$ were selected as the surveyed phosphors.

$\text{ZnO}:\text{Zn}$ phosphor has a short lifespan of below 1 ns, which enables the measurement of fast-moving objects, which is significant for measuring temperature in turbulent flows. It has a high-temperature sensitivity with a very large line shift. Thus, the intensity ratio between different parts of the emission spectra can be used to conduct temperature measurement. Normally, two emission lines at 380 nm and 510 nm are selected for the purpose of analysis.⁴⁰ The exceptionally high-temperature sensitivity, where 1% ratio change corresponds to around 4 K temperature change, makes the measurement very precise and therefore is the best phosphorescence measurement. Recently, Kueh *et al.*⁴¹ reported the direct planar temperature measurement of individual $\text{ZnO}:\text{Zn}$ phosphor aggregates using the LIP method, and the maximum particle temperature observed for $\text{ZnO}:\text{Zn}$ phosphors is 650 K.

BAM is another widely used phosphor, which has stable physical properties and a strong emission line at 440 nm. Its high melting point at 2190 K ensures the particles will

not be damaged in high-temperature applications.⁴² Compared to ZnO:Zn phosphors, the temperature sensitivity range of BAM phosphors can reach up to 1300 K,²¹ which is more than 500 K higher than the ZnO:Zn phosphors than that used in the previous study.⁴¹ Figure 2.4 presents the normalized emission spectra of BAM phosphors at 290 K to 1150 K following 355 nm laser excitation measured by Aldén *et al.*²¹ Based on the emission spectra at elevated temperatures, the normalized intensity at a wavelength of around 460 nm almost remains unchanged with temperature, while that at 400 nm exhibits an obvious increase. This demonstrates that the ratio of the signals obtained 460 nm to that at short slope wavelength, e.g. 400 nm can be used to provide a measurement of temperature.

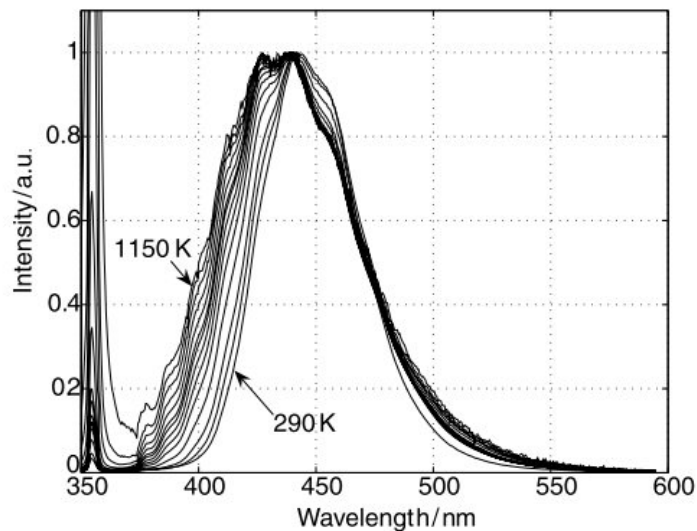


Figure 2.4: Normalized emission spectra of BAM phosphors at 290 K to 1150 K following 355 nm laser excitation.²¹

Recently, Fond *et al.*⁴³ investigated the luminescence properties of BAM phosphors in the gas phase. They performed spectrally resolved measurements on BAM phosphor powders and observed that the emission spectrum of BAM phosphors shifts continuously from 300 K to 1100 K towards shorter wavelengths. They confirmed that BAM phosphors constitute a desired material for temperature measurements in turbulent flows up to 920 K. Their work gives confidence that the LIP technique with BAM phosphors is reliable to

perform the non-intrusive temperature measurement under high-flux radiation. However, its *in-situ* phosphor temperature measurement with 2D images in high-temperature reactors has scarcely been investigated. Therefore, **Chapter 3** reports detailed work done on the two-dimensional temperature measurement of fluidized BAM phosphor aggregates through a pair of spatially resolved images in an environment where particles are heated by high-flux radiation.

Furthermore, the optical properties of dispersed media have been widely investigated. The numerical models have been developed to determine their optical properties and to study the radiation transfer of different particle suspensions. For example, Dombrovsky and co-workers⁴⁴ calculated the radiation absorption and scattering of diesel fuel droplets using the Mie theory. Their results are applicable for the analysis of radiative characterization including radiation attenuation caused by fuel droplets and spays. Recently, Coquard and Baillis⁴⁵ computed the optical properties of spherical particle beds based on independent scattering theory. Cunsolo *et al.*⁴⁶ calculated the scattering phase function of cellular foams using Monte Carlo ray-tracing techniques. Zeghondy *et al.*⁴⁷ used the Radiative Distribution Function Identification (RDFI) model to determine the extinction and absorption coefficients of high porosity materials. In addition, to confirm the robustness of modeling approaches, the experimental works for the determination of optical properties were performed on different light-absorbing-scattering media. The literature covers the extinction coefficient determination of packed-beds,⁴⁸ the asymmetry factor characterization of ceramic foams,⁴⁹⁻⁵⁰, and the scattering analysis of dispersed media.⁵¹ These previous works imply that the optical properties play an important role in the modeling of radiation trapping and heat transfer process. However, the comprehensive studies on optical properties and radiation trapping effects of phosphors, especially in the experimental aspect, have been rarely reported. Therefore, **Chapter 4** investigates the optical properties and non-thermal radiation

trapping of ZnO:Zn and BAM phosphors at room temperature using a spectro-goniometric system and a Monte Carlo ray-tracing model.

2.3.2 Biomass tablets

Biomass such as straw, rice husks, and wood, are now available in large quantities as waste from agricultural and forest practices. Biomass typically contains around 50% carbon, 6% hydrogen, and 40% oxygen on a dry, ash-free basis and its energy content is around 19 to 20 MJ kg⁻¹. A high temperature around 1200 K is required in biomass thermal processes due to their intensive energy consumption.⁵²

Currently, different types of biomass are selected as feedstock to investigate radiation-driven biomass pyrolysis and gasification. For example, Wu *et al.*⁵³ reported the pyrolysis of mallee wood powder under concentrated solar radiation at various temperatures, heating rates, and holding times. They found the products from solar-thermal pyrolysis were mainly volatiles (90 – 95 wt.%) and the char yields were maintained at considerable amounts (8.3 – 15.3 %) at a high temperature of 2200 K, which was very important to the design of solar-thermal reactors. Bellouard *et al.*⁵⁴ experimentally tested a 1 kW tubular solar reactor for continuous solar-driven gasification of biomass. A wood mixture of pine and spruce (bark included) was used as biomass feedstocks. A sun heliostat reflected the solar radiation to a parabolic mirror to a flux density up to 16 MW/m². In their work, the high carbon conversion rate was achieved at 93.5% and the maximum conversion rate of solar-to-fuel reached 28% when the temperature of the biomass was at 1700 K.

Furthermore, temperature plays an important role in the thermo-chemical processing of biomass.⁵⁵ At higher temperatures and heating rates, volatile materials easily escape from the system, resulting in the reduction of char yields. For example, according to Park *et al.*⁵⁶, when the reaction increases from 638 K to 879 K, the char yields were observed to decrease

from 31% to 17%. Conversely, at lower temperatures, biomass may experience an incomplete decomposition, which causes a large amount of non-pyrolytic solid in char product. Wang *et al.*⁵⁷ studied the effect of temperature on the product quality for various types of biomass feedstock (pine, beech, bamboo, demolition wood). They found that when the temperature ranged from 723 K to 823 K, a liquid product was formed such as bio-oil, and the solid product formed was not carbonaceous. Only at temperatures higher than 773 K did the solid product of char, which contained more than 85 wt.% carbon, form. Liquid product yields highly depend on operating conditions like reaction pressure, temperature, and volatiles residence. Increasing temperature can increase liquid yields to the maximum value.

According to Kersten *et al.*⁵⁸, the maximum yield of bio-oil was achieved at temperatures of 673-823 K for different types of biomass feedstock. Over this temperature range, the decomposition of vapor became significant, causing a decline in condensed liquid yields and a corresponding increase in gas yield. The best bio-oil quality was obtained at the maximum yield temperature. The yields of gases usually increase significantly at high temperatures because they are the main products derived from vapor decomposition. The composition of in-condensable gas is also affected by temperature. For example, Luo *et al.*⁵⁹ studied the fast pyrolysis of wood feedstocks in a fluidized bed reactor. Their experimental results showed that high temperatures greater than 773 K caused large amounts of CO and CH₄, but a small amount of CO₂. The gases with higher heating values could be obtained at a higher temperature. Therefore, direct and accurate measurement of biomass temperature is urgently required to understand the biomass thermal processes and improve energy efficiency.

Chapter 5 reports on a study that investigated the fast-thermal processes of biomass tablets under high-flux radiation heating, particularly for understanding the synergy of

renewable biomass and radiation energy. The high-fidelity data, including temporally recorded biomass temperatures and heating rates, are presented in this chapter.

2.3.3 Hydrochar slurry

Bio-slurry fuel is a kind of liquid biofuel produced from biomass resources. Compared with the traditional bioliquid, it has the advantages of low operating cost, high energy density, ease of storage, and suitability in a wide range of applications. These include boilers, gasifiers, and combustion engines.⁶⁰

Early research into liquid slurry fuels highlighted the main concerns of slurry fuel as a liquid fuel alternative. For the process of burning in slurry fuels, the liquid medium is consumed first before the solid phase begins to burn. This burning mechanism is suitable unless particle agglomeration has caused larger groups of particles to clump together which can occur before, or during the ignition stage.⁶¹ This causes low combustion efficiency and build-up of solid residue inside machinery. The particle agglomeration can be effectively overcome by using stabilization agents in the form of dispersants. In addition, ash content leads to a build-up of solids inside reactors. In the 1980s, coal-water slurry fuels were used in a diesel engine as a replacement for diesel fuels.⁶² However, the component wear of engines using slurry fuels was 2 to 20 times faster than that of engines using diesel fuels due to the higher ash content in slurry fuels.

Hydrothermal carbonization (HTC) is a thermochemical process that produces a high-energy-density char which is an important raw material of bio-slurry fuels. HTC converts the biomass feedstock into a coal-like solid product that has been successfully used as “hydrochar”.⁶³⁻⁶⁴ The typical operating temperature and pressure of HTC are maintained within the range of 453 to 523 K and 10 to 80 bar depending on the reactor’s temperature. The solid loading of the reactor must be 20 to 50% for feasible economic operations.⁶⁵ During hydrothermal treatment, significant amounts of inorganics can be dissolved in the

water and removed from the formed char product.⁶⁶ Hence, hydrochar presents a considerable reduction in ash content when compared with pyrolyzed biochar, and its utilization can significantly avoid combustion problems caused by high ash content.^{63, 67}

Currently, the studies about hydrochar are mainly focused on the direct combustion of solid products.⁶⁷⁻⁷⁰ For example, Liu *et al.*⁶⁷ investigated the co-combustion behaviors of lignite and hydrochar which were produced from coconut fibers and eucalyptus leaves. They reported that fuel quality could be improved by the hydrochar due to its high energy density and low ash content. Tremel *et al.*⁷⁰ did gasification experiments on hydrochar formed from beech wood and found that pulverized hydrochar particles could promote the fluidization process during combustion. However, work done on the application of hydrochar in the form of slurry is scarcely reported, and none of its fuel properties has been optimized for use in boiler, gasifier, or diesel engines. The thermal characteristics, such as surface temperature and heating rate, of slurry fuel droplets are also scarcely reported. Subsequently, in **Chapter 6** a new hydrochar slurry was derived from hydrothermal carbonization of grape marc. The rheological properties of hydrochar slurry were measured experimentally. A single hydrochar slurry droplet was irradiated under high-flux radiation to characterize its thermal behaviors under radiation heating.

2.3.4 Solid particles used in solar particle receivers

Solid particles have been proposed as media for the absorption of concentrated solar radiation and storage of heat in various solar reactors, such as falling particle receivers, vortex particle receivers, fluidized-bed receivers, and obstructed particle receivers with porous media.⁷¹⁻⁷⁴ Utilizing particles tolerant of high temperatures can increase the operating temperature of concentrated solar power (CSP) plants to above 1000 K, thus improving energy efficiency and reducing energy storage costs.⁷⁵ In numerical assessments of the thermal efficiency of a receiver under design, the optical properties of solar particles

including absorptivity and emissivity are of crucial importance since they are the controlling factors in solar radiation harvesting and heat loss, respectively. The absorption and emission properties of the particles' surface may change at high temperatures due to oxidation, material transformation, or both.⁷⁶

Concerning the investigation of CSP plants with solid particles, Chen *et al.*⁷⁷ modeled the thermal behavior of falling particles inside a solid particle receiver. The emissivity of solid particles was treated as a constant value of 0.8, independent of temperature. Flamant⁷⁸ measured the total emissivity (spectrally averaged) of fluidized beds of different micro-sized particles (diameter = 250 μm) under solar radiation, including zirconia, silica carbide, silica sand, and chamotte. Diago *et al.*⁷⁹ investigated the optical properties of sand and evaluated the performance of concentrated solar particle receivers. The results indicated that emissivity decreases with increasing temperature. Compared with experimental results, their numerical values show obvious underestimation, particularly when the equilibrium temperature is higher than 573 K. Klein *et al.*⁸⁰ simulated the heat transfer process within a directly irradiated solar receiver using relatively small carbon black particles. They used Mie theory to calculate the absorption efficiency factor in which the complex refraction index of carbon black particles was assumed as that of soot particles at room temperature.⁸¹

Different particles have been proposed and investigated under high operating temperatures in CSP particle receivers.⁸²⁻⁸³ Of these potential particles, ceramic particles show high absorptance, are low cost and have a long tolerance time.⁸⁴ Aluminum oxide (Al_2O_3) and silica carbide (SiC) particles are two types of ceramic particles widely used in CSP plants because of their excellent thermal properties and high refractoriness.⁸⁵ Ho *et al.*⁷¹ summarized the solar absorber efficiency of several solid particle media, including sintered bauxite proppants (contain > 75% Al_2O_3) and SiC. They found the absorptance of some of

the sintered bauxite proppants was quite high (> 0.9) and the particle stability was better at 1000 K. The absorber efficiencies of Al_2O_3 and SiC varied from 0.84 to 0.86, which were much higher than that of fracking sand (0.49). Al_2O_3 and SiC have also been widely used as media in numerical simulations of CSP plants.^{77, 86} For example, Gomez-Garcia *et al.*⁸⁶ developed an analytical model comprising a multistage fluidized bed heat exchanger for designing concentrated solar plants. Their analysis was conducted based on the thermal properties of SiC particles. According to their model, the system's thermal efficiency could reach 99.3% and a global heat exchange efficiency achieving 49.7%. However, the absorptivity and emissivity of typical solar particles (Al_2O_3 and SiC) at high temperatures have been rarely reported and remain the main sources of uncertainty in numerical simulations of concentrated solar-particle receivers. Thus, to provide reliable values of emissivity and absorption function for the numerical modeling of CSP receivers, the detailed work on the absorption and emission properties of Al_2O_3 and SiC particles at high temperatures (up to 1200 K) is reported in **Chapter 7**.

In addition, solid solar particles ranging from hundreds of micrometers to a few millimeters were usually chosen in experimental and numerical studies, e.g. 280 μm and 697 μm in falling particle receivers⁸⁷⁻⁸⁹, 1 mm in rotating kiln/centrifugal receivers⁹⁰, 250 μm in fluidized particle receivers⁷⁸, and relatively large particles 1 - 3 mm in quartz-tube solid particle receivers⁷³. Smaller particles are not preferable, and this is likely due to safety concerns with particle egress or the high manufacturing costs of fine particles. It is particularly important but very challenging to directly measure the thermal behaviors of these small particles (hundreds of micrometers) suspended in air and under high radiation flux. Thus, **Chapter 7** also reports detailed work done on the numerical evaluation of temperature increase time and equilibrium temperature (*i.e.*, the achievable maximum temperature) for micro-size solar particles.

2.4 Levitation systems

Contactless levitation systems are significant in the study involving radiation heating since they have the potential to be easily combined with any radiation heating source without physical contact. In the application of high-flux radiation, direct temperature measurement of reactants is also required to understand the details of heat transfer in high-temperature environments. To simplify experimental conditions, the selected particle or droplet samples were usually fixed on a sample holder.⁹¹⁻⁹² However, the sample holder can be heated under radiation and influence the reaction temperature.⁹³⁻⁹⁴ The undesired and complex heat conduction between the sample and the holder, together with potential catalytic effects, gives rise to much uncertainty. For example, Carlssona *et al.*⁹⁵ observed the behaviors of biomass particles under high-flux thermal radiation using a high-speed camera. They heated the biomass particle by a continuous wave 2 W Nd:YAG laser at 532 nm. The biomass particle was placed between two microscope cover glasses. Although most of the radiation is transmitted through the glasses, the glasses could still be heated up by the laser, especially after a period. Wu *et al.*⁵³ reported the pyrolysis of biomass powders in a graphite crucible under concentrated solar radiation and found heat loss from the biomass samples to the crucible walls. Stenseng *et al.*⁹⁶ also stated that the discrepancy between their experimental and modeling results could be due to the heat transfer and thermal lag between the sample and the crucible/thermocouple, which was not considered in the model. Therefore, contactless levitation systems are critically required to free the samples from physical contact to avoid the influences of unnecessary heat transfer.

2.4.1 Electrodynamic (ED) balances

In the few studies that have been published on contactless levitation systems for temperature measurement, electrodynamic (ED) balances were used to suspend particles and droplets by creating a dynamic electric field. For example, Biagini *et al.*⁹⁷ developed an experimental

method to suspend a single biomass particle and characterized its chars formed by fast pyrolysis with high temperature and heating rate. An ED balance was chosen to levitate the biomass particle due to its versatility. The biomass was heated by a CO₂ laser and its temperature was measured by pyrometry. Figure 2.5 shows the schematic of their ED balance and temperature measurement system. Also, D'Amore *et al.*⁹⁸ used ED balance to study the oxidation rates of single char particles in the temperature range of 500 to 1200 K. Weiss and Bar-Ziv⁹⁹ studied the non-uniform shrinkage and activation of highly porous chars during combustion using an improved ED chamber. Oxidation of char particles was investigated in the ED balance at temperatures in the vicinity of 900 K. However, the technique using ED balance could only levitate a single small object with a size less than 300 μm.¹⁰⁰⁻¹⁰¹ Moreover, an electrical field can potentially influence chemical reactions in which charge transfer is involved.

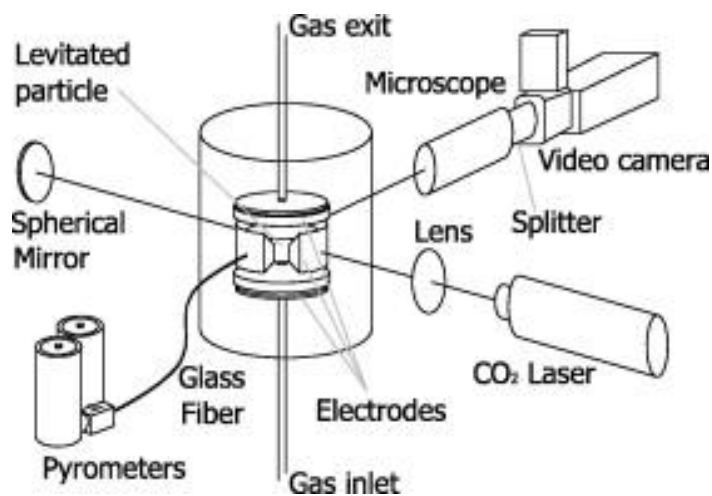


Figure 2.5: Schematic of the ED balance and the system of temperature measurement.⁹⁷

2.4.2 Acoustic levitators using acoustic force

The acoustic levitator is another apparatus that is also widely used for single-particle and droplet suspensions. Compared to an ED balance, an acoustic levitator is relatively simple to fabricate and can be combined easily with an external heating source. Currently, Contreras

*et al.*¹⁰² suspended liquid samples by acoustic levitator and detected chemical elements of liquid samples. The acoustic levitation system they presented was inexpensive and provided stable trapping force to suspend drops with diameters around 780 μm . Figure 2.6 presents the schematic of their experimental setup.

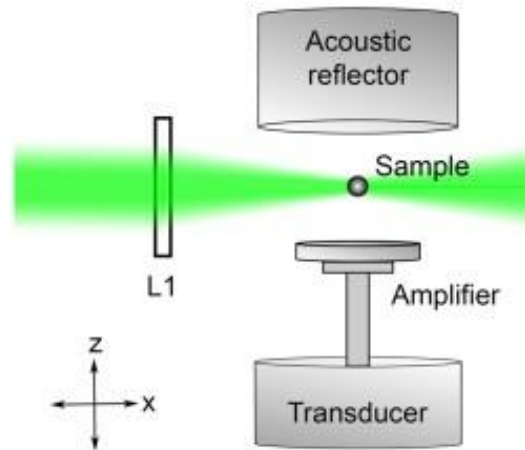


Figure 2.6: Schematic of the acoustic levitation system on the xz-plane.¹⁰²

Recently, Marzo *et al.*¹⁰³ developed a novel acoustic levitation system that could hold objects with larger sizes and densities. A total of 72 transducers were arranged at the top and bottom surfaces of the 3D printed levitator frame in a hexagonal pattern and operated at 40 kHz. They transformed the electrical input signal into acoustic waves and generated enough trapping force to levitate both particles and droplets. A higher voltage of the excitation signal was required to levitate the denser objects. When the power voltage was maintained at 12 V, this made it possible to suspend objects with a diameter up to 4 mm and a density as high as 2.2 g/cm^3 . Their levitator could provide continuous levitation for more than 2 h and highlighted good stability when the local temperature changed. Figure 2.7 presents the simulated acoustic field produced by the levitator.

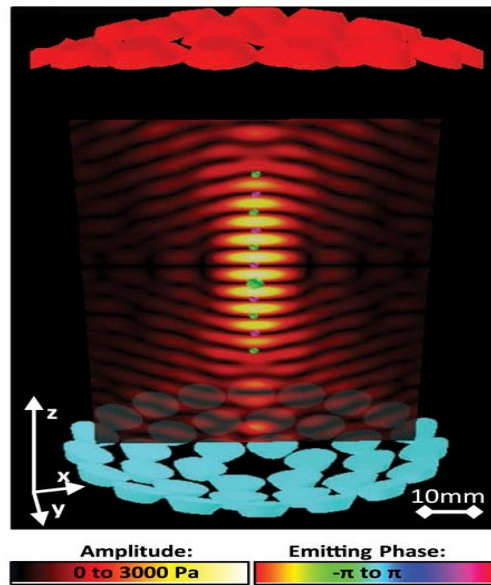


Figure 2.7: Simulated acoustic field produced by the levitator. The color represents the emitting phase of the transducers.¹⁰³

Although the acoustic levitator is a suitable apparatus that can achieve contactless suspension and is easy to combine with high-flux radiation heating sources, its applications on biomass/biofuel thermal processes, especially the measurement of temperature and heating rate of fuels, are rarely reported. For this reason, in this thesis, the acoustic levitator was used to study the thermal processes of heated biomass particles and hydrochar slurry droplets under high-flux radiation. The detailed analyses are reported in **Chapter 5** and **Chapter 6**, respectively.

2.5 Research gaps

In summary, according to the literature review, radiation heating is critical in the investigation and characterization of different heat-related engineering processes, especially for small target objects (< 5 mm). The specific research gaps related to these targets include:

- Inadequate investigation of the *in-situ* temperature imaging for fluidized phosphors in high-temperature reactors and the radiation trapping effect of phosphors.
- Unpredictable uncertainty caused by complex heat conduction between the sample and the holder in temperature measurement of biomass thermal processes
- Insufficient report about the application of hydrochar in the form of a slurry droplet and its fuel properties and thermal characteristics for use in boiler, gasifier, or diesel engines
- Deficient applications of levitation system on biomass/biofuel thermal processes, especially the measurement of temperature and heating rate of fuels
- Limited determination of absorptivity and emissivity of typical solar particles (Al_2O_3 and SiC) at high temperatures, which is the main source of uncertainty in numerical simulations of concentrated solar-particle receivers

Therefore, the well-controlled high-flux radiation is employed as the heating source in this thesis to address these concerned research problems regarding the temperature measurement, the mechanism of heat transfer, and the determination of optical properties.

References

1. Beeson, E. J. G., The CSI lamp as a source of radiation for solar simulation. *Lighting Research & Technology* **1978**, *10* (3), 164-166.
2. Levêque, G.; Bader, R.; Lipiński, W.; Haussener, S., High-flux optical systems for solar thermochemistry. *Solar Energy* **2017**, *156*, 133-148.
3. Tawfik, M.; Tonnellier, X.; Sansom, C., Light source selection for a solar simulator for thermal applications: A review. *Renewable and Sustainable Energy Reviews* **2018**, *90*, 802-813.
4. Irwan, Y. M.; Leow, W. Z.; Irwanto, M.; Amelia, A. R.; Gomesh, N.; Safwati, I., Analysis Air Cooling Mechanism for Photovoltaic Panel by Solar Simulator. *International Journal of Electrical & Computer Engineering* **2015**, *5* (4), 636-643.
5. Pernpeintner, J.; Happich, C.; Lüpfer, E.; Schiricke, B.; Lichtenthäler, N.; Weinhausen, J., Linear Focus Solar Simulator Test Bench for Non-destructive Optical Efficiency Testing of Parabolic Trough Receivers. *Energy Procedia* **2015**, *69*, 518-522.
6. Ekman, B. M.; Brooks, G.; Akbar Rhamdhani, M., Development of high flux solar simulators for solar thermal research. *Solar Energy Materials and Solar Cells* **2015**, *141*, 436-446.
7. Guo, P.; Wang, Y.; Meng, Q.; Li, J., Experimental study on an indoor scale solar chimney setup in an artificial environment simulation laboratory. *Applied Thermal Engineering* **2016**, *107*, 818-826.
8. Codd, D. S.; Carlson, A.; Rees, J.; Slocum, A. H., A low cost high flux solar simulator. *Solar Energy* **2010**, *84* (12), 2202-2212.
9. Kim, S. i.; Kissick, J.; Spence, S.; Boyle, C., Design, analysis and performance of a polymer-carbon nanotubes based economic solar collector. *Solar Energy* **2016**, *134*, 251-263.

10. Li, J.; Gonzalez-Aguilar, J.; Romero, M., Line-concentrating Flux Analysis of 42kWe High-flux Solar Simulator. *Energy Procedia* **2015**, *69*, 132-137.
11. Dong, X.; Sun, Z.; Nathan, G. J.; Ashman, P. J.; Gu, D., Time-resolved spectra of solar simulators employing metal halide and xenon arc lamps. *Solar Energy* **2015**, *115*, 613-620.
12. Kuhn, P.; Hunt, A., A new solar simulator to study high temperature solid-state reactions with highly concentrated radiation. *Solar Energy Materials* **1991**, *24* (1), 742-750.
13. Li, X.; Chen, J.; Lipiński, W.; Dai, Y.; Wang, C.-H., A 28 kWe multi-source high-flux solar simulator: Design, characterization, and modeling. *Solar Energy* **2020**, *211*, 569-583.
14. Alwahabi, Z. T.; Kueh, K. C.; Nathan, G. J.; Cannon, S., Novel solid-state solar thermal simulator supplying 30,000 suns by a fibre optical probe. *Optics Express* **2016**, *24* (22), 1444-1453.
15. Werner, M.; Wessling, C.; Hengesbach, S.; Traub, M.; Hoffmann, H.-D. In *100 W/100 um passively cooled fiber coupled diode laser at 976 nm based on multiple 100 um single emitters*, High-Power Diode Laser Technology and Applications VII, International Society for Optics and Photonics: 2009; p 71980P.
16. Vijayakumar, D.; Jensen, O. B.; Ostendorf, R.; Westphalen, T.; Thestrup, B., Spectral beam combining of a 980 nm tapered diode laser bar. *Optics Express* **2010**, *18* (2), 893-898.
17. Jaramillo, O. A.; Río, J. A. d.; Huelsz, G., A thermal study of optical fibres transmitting concentrated solar energy. *Journal of Physics D: Applied Physics* **1999**, *32* (9), 1000-1005.
18. Liang, D.; Nunes, Y.; Monteiro, L. F.; Monteiro, M. F.; Collares-Pereira, M. In *200-W solar energy delivery with optical fiber bundles*, Nonimaging Optics: Maximum

Efficiency Light Transfer IV, International Society for Optics and Photonics: 1997; pp 217-224.

19. Allison, S. W.; Gillies, G. T., Remote thermometry with thermographic phosphors: Instrumentation and applications. *Review of Scientific Instruments* **1997**, *68* (7), 2615-2650.

20. Kumar, M.; Shakher, C., Measurement of temperature and temperature distribution in gaseous flames by digital speckle pattern shearing interferometry using holographic optical element. *Optics and Lasers in Engineering* **2015**, *73*, 33-39.

21. Aldén, M.; Omrane, A.; Richter, M.; Särner, G., Thermographic phosphors for thermometry: A survey of combustion applications. *Progress in Energy and Combustion Science* **2011**, *37* (4), 422-461.

22. Xiao, J. S.; Wei, J. B.; Shaw, B. D.; Peng, Z., Temperature and fiber optic spectroscopy composition measurements of heated propanol–acetone droplets. *Optics and Lasers in Engineering* **2009**, *47* (11), 1266-1272.

23. Charogiannis, A.; Beyrau, F., Laser induced phosphorescence imaging for the investigation of evaporating liquid flows. *Experiments in Fluids* **2013**, *54* (5), 1518-1533.

24. Cates, M.; Allison, S.; Jaiswal, S.; Beshears, D., *YAG: Dy and YAG: Tm Fluorescence Above 1400 °C*. United States. Department of Energy: 2003.

25. Knappe, C.; Lindén, J.; Richter, M.; Aldén, M., Enhanced color ratio calibration for two-dimensional surface thermometry using laser-induced phosphorescence. *Measurement Science and Technology* **2013**, *24* (8), 85202-85212.

26. Brübach, J.; Pflitsch, C.; Dreizler, A.; Atakan, B., On surface temperature measurements with thermographic phosphors: A review. *Progress in Energy and Combustion Science* **2013**, *39* (1), 37-60.

27. Fletcher, T. H., Time-resolved particle temperature and mass loss measurements of a bituminous coal during devolatilization. *Combustion and Flame* **1989**, *78* (2), 223-236.

28. Khatami, R.; Stivers, C.; Joshi, K.; Levendis, Y. A.; Sarofim, A. F., Combustion behavior of single particles from three different coal ranks and from sugar cane bagasse in O₂/N₂ and O₂/CO₂ atmospheres. *Combustion and Flame* **2012**, *159* (3), 1253-1271.
29. Brübach, J.; Zetterberg, J.; Omrane, A.; Li, Z. S.; Aldén, M.; Dreizler, A., Determination of surface normal temperature gradients using thermographic phosphors and filtered Rayleigh scattering. *Applied Physics B* **2006**, *84* (3), 537-541.
30. Jaber, A.; Zigan, L.; Sakhrieh, A.; Leipertz, A., Laser-induced Phosphorescence in Combustion Diagnostics Calibration at Extremely High Temperatures. In *11th Int. Conference on Combustion and Energy Utilization (ICCEU)*, Portugal 2012.
31. Goss, L. P.; Smith, A. A.; Post, M. E., Surface thermometry by laser-induced fluorescence. *Review of Scientific Instruments* **1989**, *60* (12), 3702-3706.
32. Jaber, A.; Zigan, L.; Sakhrieh, A.; Leipertz, A., Surface temperature measurements in a porous media burner using a new laser-induced phosphorescence intensity ratio technique. *Measurement Science and Technology* **2013**, *24* (7), 75202-75209.
33. Mehta, B.; Khandekar, S., Infra-red thermography of laminar heat transfer during early thermal development inside a square mini-channel. *Experimental Thermal and Fluid Science* **2012**, *42*, 219-229.
34. Mikielwicz, D.; Wajs, J.; Gliński, M.; Zrooga, A.-B. R. S., Experimental investigation of dryout of SES 36, R134a, R123 and ethanol in vertical small diameter tubes. *Experimental Thermal and Fluid Science* **2013**, *44*, 556-564.
35. Klassen, M.; di Marzo, M.; Sirkis, J., Infrared thermography of dropwise evaporated cooling. *Experimental Thermal and Fluid Science* **1992**, *5* (1), 136-141.
36. Astarita, T.; Cardone, G.; Carlomagno, G. M.; Meola, C., A survey on infrared thermography for convective heat transfer measurements. *Optics & Laser Technology* **2000**, *32* (7), 593-610.

37. Dančová, P.; Michalski, D.; Strąk, K.; Piasecka, M., Comparison of two surface temperature measurement using thermocouples and infrared camera. *EPJ Web of Conferences* **2017**, *143*, 02075.
38. Salem, T. E.; Ibitayo, D.; Geil, B. R., Validation of Infrared Camera Thermal Measurements on High-Voltage Power Electronic Components. *IEEE Transactions on Instrumentation and Measurement* **2007**, *56* (5), 1973-1978.
39. Stallings, D. W.; Whetsel, R. G. In *Use Of Infrared Imagery In Continuous Flow Wind Tunnels*, Proc.SPIE, 1983.
40. Abram, C.; Fond, B.; Beyrau, F., High-precision flow temperature imaging using ZnO thermographic phosphor tracer particles. *Optics Express* **2015**, *23* (15), 19453-68.
41. Kueh, K. C. Y.; Lau, T. C. W.; Nathan, G. J.; Alwahabi, Z. T., Single-shot planar temperature imaging of radiatively heated fluidized particles. *Optics Express* **2017**, *25* (23), 28764-28775.
42. Sarner, G.; Richter, M.; Alden, M., Investigations of blue emitting phosphors for thermometry. *Measurement Science and Technology*. **2008**, *19* (12), 125304-125313.
43. Fond, B.; Abram, C.; Beyrau, F., Characterisation of the luminescence properties of BAM:Eu²⁺ particles as a tracer for thermographic particle image velocimetry. *Applied Physics B* **2015**, *121* (4), 495-509.
44. Dombrovsky, L. A.; Sazhin, S. S.; Mikhalovsky, S. V.; Wood, R.; Heikal, M. R., Spectral properties of diesel fuel droplets. *Fuel* **2003**, *82* (1), 15-22.
45. Coquard, R.; Baillis, D., Radiative characteristics of opaque spherical particles beds: a new method of prediction. *Journal of Thermophysics and Heat Transfer* **2004**, *18* (2), 178-186.
46. Cunsolo, S.; Coquard, R.; Baillis, D.; Chiu, W. K. S.; Bianco, N., Radiative properties of irregular open cell solid foams. *International Journal of Thermal Sciences* **2017**, *117*, 77-89.

47. Zeghondy, B.; Iacona, E.; Taine, J., Determination of the anisotropic radiative properties of a porous material by radiative distribution function identification (RDFI). *International Journal of Heat and Mass Transfer* **2006**, *49* (17-18), 2810-2819.
48. Lopes, R.; Moura, L. M.; Baillis, D.; Sacadura, J. F., Directional Spectral Emittance of a Packed Bed: Correlation Between Theoretical Prediction and Experimental Data. *Journal of Heat Transfer* **2000**, *123* (2), 240-248.
49. Barreto, G.; Canhoto, P.; Collares-Pereira, M., Combined experimental and numerical determination of the asymmetry factor of scattering phase functions in porous volumetric solar receivers. *Solar Energy Materials and Solar Cells* **2020**, *206*, 110327.
50. Zhao, S.; Sun, X.; Que, Q.; Zhang, W., Influence of Scattering Phase Function on Estimated Thermal Properties of Al₂O₃ Ceramic Foams. *International Journal of Thermophysics* **2019**, *40* (1), 11.
51. Sacadura, J.; Baillis, D., Experimental characterization of thermal radiation properties of dispersed media. *International Journal of Thermal Sciences* **2002**, *41* (7), 699-707.
52. Nzihou, A.; Flamant, G.; Stanmore, B., Synthetic fuels from biomass using concentrated solar energy – A review. *Energy* **2012**, *42* (1), 121-131.
53. Wu, H.; Gauthier, D.; Yu, Y.; Gao, X.; Flamant, G., Solar-Thermal Pyrolysis of Mallee Wood at High Temperatures. *Energy & Fuels* **2017**, *32* (4), 4350-4356.
54. Bellouard, Q.; Abanades, S.; Rodat, S.; Dupassieux, N., Solar thermochemical gasification of wood biomass for syngas production in a high-temperature continuously-fed tubular reactor. *International Journal of Hydrogen Energy* **2017**, *42* (19), 13486-13497.
55. Sharma, A.; Pareek, V.; Zhang, D., Biomass pyrolysis—A review of modelling, process parameters and catalytic studies. *Renewable and Sustainable Energy Reviews* **2015**, *50*, 1081-1096.

56. Park, W. C.; Atreya, A.; Baum, H. R., Experimental and theoretical investigation of heat and mass transfer processes during wood pyrolysis. *Combustion and Flame* **2010**, *157* (3), 481-494.
57. Wang, X.; Kersten, S. R. A.; Prins, W.; van Swaaij, W. P. M., Biomass Pyrolysis in a Fluidized Bed Reactor. Part 2: Experimental Validation of Model Results. *Industrial & Engineering Chemistry Research* **2005**, *44* (23), 8786-8795.
58. Kersten, S. R. A.; Wang, X.; Prins, W.; van Swaaij, W. P. M., Biomass Pyrolysis in a Fluidized Bed Reactor. Part 1: Literature Review and Model Simulations. *Industrial & Engineering Chemistry Research* **2005**, *44* (23), 8773-8785.
59. Luo, Z.; Wang, S.; Liao, Y.; Zhou, J.; Gu, Y.; Cen, K., Research on biomass fast pyrolysis for liquid fuel. *Biomass and Bioenergy* **2004**, *26* (5), 455-462.
60. Benter, M. M.; Gilmour, I. A.; Arnoux, L., Biomass-oil slurry fuels: an investigation into their preparation and formulation. *Biomass and Bioenergy* **1997**, *12* (4), 253-261.
61. Roy Choudhury, P., Slurry fuels. *Progress in Energy and Combustion Science* **1992**, *18* (5), 409-427.
62. Caton, J. A.; Hsu, B. D., The General Electric Coal-Fueled Diesel Engine Program (1982–1993): A Technical Review. *Journal of Engineering for Gas Turbines and Power* **1994**, *116* (4), 749-757.
63. Libra, J. A.; Ro, K. S.; Kammann, C.; Funke, A.; Berge, N. D.; Neubauer, Y.; Titirici, M.-M.; Fühner, C.; Bens, O.; Kern, J.; Emmerich, K.-H., Hydrothermal carbonization of biomass residuals: a comparative review of the chemistry, processes and applications of wet and dry pyrolysis. *Biofuels* **2011**, *2* (1), 71-106.
64. Kambo, H. S.; Dutta, A., A comparative review of biochar and hydrochar in terms of production, physico-chemical properties and applications. *Renewable and Sustainable Energy Reviews* **2015**, *45*, 359-378.

65. Titirici, M.-M.; Funke, A.; Kruse, A., Hydrothermal Carbonization of Biomass. In *Recent Advances in Thermo-Chemical Conversion of Biomass*, Pandey, A.; Bhaskar, T.; Stöcker, M.; Sukumaran, R. K., Eds. Elsevier: Boston, 2015; pp 325-352.
66. Funke, A.; Ziegler, F., Hydrothermal carbonization of biomass: A summary and discussion of chemical mechanisms for process engineering. *Biofuels, Bioproducts and Biorefining* **2010**, *4* (2), 160-177.
67. Liu, Z.; Quek, A.; Kent Hoekman, S.; Srinivasan, M. P.; Balasubramanian, R., Thermogravimetric investigation of hydrochar-lignite co-combustion. *Bioresource Technology* **2012**, *123*, 646-652.
68. Islam, M. A.; Kabir, G.; Asif, M.; Hameed, B. H., Combustion kinetics of hydrochar produced from hydrothermal carbonisation of Karanj(*Pongamia pinnata*) fruit hulls via thermogravimetric analysis. *Bioresource Technology* **2015**, *194*, 14-20.
69. He, C.; Giannis, A.; Wang, J.-Y., Conversion of sewage sludge to clean solid fuel using hydrothermal carbonization: Hydrochar fuel characteristics and combustion behavior. *Applied Energy* **2013**, *111*, 257-266.
70. Tremel, A.; Stemann, J.; Herrmann, M.; Erlach, B.; Spliethoff, H., Entrained flow gasification of biocoal from hydrothermal carbonization. *Fuel* **2012**, *102*, 396-403.
71. Ho, C.; Christian, J.; Gill, D.; Moya, A.; Jeter, S.; Abdel-Khalik, S.; Sadowski, D.; Siegel, N.; Al-Ansary, H.; Amsbeck, L.; Gobereit, B.; Buck, R., Technology Advancements for Next Generation Falling Particle Receivers. *Energy Procedia* **2014**, *49*, 398-407.
72. Chinnici, A.; Arjomandi, M.; Tian, Z. F.; Lu, Z.; Nathan, G. J., A Novel Solar Expanding-Vortex Particle Reactor: Influence of Vortex Structure on Particle Residence Times and Trajectories. *Solar Energy* **2015**, *122*, 58-75.
73. Zhang, Y.; Bai, F.; Zhang, X.; Wang, F.; Wang, Z., Experimental Study of a Single Quartz Tube Solid Particle Air Receiver. *Energy Procedia* **2015**, *69*, 600-607.

74. Lee, T.; Lim, S.; Shin, S.; Sadowski, D. L.; Abdel-Khalik, S. I.; Jeter, S. M.; Al-Ansary, H., Numerical simulation of particulate flow in interconnected porous media for central particle-heating receiver applications. *Solar Energy* **2015**, *113*, 14-24.
75. Behar, O.; Khellaf, A.; Mohammedi, K., A review of studies on central receiver solar thermal power plants. *Renewable and Sustainable Energy Reviews* **2013**, *23*, 12-39.
76. Wang, F.; Cheng, L.; Xie, Y.; Jian, J.; Zhang, L., Effects of SiC shape and oxidation on the infrared emissivity properties of ZrB₂-SiC ceramics. *Journal of Alloys and Compounds* **2015**, *625*, 1-7.
77. Chen, H.; Chen, Y.; Hsieh, H.-T.; Siegel, N., Computational Fluid Dynamics Modeling of Gas-Particle Flow Within a Solid-Particle Solar Receiver. *Journal of Solar Energy Engineering* **2006**, *129* (2), 160-170.
78. Flamant, G., Theoretical and experimental study of radiant heat transfer in a solar fluidized-bed receiver. *AIChE Journal* **1982**, *28* (4), 529-535.
79. Diago, M.; Iniesta, A. C.; Soum-Glaude, A.; Calvet, N., Characterization of desert sand to be used as a high-temperature thermal energy storage medium in particle solar receiver technology. *Applied Energy* **2018**, *216*, 402-413.
80. Klein, H. H.; Karni, J.; Ben-Zvi, R.; Bertocchi, R., Heat transfer in a directly irradiated solar receiver/reactor for solid-gas reactions. *Solar Energy* **2007**, *81* (10), 1227-1239.
81. Dalzell, W. H.; Sarofim, A. F., Optical Constants of Soot and Their Application to Heat-Flux Calculations. *Journal of Heat Transfer* **1969**, *91* (1), 100-104.
82. Hellmann, J. R.; McConnell, V. S. *Characterization of spherical ceramic particles for solar thermal transfer media: A market survey*; Sandia National Labs., Albuquerque, NM: United States, 1986-10-01, 1986.

83. Siegel, N.; Gross, M.; Ho, C.; Phan, T.; Yuan, J., Physical properties of solid particle thermal energy storage media for concentrating solar power applications. *Energy Procedia* **2014**, *49* (1), 1015-1023.
84. Ho, C. K., A review of high-temperature particle receivers for concentrating solar power. *Applied Thermal Engineering* **2016**, *109*, 958-969.
85. Tan, T.; Chen, Y., Review of study on solid particle solar receivers. *Renewable and Sustainable Energy Reviews* **2010**, *14* (1), 265-276.
86. Gomez-Garcia, F.; Gauthier, D.; Flamant, G., Design and performance of a multistage fluidised bed heat exchanger for particle-receiver solar power plants with storage. *Applied Energy* **2017**, *190*, 510-523.
87. Kim, K.; Siegel, N.; Kolb, G.; Rangaswamy, V.; Moujaes, S. F., A study of solid particle flow characterization in solar particle receiver. *Solar Energy* **2009**, *83* (10), 1784-1793.
88. Siegel, N. P.; Ho, C. K.; Khalsa, S. S.; Kolb, G. J., Development and Evaluation of a Prototype Solid Particle Receiver: On-Sun Testing and Model Validation. *Journal of Solar Energy Engineering* **2010**, *132* (2).
89. Ho, C. K.; Christian, J. M.; Romano, D.; Yellowhair, J.; Siegel, N.; Savoldi, L.; Zanino, R., Characterization of Particle Flow in a Free-Falling Solar Particle Receiver. *Journal of Solar Energy Engineering* **2017**, *139* (2), 021011.
90. Wu, W.; Amsbeck, L.; Buck, R.; Waibel, N.; Langner, P.; Pitz-Paal, R., On the influence of rotation on thermal convection in a rotating cavity for solar receiver applications. *Applied Thermal Engineering* **2014**, *70* (1), 694-704.
91. Al-Rahbi, A. S.; Onwudili, J. A.; Williams, P. T., Thermal decomposition and gasification of biomass pyrolysis gases using a hot bed of waste derived pyrolysis char. *Bioresource Technology* **2016**, *204*, 71-79.

92. Park, W. C.; Atreya, A.; Baum, H. R., Experimental and theoretical investigation of heat and mass transfer processes during wood pyrolysis. *Combustion and Flame* **2010**, *157* (3), 481-494.
93. Bashir, M.; Yu, X.; Hassan, M.; Makkawi, Y., Modeling and Performance Analysis of Biomass Fast Pyrolysis in a Solar-Thermal Reactor. *ACS Sustainable Chemistry & Engineering* **2017**, *5* (5), 3795-3807.
94. Zeng, K.; Soria, J.; Gauthier, D.; Mazza, G.; Flamant, G., Modeling of beech wood pellet pyrolysis under concentrated solar radiation. *Renewable Energy* **2016**, *99*, 721-729.
95. Carlsson, P.; Lycksam, H.; Gren, P.; Gebart, R.; Wiinikka, H.; Iisa, K., High-speed imaging of biomass particles heated with a laser. *Journal of Analytical and Applied Pyrolysis* **2013**, *103*, 278-286.
96. Stenseng, M.; Jensen, A.; Dam-Johansen, K., Investigation of biomass pyrolysis by thermogravimetric analysis and differential scanning calorimetry. *Journal of Analytical and Applied Pyrolysis* **2001**, *58-59*, 765-780.
97. Biagini, E.; Pintus, S.; Tognotti, L., Characterization of high heating-rate chars from alternative fuels using an electrodynamic balance. *Proceedings of the Combustion Institute*. **2005**, *30* (2), 2205-2212.
98. D'Amore, M.; Tognotti, L.; Sarofim, A. F., Oxidation rates of a single char particle in an electrodynamic balance. *Combustion and Flame* **1993**, *95* (4), 374-382.
99. Weiss, Y.; Bar-Ziv, E., Observation of nonuniform shrinkage and activation of highly porous chars during combustion in an improved electrodynamic chamber. *Combustion and Flame* **1995**, *101* (4), 452-460.
100. Chan, M. N.; Choi, M. Y.; Ng, N. L.; Chan, C. K., Hygroscopicity of Water-Soluble Organic Compounds in Atmospheric Aerosols: Amino Acids and Biomass Burning Derived Organic Species. *Environmental Science & Technology* **2005**, *39* (6), 1555-1562.

101. Tognotti, L.; Longwell, J. P.; Sarofim, A. F., The products of the high temperature oxidation of a single char particle in an electrodynamic balance. *Symposium (International) on Combustion* **1991**, 23 (1), 1207-1213.
102. Contreras, V.; Valencia, R.; Peralta, J.; Sobral, H.; Meneses-Nava, M. A.; Martinez, H., Chemical elemental analysis of single acoustic-levitated water droplets by laser-induced breakdown spectroscopy. *Optics Letters* **2018**, 43 (10), 2260-2263.
103. Marzo, A.; Barnes, A.; Drinkwater, B. W., TinyLev: A multi-emitter single-axis acoustic levitator. *Review of Scientific Instruments* **2017**, 88 (8), 085105.

Chapter 3

Temperature Imaging of Mobile BaMgAl₁₀O₁₇:Eu Phosphor Aggregates under High Radiation Flux

Statement of Authorship

Title of Paper	Temperature imaging of mobile BaMgAl ₁₀ O ₁₇ :Eu phosphor aggregates under high radiation flux
Publication Status	<input checked="" type="checkbox"/> Published <input type="checkbox"/> Accepted for Publication <input type="checkbox"/> Submitted for Publication <input type="checkbox"/> Unpublished and Unsubmitted work written in manuscript style
Publication Details	Wanxia Zhao, Kimberley C.Y. Kueh, Graham J. Nathan, Zeyad T. Alwahabi. (2021) Optics and Lasers in Engineering, 137, 106398. DOI: 10.1016/j.optlaseng.2020.106398

Principal Author

Name of Principal Author (Candidate)	Wanxia Zhao		
Contribution to the Paper	Performed experiments, analysed results, interpreted data and wrote manuscript.		
Overall percentage (%)	70		
Certification:	This paper reports on original research I conducted during the period of my Higher Degree by Research candidature and is not subject to any obligations or contractual agreements with a third party that would constrain its inclusion in this thesis. I am the primary author of this paper.		
Signature		Date	03/07/20

Co-Author Contributions

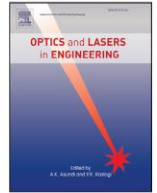
By signing the Statement of Authorship, each author certifies that:

- the candidate's stated contribution to the publication is accurate (as detailed above);
- permission is granted for the candidate to include the publication in the thesis; and
- the sum of all co-author contributions is equal to 100% less the candidate's stated contribution.

Name of Co-Author	Kimberley C.Y. Kueh		
Contribution to the Paper	Assisted in experiments, discussed experimental results and findings, and revised the manuscript.		
Signature		Date	22/07/2020

Name of Co-Author	Graham J. Nathan		
Contribution to the Paper	Revised the manuscript.		
Signature	member: 6F60A2C9-464C-4731-A902-50897C953BAA A6618188-A72C-4467-995B-F4E03C526843 <small>Digitally signed by member: 6F60A2C9-464C-4731-A902-50897C953BAA A6618188-A72C-4467-995B-F4E03C526843 DN: cn=member, o=UNSW, ou=UNSW, email=6F60A2C9-464C-4731-A902-50897C953BAA A6618188-A72C-4467-995B-F4E03C526843, c=AU Date: 2020.07.23 16:37:39 +09'30'</small>	Date	23/07/2020

Name of Co-Author	Zeyad T. Alwahabi		
Contribution to the Paper	Discussed experimental results and findings, supervised the research project, and revised the manuscript.		
Signature	member: 6F60A2C9-464C-4731-A902-50897C953BAA A6618188-A72C-4467-995B-F4E03C526843 <small>Digitally signed by member: 6F60A2C9-464C-4731-A902-50897C953BAA A6618188-A72C-4467-995B-F4E03C526843 DN: cn=member, o=6F60A2C9-464C-4731-A902-50897C953BAA A6618188-A72C-4467-995B-F4E03C526843, email=member.6F60A2C9-464C-4731-A902-50897C953BAA A6618188-A72C-4467-995B-F4E03C526843 Date: 2020.07.22 22:08:11 +0930</small>	Date	22/07/2020



Temperature imaging of mobile BaMgAl₁₀O₁₇:Eu phosphor aggregates under high radiation flux

Wanxia Zhao^{a,c}, Kimberley C.Y. Kueh^{b,c}, Graham J. Nathan^{b,c}, Zeyad T. Alwahabi^{a,c,*}

^a School of Chemical Engineering and Advanced Materials, The University of Adelaide, SA 5005, Australia

^b School of Mechanical Engineering, The University of Adelaide, SA 5005, Australia

^c Centre of Energy Technology, The University of Adelaide, SA 5005, Australia

ARTICLE INFO

Keywords:

Planar temperature imaging of suspended aggregates
Laser-induced phosphorescence (LIP)
Thermographic phosphors
Homogeneous radiation heating

ABSTRACT

Planar laser-induced phosphorescence (PLIP) has been used for the temperature measurement of suspended phosphor aggregates. Two-dimensional surface temperature of fluidized phosphor aggregates was measured through a pair of spatial and wavelength resolved images in an environment where phosphors are heated by high-flux radiation. The heating was supplied by a multi-diode laser system which provides a well-characterized high-flux radiation up to 28.87 MW/m². Phosphors made of BaMgAl₁₀O₁₇:Eu (BAM) were selected as the material and suspended in a fluidized bed. Single-shot temperature imaging of BAM aggregates were inferred and compared at several heat fluxes. With the increasing heat flux up to 28.87 MW/m², the BAM aggregates were found to exhibit a wider range of temperature distribution, and the maximum average aggregate temperature achieved 723 K, while the maximum temperature of a single aggregate could reach up to 1063 K. The wider temperature distributions that observed under higher radiation fluxes were caused by the elevated temperature of cooling air and the non-uniform aggregate surfaces. This non-intrusive method of measuring temperature offers advantages over other available methods in the study of heat transfer processes involving high-temperature reactions.

1. Introduction

Radiation heat transfer is a fundamental and significant phenomenon in many heat-related engineering processes. High-flux radiation is widely used as the dominant mode of heat transfer in a variety of processes, especially which are associated with time-dependent heat transfer inside particle suspensions, such as biomass gasification [1,2], combustion [3], fuels production [4] and materials processing [5–7]. Compared with convective heat transfer, radiation heating is efficient as it scales with the fourth power of temperature difference and enables contactless energy transfer. Many sources of pure, or nearly pure, radiation is available, such as spanning concentrated solar thermal energy, plasmas, lasers, microwaves, and radiant burners. These have the advantages of achieving high heating rates and eliminating contamination.

A key to advancing the understand of radiation heat transfer in suspension-flow particle receivers and reactors is the capacity to provide a well-resolved measurement of particle temperature, both spatially and temporally. In addition to its dominant influence on heat transfer through the fourth power dependence on heat transfer, it also has a significant impact on the optical properties, species compositions, and phases of the particle-gas flow. However, few investigations are available of temperature measurements of particles in suspension at high

temperatures, which leads to significant uncertainty in the details of the heat transfer in such environments. This lack of available data is because non-intrusive temperature measurements of suspended particles in a multiphase flow are difficult. Currently, the performance of suspension-flow particle reactor using radiation heating has been widely studied for high-temperature particle reactors, such as solar thermal receiver [8–10], gasifier [11,12], and fluidized bed [13,14], however, the *in situ* particle temperature in such reactors is scarcely investigated and only gas temperatures have been reported [15–17].

Various non-intrusive laser diagnostic techniques are emerging with strong potential to achieve *in situ* particle measurements with high resolution [18–20]. One of these techniques is laser-induced phosphorescence (LIP). The LIP method relies on the temperature-dependent properties of thermographic phosphors (TPs) [21]. Following laser excitation, the emitted phosphorescence can be collected using an ICCD camera. The spectral property of the emitted radiation is temperature-dependent and can serve as the parameter to determine surface temperatures of phosphors [19]. Based on the required temperature ranges, different thermographic phosphors are suitable for different applications.

Compared with other non-invasive temperature measurement techniques identified to date, LIP is able to provide more accurate results due to its low sensitivity of the phosphor surface properties to temper-

* Corresponding author.

E-mail address: zeyad.alwahabi@adelaide.edu.au (Z.T. Alwahabi).

<https://doi.org/10.1016/j.optlaseng.2020.106398>

Received 22 May 2020; Received in revised form 31 August 2020; Accepted 10 September 2020

Available online 25 September 2020

0143-8166/Crown Copyright © 2020 Published by Elsevier Ltd. All rights reserved.

ature and low interferences from chemiluminescence or scattering light [19,22]. For example, pyrometry is another method that can provide non-invasively two-dimensional temperature measurement. However, its accuracy is affected by the emissivity of target surfaces and interfering light from surrounding objects or backgrounds. Pyrometry is unable to differentiate the temperature signal was from the particle surface only or was interfered with the surrounding noises [23,24].

Previous studies that using the LIP technique to perform temperature measurement only work on the gas temperature of multi-phase flows. They usually assumed the phosphor particles are small enough for heat transfer processes and can be modeled as a gas [25–27]. However, the direct temperature measurement of solid phosphor particles is scarcely reported.

Among the limited works in studying the temperature of solid phosphors, recently, Kueh et al. reported a direct planar temperature measurement of individual ZnO:Zn phosphor aggregates using the LIP method. However, the maximum temperature that can be observed for ZnO:Zn phosphors is 650 K because the phosphors are damaged above this range [19,28]. It limits ZnO:Zn phosphors in applications like combustion or solar thermal reactors, whose reaction temperature requirement is higher than this temperature. Therefore, BaMgAl₁₀O₁₇:Eu (BAM) phosphors have been selected to be heated directly. The BAM phosphor has a large temperature sensitivity range up to 1300 K [19], which is more than 500 K higher than the ZnO:Zn phosphor that used in the previous study [28].

Furthermore, choosing a suitable heating source is equally important in studying the radiation heat transfer within phosphor suspensions. Since the short residence time of phosphors in the heating region when fluidization occurs is evident, the heat flux needs to be high enough, scaling-up to the power level of MW, to heat the small phosphors to a high temperature within a short time [2].

The main objective of this work is to non-intrusively measure the temperature of mobile BAM phosphors in multiphase flow using the LIP technique with high resolution. The BAM phosphors were heated using a well-characterized multi-diode laser system to reach a high temperature within a short time. Representative results were shown and discussed in

this analysis by highlighting the spatially and temporally resolved temperature images under different high fluxes. The average and maximum temperature of mobile BAM phosphors, together with the corresponding temperature distribution, were studied with the purpose of determining the dependence of phosphor temperature to a function of heat flux.

2. Experimental methodology

The experimental setup was organized into three phases, which are a high radiation multi-diode laser system to generate the high flux radiation, a fluidized bed with optical accesses, and a laser diagnostics system with an excitation source and imaging device. Fig. 1 presents a schematic diagram of how these components are arranged together.

The peak wavelength of the high radiation multi-diode laser system varied slightly from 904.0 nm to 918.5 nm within the operating temperature range [29]. The device delivers high output power with an excellent beam profile. The constant beam profile is important because it provides a uniform heating region inside the fluidized bed. The focused radiation had a 10.5 mm diameter and a flux, Φ , of up to 32.8 MW/m². A water chiller (PolyScience, 6500 Series) was used to cool the lasers by maintaining the operating water temperature at 291 K, which was monitored continuously with a thermocouple to make sure that the temperature did not exceed 323 K.

The fluidized bed had four optically accessible ports. The laser energy before and after the fluidized bed was monitored with two power meters (Gentec model, HP100A-4KW-HE) at a sampling frequency of 10 Hz. Dry air was used as the fluidizing gas to minimize the humidity in the fluidized bed and avoid the aggregation of phosphors. The airflow rate was maintained by a flow controller at 17.37 L/min (Alicat Scientific, MC 20 slpm) to ensure a uniform gas flow throughout the experiment. This airflow rate was set only for the fluidization of BAM aggregates with diameters around 100 μ m, while the oversized aggregates were too heavy to be fluidized and the fine single phosphors could escape with the airflow. The top of the fluidized bed was connected to an exhaust system to remove phosphors that escaped from the system. The BAM phosphors were mixed with SiO₂ particles at the volume ra-

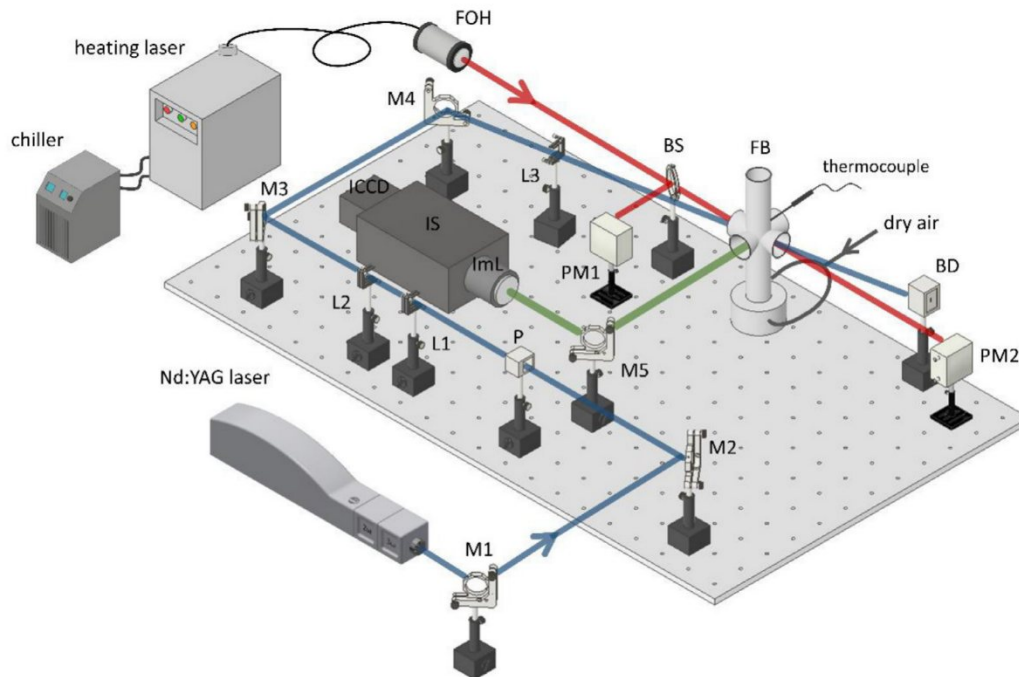


Fig. 1. Optical arrangement of the experiment. Blue line: 355 nm Nd:YAG laser beam path, Red line: heating radiation beam path, Green line: phosphorescence emission. M: mirror, P: polariser, L: lens, FOH: fiber-optic head, PM: power meter, BS: beam splitter, BD: beam dump, FB: fluidized bed, ImL: image lens, IS: image splitter.

tio of 1:1 to promote fluidization and minimize phosphor aggregation in the fluidized bed. While, SiO_2 particles do not emit any phosphorescence signal after laser excitation, they also do not generate any interference to the temperature measurement of BAM phosphors [30]. In addition, the size of SiO_2 particles is similar to the fine single phosphors, therefore, SiO_2 could escape easily from the fluidized bed with the airflow and could not be fluidized within the heating region. The low absorptance of SiO_2 particles at the spectrum range between 904.0 nm and 918.5 nm also makes them hard to be heated up by the radiation source.

An Nd:YAG (Quantel, Q-smart 850) laser, operated at $2.270 \text{ mJ} \pm 98.17 \text{ } \mu\text{J}$ and 355 nm, was used to excite the TPs within the fluidized bed. Three cylindrical lenses (L1, L2, and L3) focused the laser beam and formed a small sheet of $300 \text{ } \mu\text{m}$ thickness in the measurement region. The Nd:YAG laser sheet was aligned to intercepted with the focal region from the heating laser in the center of the fluidized bed. The excited phosphorescence emission signals from the phosphors were directed via a mirror to the imaging system through an image splitter (Cairns Research, Opto-Split II) to record two $15.0 \text{ mm} \times 10.5 \text{ mm}$ sub-images onto the ICCD camera (Princeton Instruments, PI-Max) with a spatial resolution of 51 pixels/mm. Both images were collected simultaneously on the same pixel array which avoids errors associated with pixel matching during the image processing. Two high transmission ($>93\%$) interference filters, at $400 \pm 20 \text{ nm}$ (Semrock, FF01-400/40-25) and $460 \pm 7 \text{ nm}$ (Semrock, FF01-460/14-25), were chosen to select two parts of the BAM phosphorescence emission signal. The images were collected after a 45 ns delay from the excitation laser over a 1700 ns gate width to make good use of the long phosphorescent emission signal. The intensity ratio, $\frac{I_{400}}{I_{460}}$, was calculated at each pixel by superposition and dividing the intensity of two sub-images on a pixel-by-pixel basis.

The BAM phosphor temperature was related to the phosphorescence emissions by calibration. The calibration process used a similar experimental arrangement to the actual measurement, except that the fluidized bed was replaced by an oven (MTI Corporation, OTF-1200X-S). A metal plate, whose surface was coated with a thin layer of BAM phosphors and monitored by a surface-mounted K-type thermocouple, was placed in the middle of the oven. The surface was then imaged for a series of temperatures selected using the oven's controller.

The temperature of BAM phosphors is determined based on the wavelength shift of the emitted signal at different temperatures. As this wavelength shift of phosphors is only temperature dependent, the temperature measurement of BAM phosphors will not be affected by the changed solid volume fraction in calibration.

3. Results and discussion

3.1. $\text{BaMgAl}_{10}\text{O}_{17}:\text{Eu}$ properties

Fig. 2(a) presents the particle size distribution of the BAM phosphors, as measured with the dynamic light scattering (DLS) method (Malvern, Mastersizer 2000). It can be seen that the separated BAM phosphors have a log-normal size distribution with a mean diameter of $9.2 \text{ } \mu\text{m}$. Fig. 2(b) and (c) present images of the phosphors obtained with a scanning electron microscope (Philips, SEM XL-30) at two resolutions. It can be seen that the phosphors are both irregular-shaped and tend to aggregate. The size of the aggregates is typically an order of magnitude larger than that of the individual phosphor particles but were not measured statistically.

3.2. Laser-induced phosphorescence spectra

Fig. 3(a) presents five typical examples of the phosphorescence emission obtained with a spectrometer (Princeton Instruments, Acton Series Spectrograph) at temperatures 294 K, 515 K, 696 K, 900 K, and 1105

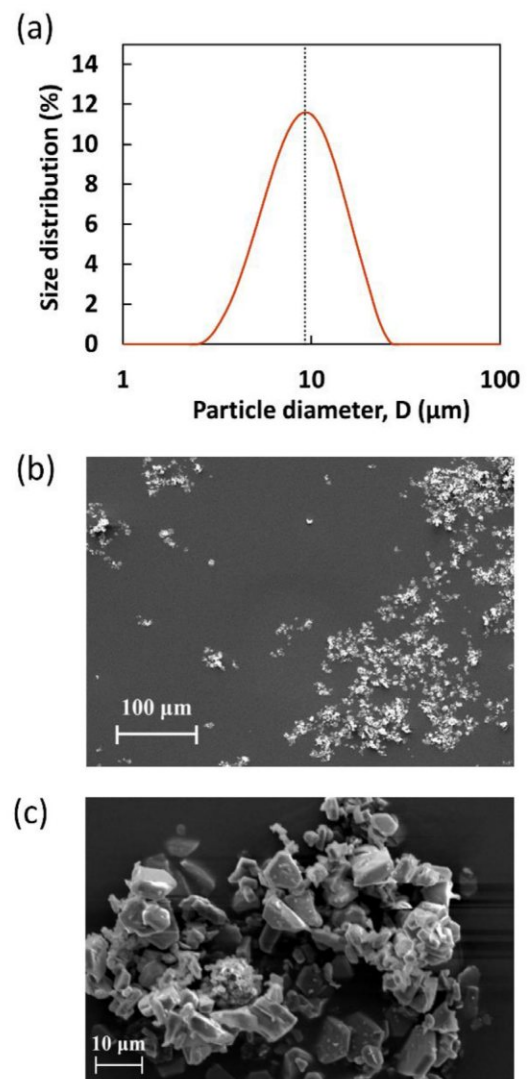


Fig. 2. Images of (a) the BAM phosphor size distribution as measured with DLS analysis, (b) a series of phosphors as obtained with SEM photography, and (c) a higher resolution SEM image of aggregates with a complex structure.

K using the calibration oven. Fig. 3(b) presents the corresponding normalized spectral emissions. Fig. 3(a) shows that a decrease in the phosphorescence emission signal intensity occurs with respect to increasing temperature. From Fig. 3(b), the wavelength of emission peak remains at 440 nm, but the width of the distribution becomes broader and shifts towards shorter wavelengths. That is, the spectrum exhibits a temperature sensitivity within the recorded temporal range. In addition, the normalized intensity at a wavelength around 460 nm almost remains unchanged with temperature, while that at 400 nm exhibits an obvious increase. This demonstrates that the ratio of the signals obtained 460 nm to that at 400 nm can be used to provide a measurement of temperature, consistent with previous investigations [19]. From this, two narrowband interference filters with bandwidths centered at $400 \pm 20 \text{ nm}$ and $460 \pm 7 \text{ nm}$ were selected for the temperature measurement. The shaded regions in Fig. 3(b) indicate the wavelength range of these two filters.

3.3. Temperature calibration

The calibration of BAM temperatures as the function of phosphorescence emission properties was conducted for temperature ranges between 295 K and 1105 K by using the two interference filters (400

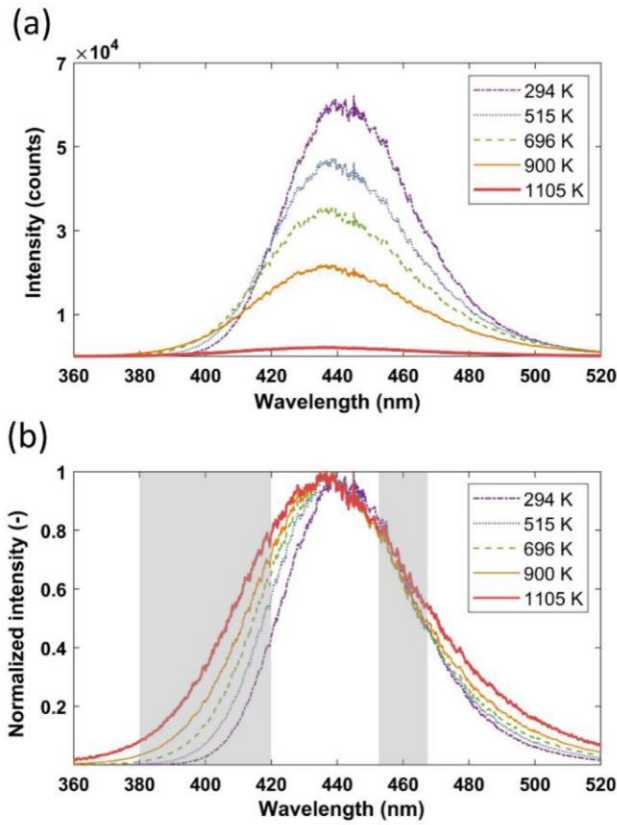


Fig. 3. The BAM spectra emission (a) as a function of wavelength at 5 different temperatures and (b) after normalized by maximum intensity at each temperature. The two shaded regions in (b) indicate the wavelength range of the two filters centered at 400 ± 20 nm and 460 ± 7 nm.

nm and 460 nm) in the image splitter. This performed using the metal plate coated with a thin and homogeneous layer of BAM phosphors in a temperature-controlled oven as described above. Nineteen sets of temperature measurements were performed, with 100 were recorded for each set after the BAM-coated plate had reached thermal equilibrium. The intensity ratio of the emitted phosphorescence at the two wavelength bands, $\frac{I_{400}}{I_{460}}$, was calculated by dividing two sub-images pixel-by-pixel. This was normalized by the intensity ratio calculated at room temperature to eliminate uncertainty caused by the background.

Fig. 4 shows the resulting calibration curve of the BAM phosphors, using error-bars magnified by a factor of three to allow them to be visualized. These error bars indicate the range of intensity ratio measured over the 100 images at each temperature. The accuracy of the calibration was maintained within an error range of $\pm 5\%$. The relationship between the intensity ratio, $\frac{I_{400}}{I_{460}}$, and temperature can be described by a fourth-order polynomial with a confidence level of 95% and an R-squared value of 0.998 as follows:

$$T(K) = 44 \left(\frac{I_{400}}{I_{460}} \right)^4 - 479 \left(\frac{I_{400}}{I_{460}} \right)^3 + 1777 \left(\frac{I_{400}}{I_{460}} \right)^2 - 2316 \left(\frac{I_{400}}{I_{460}} \right) + 1268. \quad (1)$$

From the relationship, it can be seen that the increasing rate of intensity ratio according to temperature is 0.005/K within the higher temperature range from 850 K to 1250 K, while the corresponding increasing rate at the temperature range below 850 K is only 0.0025/K, a reduction of nearly half. Thus, the intensity ratio of BAM phosphors is more sensitive at temperature values above 850 K, which provides the confidence of its feasibility to perform more accurate measurements at higher

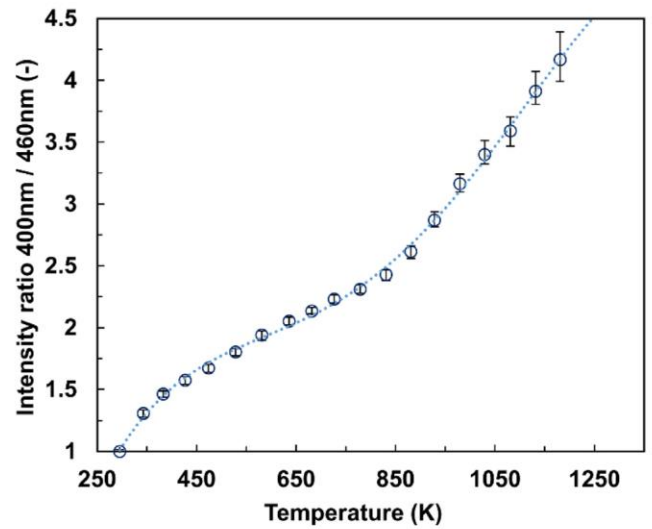


Fig. 4. BAM calibration by 2D images indicating the relationship between temperature and intensity ratio. These error bars are magnified by a factor of 3 for the purpose of visualization.

temperatures. The calibration equation was then used to infer the temperature of mobile BAM phosphors in the subsequent measurements in the fluidized bed.

3.4. In situ temperature measurements

To demonstrate the real-time single-shot BAM temperature measurement, BAM aggregates were radiatively heated within the moving environment of the fluidized bed using the system shown in Fig. 1. For each flux, 300 images were recorded with the ICCD camera after the system had reached a steady state. The system was cooled back to room temperature (295 K) before any subsequent measurements.

Fig. 5 presents a series of typical images of BAM aggregates as obtained for four values of heat fluxes, namely at 0 MW/m² (at room temperature without any heating), 11.12 MW/m², 19.92 MW/m², 28.87 MW/m². Column A and column B present the images of individual aggregates images as recorded through the 400 ± 20 nm filter and 460 ± 7 nm filter, respectively, while column C presents the derived temperature image of the particle after application of the calibration equation Eq. (1). It can be seen that the signal intensity of aggregates images taken through both filters decreases with an increase in the heat flux, while the inferred particle temperature increases. This is consistent with Fig. 3. Furthermore, for the highest heat flux of 28.87 MW/m², the maximum temperature of the aggregate was 1063 K. This is almost 400 K higher than the maximum temperature of 650 K recorded with ZnO:Zn aggregates in a previous study [28]. This result confirms that the BAM phosphors are able to be used to measure at higher temperatures in a suspended environment than ZnO:Zn phosphors, which is consistent with the studies conducted by Särner et. al. [31].

The signal-to-noise ratio (SNR) for the images taken with the 400 ± 20 nm filter varied between 15 at without heat flux and 3.5 at a heat flux of 28.87 MW/m², while the SNR for the images taken with the 460 ± 7 nm filter varied from 28 at without heat flux to 5.1 at a heat flux of 28.87 MW/m². It makes the derivation of the aggregate temperature is reliable. The SNRs for the images recorded at both 400 ± 20 nm and 460 ± 7 nm are decreased with increasing heat flux, and 460 ± 7 nm presents a more significant decrease comparing with 400 ± 20 nm. This is contributed by the decrease in phosphorescence emission signal intensity and the shift of emission at high temperature, which is shown in Fig. 3. On the other hand, for ZnO:Zn phosphors, the SNR has a converse changing trend as a function of heat flux between two sub-images, i.e., the SNR for the images recorded at 392 ± 9 nm is decreased with increasing heat

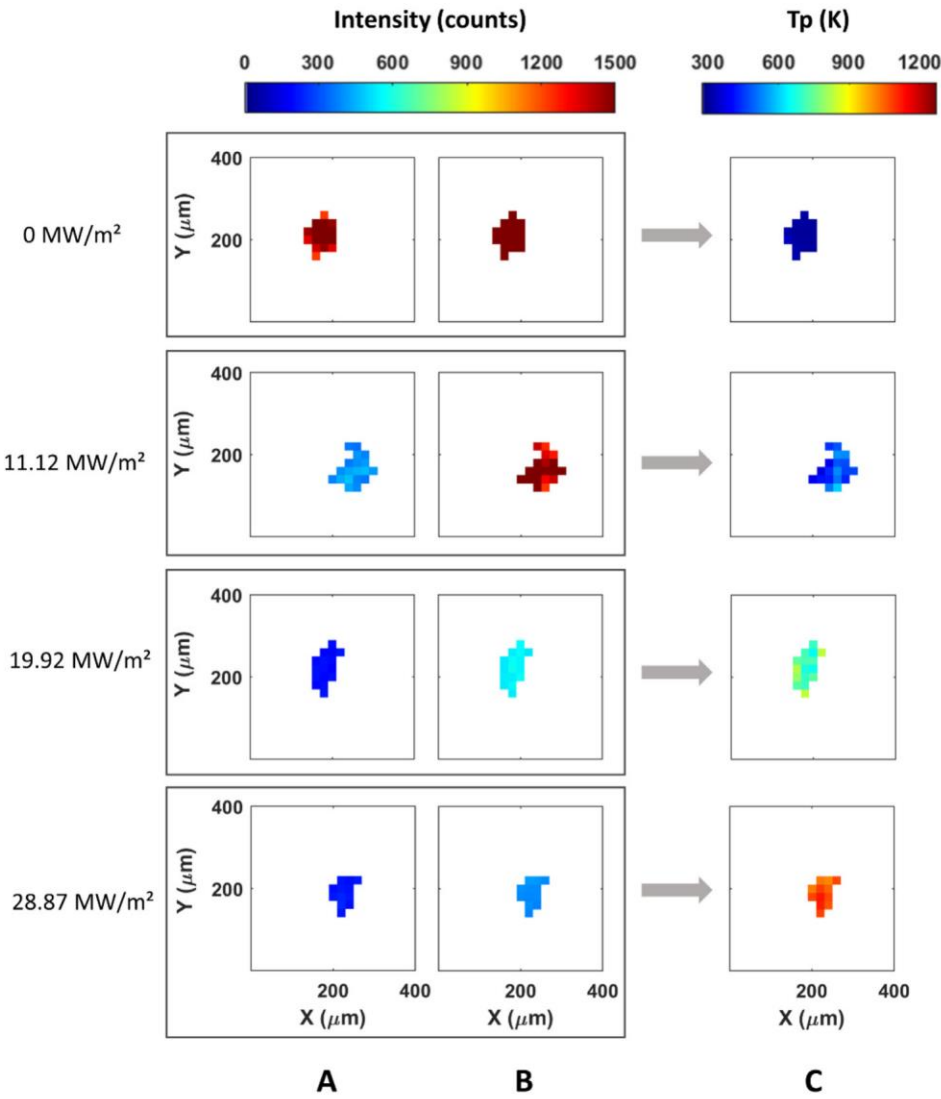


Fig. 5. Typical example of single-shot aggregate temperature distribution images (column C), derived from the two corresponding raw sub-images at 400 ± 20 nm (column A) and 460 ± 7 nm (column B) for four values of heat flux: 0 MW/m^2 , 11.12 MW/m^2 , 19.92 MW/m^2 and 28.87 MW/m^2 .

flux, while that at 440 ± 20 nm is increased with increasing heat flux [28]. This different SNR change trend of BAM and ZnO:Zn aggregates with respect to the temperature is due to their converse emission shift at high temperature, where BAM aggregates experiences a shift towards shorter wavelength while ZnO:Zn shifts towards longer wavelength.

In addition, it can be seen from Fig. 5 that the phosphors are non-spherical and of much larger size than a single BAM particle, as measured from Section 3.1. This is attributed to the aggregation of phosphors during fluidization, which is true for most phosphors in real flows. Furthermore, from Column C of Fig. 5, some variations can be seen in the temperature at different regions of the imaged aggregates. This is attributed to a combination of measurement noise from the ICCD and to genuine differences caused by the non-uniformity of the aggregate surfaces. Further analysis of these differences can be explored in the future.

Fig. 6 presents the superposition of the measured aggregate temperature in the measurement area over 300 images. The temperature of each aggregate was determined using the intensity ratio method as presented in Fig. 5. Then, the temperature distribution of all BAM aggregates was obtained by overlapping all aggregates temperatures over 300 images. The average value was applied when different aggregates were in the same position. When increasing the heat flux, more aggregates with high temperatures are presented. The aggregates were fluidized from bottom to top, more hot aggregates observed in the upper measurement area are also caused by their longer path length and longer residence time within the heating region.

Fig. 7 presents probability distributions of the measured aggregate temperature over 300 images and the corresponding probability density functions (PDFs) as a function of heat flux, ranging from 4.48 MW/m^2 to 27.28 MW/m^2 . The gamma distribution [32] was applied to describe the probability distribution of measured aggregate temperature at each heat flux case. It is clear to see that as the heat flux increasing from 4.48 MW/m^2 to 27.28 MW/m^2 , the probability of aggregate temperature reaching higher temperatures is increased consistently. The average temperature of BAM aggregates is approximately located in the peak of the distribution.

The larger value of dispersion was found in the wider temperature distribution under higher-flux environments is caused by the elevated temperature of cooling air reducing its cooling ability. Under low-flux radiation, the BAM phosphors were heated by the radiation and cooled down by the fluidized airflow. However, the temperature of air was increased along with the increased radiation flux. According to the convection heat transfer equation, the total heat loss rate from the surfaces of BAM aggregates, \dot{Q} , depends on the temperature drop between the aggregates and the cooling air, $T_{BAM} - T_{air}$:

$$\dot{Q} = h_{conv} \cdot A \cdot (T_{BAM} - T_{air}), \quad (2)$$

where h_{conv} is the convective heat transfer coefficient, A is the surface area of BAM aggregates. Therefore, under high-flux radiation, some of the aggregates cannot be cooled down due to the reduction in this tem-

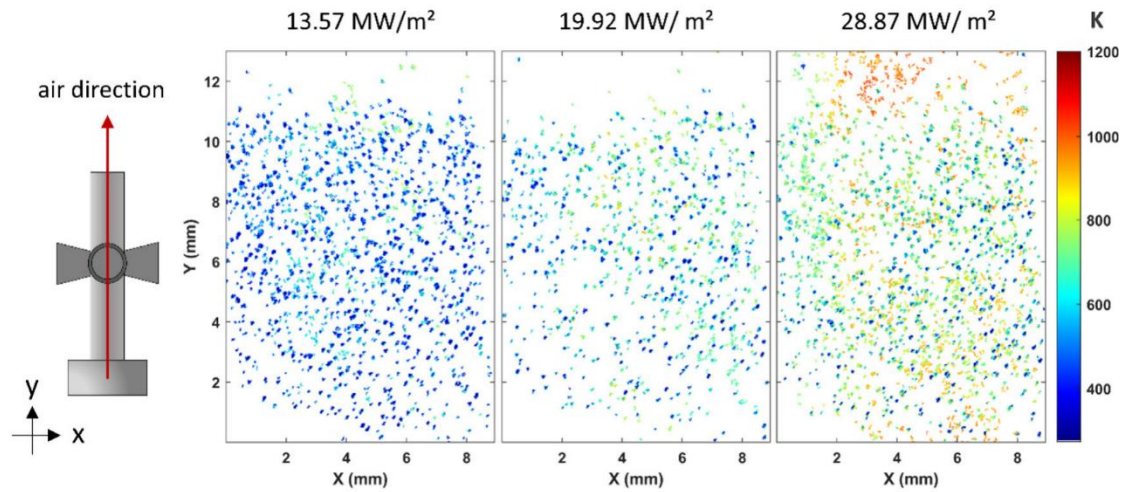


Fig. 6. Superposition of BAM aggregates temperature in the measurement area by overlapping aggregates over 300 images under three heating fluxes: 13.57 MW/m²; 19.92 MW/m²; 28.87 MW/m². The air-flow direction was along the y-axis of the fluidized bed.

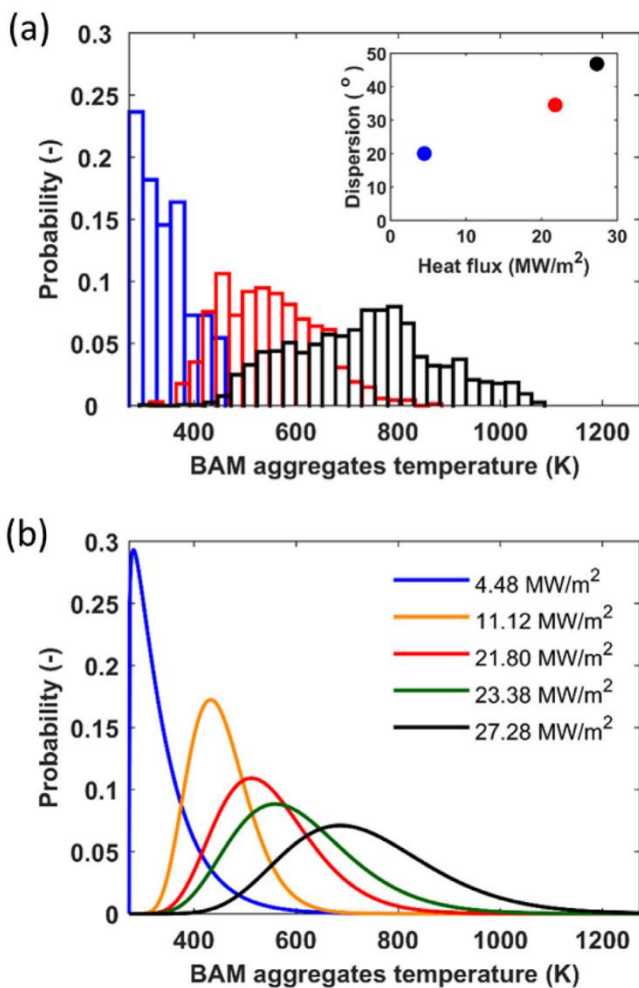


Fig. 7. (a) BAM aggregates measured temperature probability and dispersion for heat flux: 4.48 MW/m² (blue), 21.8 MW/m² (red), and 27.28 MW/m² (black); and (b) probability density functions (PDFs) of BAM temperatures as a function of heat flux, ranging from 4.48 MW/m² to 27.28 MW/m².

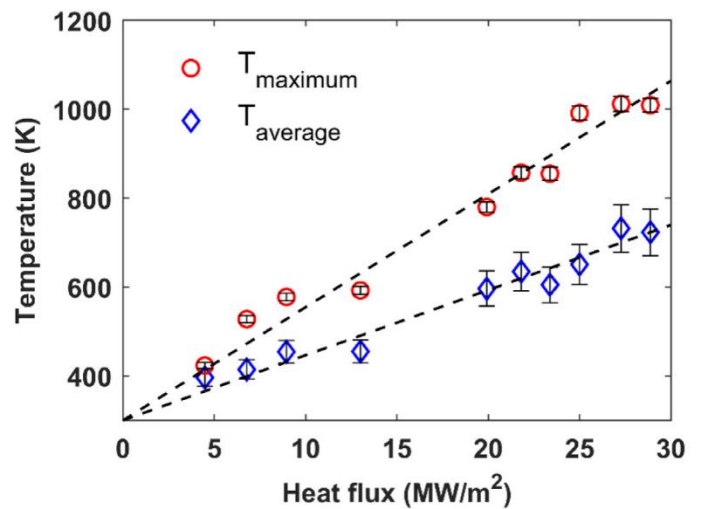


Fig. 8. The average temperature and maximum temperature of BAM aggregates derived over the entire images as a function of heat flux. The black dash lines are linear fits of the measured temperature.

perature difference rules of Eq. (2). In the absence of cooling air, this leads to the increase of average aggregates temperature producing a wider temperature distribution. In addition, the wider range of aggregates temperature is also caused by the non-uniformity of the aggregate surfaces and the unsteady flow within the fluidized bed. The variation in surface area influences the temperature of the aggregates in terms of energy absorption and convective cooling, and the unsteady flow leads to the different residence times of each aggregates within the heating region. These combined effects have significant impacts on the aggregate temperature distribution at relatively high flux environments, as shown in Fig. 7.

Fig. 8 presents the average temperature, T_{ave} , and maximum temperature, T_{max} , of all BAM aggregates for the heat flux in the range of 4.48 MW/m² and 28.87 MW/m². Here, T_{ave} was the average temperature of aggregates over 300 images recorded after the radiation was switched on, while T_{max} was adopted by the mean value of the ten highest temperatures, which were read from ten different BAM aggregates. The error bars indicate the range of aggregate temperature at each heat flux case. A range in aggregate temperatures occurs for all cases because of the variations in particle size and shape, in the local mass loading and in the residence time due to the unsteady turbulent flow within the fluidized

bed system. The particle size and shape influence the energy balance between radiant energy absorbed, transmitted, and convective cooling. The particle loading affects temperature through the apparent thermal conductivity and heat transfer coefficient of the fluid in the turbulent flow [33]. As heat flux increases, the average temperature of BAM aggregates approaches the highest value of 723 K when the heat flux is at 27.28 MW/m². Both average temperature and maximum temperature of BAM aggregates present a linear increasing trend with the increase of heat flux. The room temperature was maintained at 294 K during the experiment. The relationship between T_{ave} and heat flux, Φ , can be described by a linear fit with a confidence level of 95% and an R-squared value of 0.959 as:

$$T_{ave}(K) = 14.7 \times \Phi (MW/m^2) + T_i (K), \quad (3)$$

where T_i is the initial temperature of the aggregates, while the relationship between T_{max} and heat flux can be described by a linear fit with a confidence level of 95% and an R-squared value of 0.969 as:

$$T_{max}(K) = 25.5 \times \Phi (MW/m^2) + T_i (K) \quad (4)$$

The dependence of aggregates temperature to heat flux provides evidence that the temperature imaging method reported in this paper is reliable. The temperature of mobile phosphor aggregates in multiphase flow can be determined using the LIP technique even under high-temperature environments.

4. Conclusion

Single-shot imaging of transported BAM aggregates within a fluidized bed was demonstrated using a planar laser-induced phosphorescence technique using a single ICCD camera. The average temperature of BAM aggregates was found to vary from 404 K to 723 K as the heat flux was increased from 4.48 MW/m² to 28.87 MW/m². The variations in mass loading, aggregate surface, and residence time due to the unsteady turbulent flow caused the range in average temperatures of BAM aggregates in each flux case. The maximum temperature of single aggregates of 1063 K was found to be much higher than the maximum temperature of 650 K that recorded with ZnO:Zn phosphors in our previous study, which gives confidence that BAM phosphors can study the heat transfer process for high-temperature applications. Both average temperature and maximum temperature of BAM aggregates presented a linear increasing trend as a function of increasing heat flux. The averaged and maximum aggregates temperature increased linearly with increasing the radiation flux by a factor of 14.7 and 25.5, respectively. The probability distribution of all measured aggregate temperatures over 300 images was described by gamma distribution under each flux. The wider temperature distributions under higher radiation fluxes were caused by the elevated temperature of the cooling air and the non-uniform aggregate surfaces. The dependence of aggregates temperature to heat flux was consistent with expected trends, thus providing a further confidence that the temperature imaging method reported in this paper is reliable to measure the temperature of mobile phosphor aggregates in multiphase flows.

Declaration of Competing Interest

The authors declare that they have no known competing financial interests or personal relationships that could have appeared to influence the work reported in this paper.

CRedit authorship contribution statement

Wanxia Zhao: Methodology, Software, Investigation, Writing - original draft, Visualization. **Kimberley C.Y. Kueh:** Software, Validation, Writing - review & editing. **Graham J. Nathan:** Writing - review & editing. **Zeyad T. Alwahabi:** Conceptualization, Supervision, Writing - review & editing.

Acknowledgments

Support was received from the Australian Research Council (ARC) through the Discovery Project DP180102045 with grant number LE130100127. The authors would like to thank Mr. Jeffrey Hiorns and Mr. Jason Peak, from the mechanical workshop at the School of Chemical Engineering, for their technical support.

Supplementary materials

Supplementary material associated with this article can be found, in the online version, at doi:10.1016/j.optlaseng.2020.106398.

References

- [1] Nzihou A, Flamant G, Stanmore B. Synthetic fuels from biomass using concentrated solar energy – a review. *Energy* 2012;42(1):121–31.
- [2] Piatkowski N, Wieckert C, Weimer AW, Steinfeld A. Solar-driven gasification of carbonaceous feedstock—a review. *Energy Environ Sci* 2011;4(1):73–82.
- [3] Nathan GJ, Jafarian M, Dally BB, Saw WL, Ashman PJ, Hu E, et al. Solar thermal hybrids for combustion power plant: a growing opportunity. *Prog Energy Combust Sci* 2018;64:4–28.
- [4] Hirsch D, Epstein M, Steinfeld A. The solar thermal decarbonization of natural gas. *Int J Hydrog Energy* 2001;26(10):1023–33.
- [5] Lipiński W, Davidson JH, Haussener S, Klausner JF, Mehdizadeh AM, Petrasch J, et al. Review of heat transfer research for solar thermochemical applications. *J Therm Sci Eng Appl* 2013;5(2) 021005-021005-14.
- [6] Schaffner B, Hoffelner W, Sun H, Steinfeld A. Recycling of hazardous solid waste material using high-temperature solar process heat. 1. Thermodynamic analysis. *Environ Sci Technol* 2000;34(19):4177–84.
- [7] Meier A, Bonaldi E, Cella GM, Lipinski W, Wuillemin D. Solar chemical reactor technology for industrial production of lime. *Sol Energy* 2006;80(10):1355–62.
- [8] Maag G, Lipiński W, Steinfeld A. Particle–gas reacting flow under concentrated solar irradiation. *Int J Heat Mass Transf* 2009;52(21):4997–5004.
- [9] Schunk LO, Lipiński W, Steinfeld A. Heat transfer model of a solar receiver-reactor for the thermal dissociation of ZnO—experimental validation at 10kW and scale-up to 1MW. *Chem Eng J* 2009;150(2):502–8.
- [10] Ho CK, Iverson BD. Review of high-temperature central receiver designs for concentrating solar power. *Renewable Sustainable Energy Rev* 2014;29:835–46.
- [11] Z'Graggen A, Steinfeld A. Heat and mass transfer analysis of a suspension of reacting particles subjected to concentrated solar radiation – application to the steam-gasification of carbonaceous materials. *Int J Heat Mass Transf* 2009;52(1):385–95.
- [12] Müller R, Zedtwitz Pv, Wokaun A, Steinfeld A. Kinetic investigation on steam gasification of charcoal under direct high-flux irradiation. *Chem Eng Sci* 2003;58(22):5111–19.
- [13] Flamant G, Gauthier D, Boudhari C, Flitris Y. A 50 kW fluidized bed high temperature solar receiver: heat transfer analysis. *J Sol Energy Eng* 1988;110(4):313–20.
- [14] Flamant G, Gauthier D, Benoit H, Sans J-L, Garcia R, Boissière B, et al. Dense suspension of solid particles as a new heat transfer fluid for concentrated solar thermal plants: on-sun proof of concept. *Chem Eng Sci* 2013;102:567–76.
- [15] Alalomhoda F, Shamiri A, Hussain MA, Sotudeh-Gharebagh R, Mostoufi N. Early detection of agglomeration in a polyethylene fluidized bed at high temperature and pressure by vibration signature analysis. *Chem Eng Res Des* 2015;104:156–63.
- [16] Guo F, Dong Y, Dong L, Guo C. Effect of design and operating parameters on the gasification process of biomass in a downdraft fixed bed: an experimental study. *Int J Hydrog Energy* 2014;39(11):5625–33.
- [17] Rodriguez P, Causat B, Ablitzer C, Iltis X, Brothier M. Fluidization and coating of very dense powders by fluidized bed chemical vapour deposition. *Chem Eng Res Des* 2013;91(12):2477–83.
- [18] Kumar M, Shakher C. Measurement of temperature and temperature distribution in gaseous flames by digital speckle pattern shearing interferometry using holographic optical element. *Opt Laser Eng* 2015;73:33–9.
- [19] Aldén M, Omrane A, Richter M, Särner G. Thermographic phosphors for thermometry: a survey of combustion applications. *Prog Energy Combust Sci* 2011;37(4):422–61.
- [20] Xiao JS, Wei JB, Shaw BD, Peng Z. Temperature and fiber optic spectroscopy composition measurements of heated propanol–acetone droplets. *Opt Laser Eng* 2009;47(11):1266–72.
- [21] Alaruri S, Bonsett T, Brewington A, McPheeters E, Wilson M. Mapping the surface temperature of ceramic and superalloy turbine engine components using laser-induced fluorescence of thermographic phosphor. *Opt Laser Eng* 1999;31(5):345–51.
- [22] Brübach J, Pflitsch C, Dreizler A, Atakan B. On surface temperature measurements with thermographic phosphors: a review. *Prog Energy Combust Sci* 2013;39(1):37–60.
- [23] Fletcher TH. Time-resolved particle temperature and mass loss measurements of a bituminous coal during devolatilization. *Combust Flame* 1989;78(2):223–36.
- [24] Khatami R, Stivers C, Joshi K, Leventis YA, Sarofim AF. Combustion behavior of single particles from three different coal ranks and from sugar cane bagasse in O₂/N₂ and O₂/CO₂ atmospheres. *Combust Flame* 2012;159(3):1253–71.
- [25] Kueh KCY, Lau TCW, Nathan GJ, Alwahabi ZT. Non-intrusive temperature measurement of particles in a fluidised bed heated by well-characterised radiation. *Int J Multiphase Flow* 2018;100:186–95.

- [26] Abram C, Fond B, Heyes AL, Beyrau F. High-speed planar thermometry and velocimetry using thermographic phosphor particles. *Appl Phys B* 2013;111(2):155–60.
- [27] Jovicic G, Zigan L, Will S, Leipertz A. Phosphor thermometry in turbulent hot gas flows applying Dy:YAG and Dy:Er:YAG particles. *Meas Sci Technol* 2014;26(1):015204.
- [28] Kueh KCY, Lau TCW, Nathan GJ, Alwahabi ZT. Single-shot planar temperature imaging of radiatively heated fluidized particles. *Opt Express* 2017;25(23):28764–75.
- [29] Alwahabi ZT, Kueh KC, Nathan GJ, Cannon S. Novel solid-state solar thermal simulator supplying 30,000 suns by a fibre optical probe. *Opt Express* 2016;24(22):1444–53.
- [30] Lindén J, Takada N, Johansson B, Richter M, Aldén M. Investigation of potential laser-induced heating effects when using thermographic phosphors for gas-phase thermometry. *Appl Phys B* 2009;96(2):237–40.
- [31] Sarner G, Richter M, Alden M. Investigations of blue emitting phosphors for thermometry. *Meas Sci Technol* 2008;19(12):125304–13.
- [32] Gilpin RK, Jaroniec M, Martin-Hopkins MB. Use of a gamma energy distribution to model the gas chromatographic temperature dependence of solute retention on aryl-siloxane chemically modified porous carbon. *J Chromatogr A* 1990;513:1–11.
- [33] Yang Y, Zhang ZG, Grulke EA, Anderson WB, Wu G. Heat transfer properties of nanoparticle-in-fluid dispersions (nanofluids) in laminar flow. *Int J Heat Mass Transf* 2005;48(6):1107–16.

Chapter 4

Optical Properties and Scattering

Distribution of Thermographic Phosphor

Suspensions

Statement of Authorship

Title of Paper	Optical properties and scattering distribution of thermographic phosphor suspensions
Publication Status	<input type="checkbox"/> Published <input type="checkbox"/> Accepted for Publication <input checked="" type="checkbox"/> Submitted for Publication <input type="checkbox"/> Unpublished and Unsubmitted work written in manuscript style
Publication Details	Submitted to Optical Materials.

Principal Author

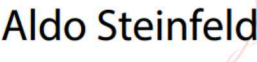
Name of Principal Author (Candidate)	Wanxia Zhao		
Contribution to the Paper	Performed experiments, analysed results, interpreted data and wrote manuscript.		
Overall percentage (%)	70		
Certification:	This paper reports on original research I conducted during the period of my Higher Degree by Research candidature and is not subject to any obligations or contractual agreements with a third party that would constrain its inclusion in this thesis. I am the primary author of this paper.		
Signature		Date	03/07/20

Co-Author Contributions

By signing the Statement of Authorship, each author certifies that:

- i. the candidate's stated contribution to the publication is accurate (as detailed above);
- ii. permission is granted for the candidate to include the publication in the thesis; and
- iii. the sum of all co-author contributions is equal to 100% less the candidate's stated contribution.

Name of Co-Author	Jan Marti		
Contribution to the Paper	Performed numerical simulations, discussed experimental results and findings.		
Signature		Date	23/07/2020

Name of Co-Author	Aldo Steinfeld		
Contribution to the Paper	Supervised the work of numerical simulations. Discussions on the project idea. Discussions on the fundamentals of radiative transfer within particle clouds. Development of the sample making process.		
Signature		Date	22/07/20

Digital unterschrieben von Aldo Steinfeld
 DN: cn=Aldo Steinfeld, o=ETH Zurich, ou,
 email=aldo.steinfeld@ethz.ch, c=CH
 Datum: 2020.07.22 13:14:47 +02'00'

Name of Co-Author	Zeyad T. Alwahabi		
Contribution to the Paper	Discussed experimental results and findings, supervised the research project, and revised the manuscript.		
Signature	Zeyad Alwahabi <small>Digitally signed by Zeyad Alwahabi DN: cn=Zeyad Alwahabi, o=University of Adelaide, ou, email=zeyad.alwahabi@adelaide.edu.au, c=AU Date: 2020.07.21 21:56:48 +09'30'</small>	Date	21/07/20

Optical properties and scattering distribution of thermographic phosphor suspensions

Wanxia Zhao^{a,b}, Jan Marti^c, Aldo Steinfeld^c, and Zeyad T. Alwahabi^{a,b,*}

^a School of Chemical Engineering and Advanced Materials, University of Adelaide, Adelaide 5005, Australia

^b Centre for Energy Technology, University of Adelaide, Adelaide 5005, Australia

^c Department of Mechanical and Process Engineering, ETH Zurich, Zurich 8092, Switzerland

* Corresponding author. E-mail address: zeyad.alwahabi@adelaide.edu.au (Z. T. Alwahabi).

Abstract

The optical properties and scattering distribution of thermographic phosphors with varying particle loadings were investigated using a combined experimental and numerical method. The laser-induced phosphorescence (LIP) technique enables non-intrusive temperature measurements under harsh conditions using thermographic phosphors. In the LIP technique, the temperature of thermographic phosphors is strongly influenced by their optical properties, scattering distribution, and light transmitted through phosphor suspensions. ZnO:Zn and BaMgAl₁₀O₁₇:Eu²⁺ (BAM) are two types of widely used phosphors due to their stable physical properties and high-temperature sensitivities. To study their inter-phosphor light transfer and provide a specification for the LIP technique, the angular scattering distribution and light propagation of these two phosphor suspensions was measured using a spectro-goniometric system. A collision-based Monte Carlo ray-tracing model was developed to extract their optical properties, including extinction coefficient, scattering albedo, asymmetry factors, and scattering fraction. With the void fraction around 0.98, the extinction coefficient of ZnO:Zn

was determined to be 4.719, while that of F grade BAM and N grade BAM were 11.584 and 9.777, respectively. In addition, BAM had a higher scattering fraction ($\alpha = 0.99$) than ZnO:Zn ($\alpha = 0.88$). Due to the higher values of extinction coefficient and scattering fraction, BAM demonstrated more significant scattering than ZnO:Zn. Light transmission through phosphor suspensions was predicted along the direction of the light path. For ZnO:Zn, 70% of flux was scattered when the distance increases to 0.5, while for BAM, the distance was 0.15. Furthermore, with the same mass loading, smaller particle sizes can promote scattering and reduce the amount of light transmitted through phosphor suspensions.

1. Introduction

Thermographic phosphors are widely employed to offer a non-invasive temperature measurement for both static and moving surfaces in various environments, like gas, droplet, and flame, based on the laser-induced phosphorescence (LIP) technique.¹⁻² Phosphors can absorb high energy and emit phosphorescence after laser excitation. These emissions from the coating of phosphors are temperature-dependent and can be utilized to determine the temperature of coated surfaces and particles-laden flows. Phosphors have been used as temperature monitors in recent decades and have been shown the feasibility to perform an accurate quantitative measurement in high-temperature reactors, such as combustion engines and gas burners.³

When using the LIP technique to perform temperature measurement under harsh conditions like flames and soot, phosphor particles also act as the medium to transfer heat between the heat source and gas flows. As the particle temperature increases, the radiation becomes the dominant form of heat transfer within the gas-particle multiphase flow. When the temperature rises from 600 to 1000 K, the contribution of radiation to heat transfer can increase from 10% to 30%, while at the temperature above 1000 K, this value can exceed 35%.⁴⁻⁵ In high-temperature processes, the particles are heated up by the radiation mainly in two ways: (1) direct radiation from the heat source; and (2) scattered radiation from the nearby particles. Therefore, the influence of particle loading on measured temperature should not be neglected.⁶ There is a need to demonstrate the scattering distribution among phosphor suspension to understand the heat transfer that existed within the particles-laden flows and provide a specification for the LIP technique.⁷

In the previous work, Zhao *et al.*⁸ performed an *in-situ* temperature measurement of suspended phosphor aggregates using the LIP technique. High flux radiation was employed as

a heat source and irradiated the phosphors suspended in a fluidized bed. The linear relationship between particle temperatures and heat flux were identified. The highest average temperature of phosphor aggregates was estimated at 723 K. The fluctuation in phosphor temperatures was caused by the variations of particle mass loading due to the unsteady flows inside the fluidized bed. However, the effect of mass loading was not investigated in this work. The attenuated and trapped light caused by the strong inter-particle heat transfer, like phosphor scattering, was not reported due to the lack of information on the optical properties of phosphors.

Recently, optical properties and light transmission have been demonstrated on various phosphor media. For example, Leung *et al.*⁹ used diffusion theory to measure light transport through phosphor plates with changing YAG:Ce³⁺ loading. The albedo is 0.7 for the light wavelength of 460 nm, independent of phosphor loading. The mean free paths of both absorption and transportation are on the order of sample thicknesses. Ma *et al.*¹⁰ developed a multi-wavelength model based on a fluorescent radiative transfer equation to simulate light absorption, scattering, and re-absorbing effects for varying phosphor layers. Their model had a good agreement of less than 7.6% deviation with experiments. Besides, Kumar *et al.*¹¹ evaluated the radiative properties, including radiative transition rates and lifetime, of Eu³⁺ doped ZnAl₂O₄. Mohapatra *et al.*¹² investigated the optical properties of LiAl₅O₈: Eu phosphors with UV excitation.

Among different thermographic phosphors, ZnO:Zn and BaMgAl₁₀O₁₇:Eu²⁺ (BAM) phosphors are two types of phosphors that are widely used in the LIP technique. For ZnO:Zn, the short lifespan of fewer than 1 ns enables the temperature measurement of fast-moving objects, which is significant for turbulent flows. For example, Kueh *et al.*⁶ reported the direct temperature measurement of individual ZnO:Zn phosphor aggregates using the LIP technique. At the radiation flux of 18.72 MW/m², the maximum temperature recorded was 738 K. In addition, BAM is another widely used phosphor, which has stable physical properties and a

strong emission line at 440 nm.¹³ Its broad temperature-sensitivity range up to 1300 K ensure that BAM cannot be damaged in high-temperature applications.¹³ However, the comprehensive study on scattering distribution and light propagation is scarcely reported for these two phosphors.

Furthermore, numerical models have been developed to determine optical properties and to study the light transfer among different mono and polydispersed particle suspensions. For example, Coquard and Baillis¹⁴ computed the optical properties of spherical particle beds based on independent scattering theory. Cunsolo *et al.*¹⁵ calculated the scattering phase function of cellular foams using Monte Carlo ray-tracing techniques. Zeghondy *et al.*¹⁶ used the Radiative Distribution Function Identification (RDFI) model to determine the extinction and absorption coefficients of high porosity materials. To confirm the robustness of modeling approaches, experiments to determine optical properties were conducted on different light-absorbing-scattering media. The literature covers the extinction coefficient determination of packed-beds,¹⁷ the asymmetry factor characterization of ceramic foams,¹⁸⁻¹⁹ and the scattering analysis of dispersed media.²⁰ Besides, Liu and Mishchenko²¹⁻²² numerically investigated the scattering and optical cross-sections of soot clusters. They computed the scattering matrix of the aggregates and found that the effects of particle aggregation on scattering and absorption of soot clusters are important. However, numerical models usually use uniform media to simulate the light transfer through the dispersed media. Therefore, a combined experimental and numerical study on optical properties is important to be implemented to calibrate and correct the modeling results.²³⁻²⁴

The aim of this paper is to investigate the scattering distribution, light transmission, and optical properties of phosphor suspensions, involving extinction coefficient, scattering albedo, and scattering fraction, using a combined experimental and Monte Carlo method. Collimated laser modules were applied to demonstrate the effect of light trapping at room temperature.

Two types of phosphors, specifically ZnO:Zn and BaMgAl₁₀O₁₇:Eu²⁺ (BAM), were selected as the surveyed particles. The phosphors with different mass loadings were homogeneously suspended in transparent epoxy resin as the experimental samples to study the effect of suspension void fractions. A spectro-goniometric experimental setup was developed to collect the scattering signals from the surface of phosphor suspensions multi-angularly in both forward and backward directions. The measured signals were applied to fit the modeling. A validation study using polystyrene latex beads served to confirm the accuracy of the numerical approach. The representative results were discussed by comparing the scattering behaviors between different phosphors types, particle sizes, void fractions, and sample thicknesses. Results obtained in this work can provide a specification for the LIP technique using thermographic phosphors and be used to study the light transfer among particle suspensions.

2. Experiment approach

A schematic of the experimental setup in this study is illustrated in Figure 1. The system mainly consists of a light source, a system arrangement, a sample, and a signal measurement sensor. The phosphors with different particle sizes and loading were homogeneously suspended in the transparent epoxy resin between two microscopy slide glasses as the experimental samples. Four collimated laser modules with different wavelengths at 532 nm, 635 nm, 808 nm, and 980 nm were selected as the radiation light source. The laser beam passes were modulated by a mechanical chopper at 140 Hz to eliminate the background room light. After reflected by two mirrors (M1 and M2), the pulsed light passed the samples of thermographic phosphor suspensions. The lens pair (L1 and L2) with the focal length of 200 mm and 75 mm was used to capture the leaving radiation followed by refocusing it onto the sensor. A lens pair and a signal sensor were fixed on a rotary arm to conduct angular measurements for the incoming

light signal. This angular measurement was performed from 0° up to 165° with an interval of 15° to capture the scattering signal forward and backward. The observed intensity received by the signal power sensor (Thorlabs, SE120C) was measured by a power meter (Thorlabs, PM320E) and then delivered to a computer for data acquisition purposes. The measured intensity was normalized by the reference signal, I_0 , which is measured at the viewing angle of 0° for the sample without particles. The measurement of the power meter was triggered by the frequency of the mechanical chopper.

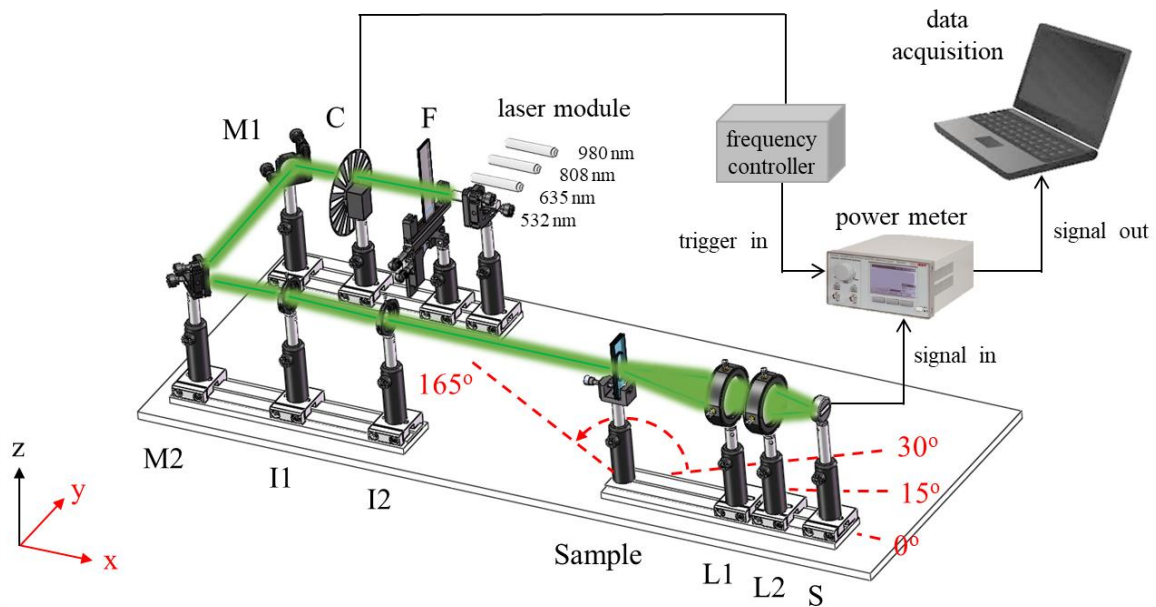


Figure 1: Experiment setup for forward and backward scattering measurement. The measurement angle is from 0° to 165° with an interval of 15° on the xy -plane. F: filter, C: mechanical beam chopper, M: mirror, I: iris, L: lens, S: signal sensor, green line: laser beam.

Two thermographic phosphors, ZnO:Zn and $\text{BaMg}_2\text{Al}_{10}\text{O}_{17}:\text{Eu}^{2+}$ (BAM) (Phosphor Technology, UK) were selected as the surveyed particles to make samples. For BAM phosphors, two different grades (F grade and N grade) were used to investigate the impact of

size. The particle size distribution of ZnO:Zn and BAM phosphors were measured by the dynamic light scattering (DLS) (Malvern, Mastersizer 2000) and presented in Figure 2. The mean, median by volume (D50), D10, and D90 diameter of all particles are listed in Table 1. All three types of particles presented a log-normal size distribution, and the mean diameter was 21.9 μm for ZnO:Zn, 4.8 μm for F grade BAM, and 9.2 μm for N grade BAM phosphors.

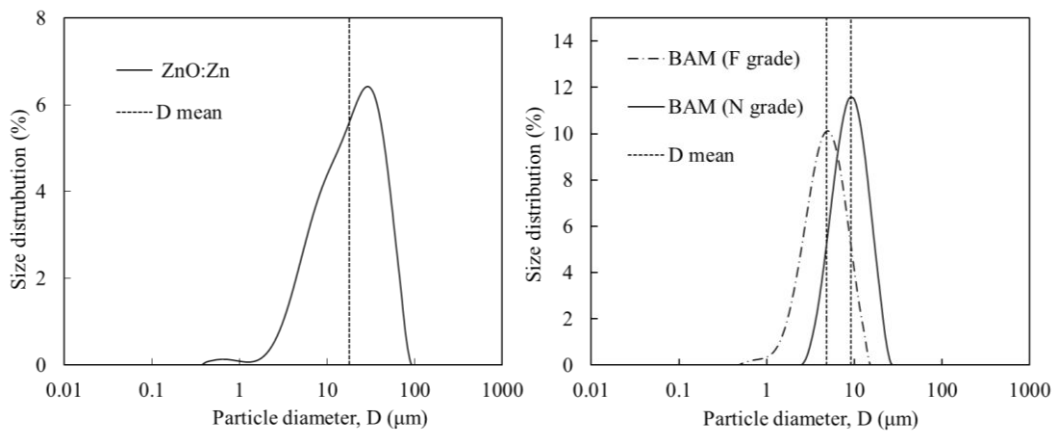


Figure 2: Particle size distributions of ZnO:Zn and BAM (F and N grade) phosphors with indicated mean diameters.

Table 1: Measured particle diameters of ZnO:Zn and BAM phosphors.

	ZnO:Zn (μm)	BAM (F grade) (μm)	BAM (N grade) (μm)
Mean diameter, D	21.8	4.8	9.2
Median diameter by volume, D50	17.9	4.4	8.5
D10	5.0	2.1	4.7
D90	45.1	8.3	14.8

The particles were homogeneously mixed with transparent epoxy resin (Jinhua Electronic Materials, China). Then the mixture was placed between two microscopy glass

slides with dimensions of $75 \times 25 \times 1$ mm, followed by 24 h drying. The small air bubbles introduced into the sample during the mixing process were removed by a vacuum pump. Sample thickness, t , was controlled by the spacer discs that were fixed between two glass slides. The small sample thicknesses, which ranged from 0.2 mm to 1.5 mm, allowing sufficient laser radiation was able to pass through the phosphor suspension and then observed by the sensor. Two side edges of the sample were covered by black opaque tape to stop the escaped radiation from the sides of glass slides. The internal reflection of glass slides was able to interfere with the detected signal especially when the measurement angle approaching 90° . The void fraction, ε , was calculated based on the mass and density of particles and epoxy resin using the following equation:

$$\varepsilon = 1 - \frac{\frac{m_P}{\rho_P}}{\frac{m_E}{\rho_E} + \frac{m_P}{\rho_P}} \quad (1)$$

where m_P and ρ_P are the mass and density of phosphors particles, while m_E and ρ_E are the mass and density of epoxy resin, respectively. The particle loading could be expressed by $1 - \varepsilon$. The thicknesses and void fractions of all samples produced for the investigation are listed in Table 2.

Table 2: Sample void fraction and thickness of ZnO:Zn and BAM (F and N grade) particle suspensions. The measurement uncertainty is ± 0.005 in the void fraction and ± 0.03 in the sample thickness.

Phosphors	Void fraction, ε (-)	Thickness, t (mm)
ZnO:Zn	0.995	0.51, 1.05, 1.50
	0.985	0.51, 1.03, 1.52
	0.975	0.21, 0.50, 1.12
	0.965	0.21, 0.48, 0.68
BaMgAl ₁₀ O ₁₇ :Eu ²⁺ (F grade)	0.995	0.23, 0.51, 0.70
	0.991	0.13, 0.30, 0.51
	0.985	0.20, 0.32, 0.50
BaMgAl ₁₀ O ₁₇ :Eu ²⁺ (N grade)	0.990	0.15, 0.30, 0.52
	0.980	0.15, 0.31, 0.52
	0.972	0.15, 0.32, 0.49

3. Modeling approach

The optic properties, including scattering albedo ω , extinction coefficient β , and approximate scattering phase function Φ , of phosphor suspensions, were determined based on the radiative transport equation (RTE):²⁵

$$\frac{dI}{ds} = \kappa_r I_{br} - \beta_r I_r(\hat{s}) + \frac{\sigma_{sr}}{4\pi} \int_0^{4\pi} I_r(\hat{s}') \Phi_r(\hat{s}', \hat{s}) d\Omega' \quad (2)$$

where I is the intensity within the phosphors suspensions in the direction \hat{s} along with the distance s , I_{br} is the intensity of a black-body, κ_r is the absorption coefficient, σ_{sr} is the spectral scattering coefficient, and Ω is the solid angle. The term of $\beta_r I_r(\hat{s})$ accounts for the intensity decreasing due to the scattering and absorption away from the direction \hat{s} . Besides, the term $\kappa_r I_{br}$ was ignored because it applies only to hot particles.

In this modeling approach, the collision-based Monte Carlo ray-tracing method was applied with in-house code VeGaS.²⁶ The model was developed for the whole experimental setup, including the optics arrangement and the sample with two microscope glass slides. The phosphor suspensions were modeled as homogeneous radiation scattering media. The light path is affected by the optical equipment. Therefore, each part of the experimental setup needs to be modeled with its location precisely. The laser radiation was approximated as a collimated circular light source with a diameter of 3.5 mm. The microscope glass slide was modeled as a double-layer Fresnel surface. The parameters of β , ω , and Φ were used as inputs of radiation properties, and the light path was calculated at least 5×10^6 stochastic rays for each set of input parameters.

The scattering of large particles normally has a strong peak in forward directions and can be described by the Henyey–Greenstein (HG) phase function as:²⁷

$$\Phi_{HG}(\theta_s, g_f) = \frac{1-g_f^2}{(1+g_f^2-2g_f \cos \theta_s)^{\frac{3}{2}}} \quad (3)$$

where θ_s is the scattering angle and g_f is the asymmetry factor of the forward peak, which is between 0 and 1. HG phase function can be improved in the double Henyey–Greenstein (DHG) phase function by combing the backward scattering peak. This is defined as:²⁸

$$\Phi_{DHG}(\theta_s, g_f, g_b, \alpha) = \alpha \Phi_{HG}(g_f, \theta_s) + (1 - \alpha) \Phi_{HG}(g_b, \theta_s) \quad (4)$$

where α is the forward scattered fraction and g_b is the asymmetry factor of the backward peak.

The extinction coefficient, β , is the only optical property that can be derived from a direct evaluation of the results without the need for a model and curve fitting. It can be derived from the linear fitting of the logarithmic normalized sensor signal and different sample thicknesses at the viewing angle 0° :

$$\frac{I}{I_0} = e^{-\beta t} \quad (5)$$

where I is the intensity measured with phosphors, I_0 is the intensity measured without phosphors, and t is the sample thickness.^{25, 29}

The scattering albedo ω , extinction coefficient β , and three parameters of DHG function (α , g_b and g_b) composed the independent parameters in the Monte Carlo simulation in this study and were turned stepwise. The modeled intensity distributions of different phosphor suspension samples were compared with the experimental results.

The modeling validation was conducted by polystyrene latex beads (Sigma-Aldrich, United States) with good sphericity. The bead size was measured by DLS (Malvern, Mastersizer 2000). Figure 3 presents its uniform size distribution with a mean bead diameter of 3.1 μm . The indicated mean diameter was used as the spherical diameter in the model.

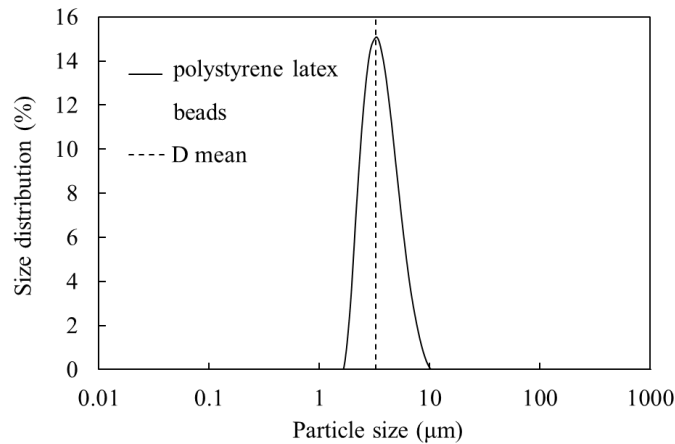


Figure 3: Particle size distribution of polystyrene latex beads with indicated mean diameter.

A computer program was devised to predict the scattering function of polystyrene latex beads by integrating their size distribution.²³ For uniform-sized spherical beads, the independent extinction coefficient can be expressed like:

$$\beta_{ind} = Q_{ext}(1 - \varepsilon) \frac{3}{4r} \quad (6)$$

where r is the particle radius and Q_{ext} equals to 2 for large particles whose the size parameter $2\pi r/\lambda \gg 1$.³⁰ For the dense beads suspension, the extinction coefficient, β , is normally assessed by applying correction terms and described as:

$$\beta = \beta_{ind}\gamma = Q_{ext}(1 - \varepsilon)\frac{3}{4r}\gamma \quad (7)$$

where γ is the scaling factor from Singh and Kaviany:³¹

$$\gamma = 1 + 1.84(1 - \varepsilon) - 3.15(1 - \varepsilon)^2 + 7.20(1 - \varepsilon)^3, \text{ for } \varepsilon > 0.3. \quad (8)$$

4. Results and discussion

For the validation process, the packed bed made of two glass slides was filled up with polystyrene latex beads suspension, which was composed mainly of spherical polymer particles and water. A small amount of surfactant was added to stabilize the suspension. The inner thickness of the packed bed was 1.67 mm, and the concentration of latex bead suspension was 3.351×10^7 beads/ml. The total volume of latex beads was calculated based on the bead size and the latex density of 1.005 g/ml. Its void fraction was determined by dividing the total volume of latex beads by the total volume of suspension liquid. The measured mean value was 0.71 ± 0.01 . The assumption of scattering albedo $\omega_L = 0.999$ was applied in the Monte Carlo ray-tracing model to effectively reduce the computational time²³. The absorption coefficient was ignored for latex beads.

Figure 4 illustrates the normalized signal of latex beads compared with the numerical model results of Monte Carlo as the function of the viewing angle. The measurement was conducted at a light wavelength of 532 nm. The scattering radiation was blocked by the sample at the viewing angle of 90° . As can be seen in the figure, the model presents a good agreement for both forward and backward scattering results. Therefore, the modeling method applied for

polystyrene latex beads is expected to determine the scattering behaviors of the ZnO:Zn and BAM phosphors samples.

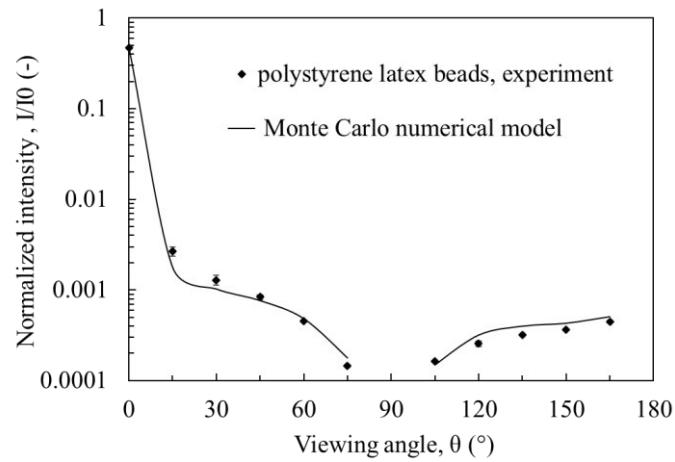


Figure 4: Normalized signal of polystyrene latex beads compared with the numerical model results of Monte Carlo at the light wavelength of 532 nm.

The dependency between the wavelength of incoming light and the detected signal intensity was tested in this study for both ZnO:Zn and BAM phosphor particles. Figure 5 presents the measured normalized signal intensity (I/I_0) as the function of the incoming light wavelength. The selected phosphor samples had a similar void fraction of around 0.985 and the sample thickness around 0.5 mm. The signals were detected at the viewing angle of 0° and 45° . As shown in the figure, there are no significant correlations between the normalized signal intensity and the light wavelength within the spectral range from 532 nm to 980 nm. The slight decrease of ZnO:Zn suspension samples at the wavelength of 980 nm might due to the reduced transmission of epoxy resin in the near-infrared region. Because of this minor spectral effect on signal intensity, all measurements in the following studies were conducted at the light wavelength of 532 nm.

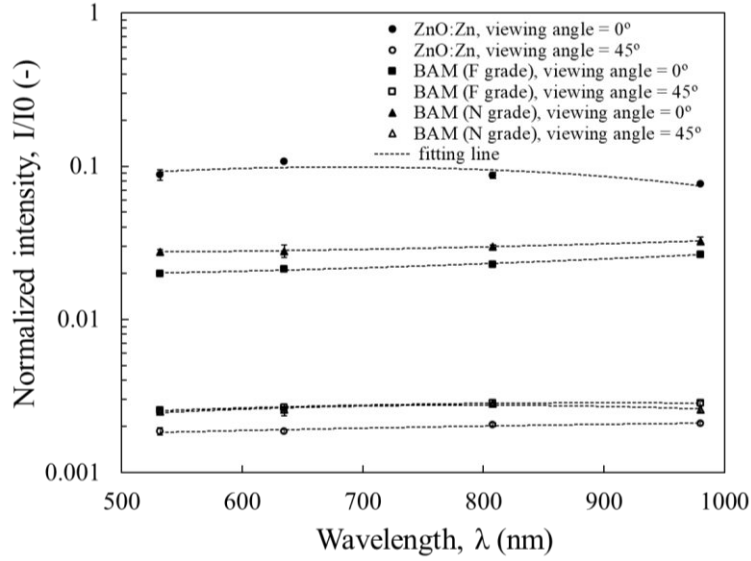


Figure 5: Normalized signal intensity at the viewing angle of 0° and 45° as the function of the incoming light wavelength for both ZnO:Zn and BAM samples whose void fraction $\varepsilon = 0.985$ and thickness $t = 0.5$ mm.

Figure 6 shows a typical example of ZnO:Zn phosphors to determine the value of β . The relationship between the logarithmic normalized sensor signal intensity and the sample thickness is presented in this figure. The measurement was conducted at a viewing angle of 0° . Three different particle loadings were investigated. The black lines indicate the respective linear fits for different samples and the β values can be derived from the linear slopes of the black lines. According to the figure, with the increase of the volume fraction of epoxy resin, the extinction coefficient increases rapidly. It shows that with the increase of the particle loading ($1 - \varepsilon$), the radiation extinction of particle suspensions is getting higher. As the extinction is the sum of absorption and scattering, thus, much light will be scattered at higher particle loading. These experimental estimated β values were used as the initial guess for the modeling approach. The same method was applied to calculate the β values for BAM phosphors. The final simulated β values which were derived from the Monte Carlo model for both ZnO:Zn and BAM phosphors are listed in Table 3, together with other radiative

parameters obtained from the numerical approach. BAM phosphors had an extinction coefficient of about 50%, which was higher than that of ZnO:Zn phosphors.

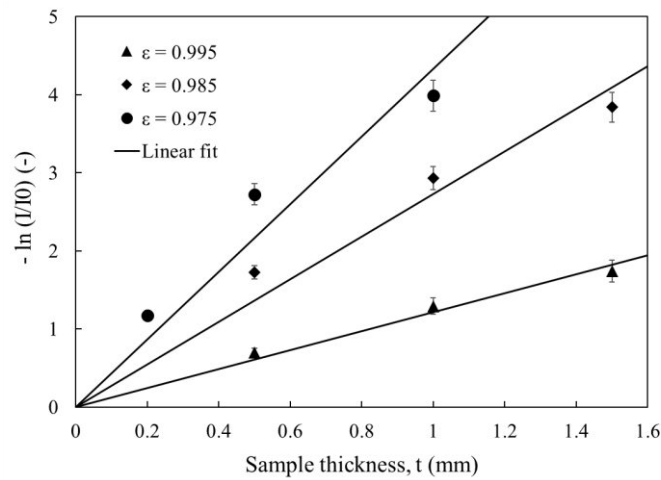


Figure 6: Logarithmic normalized signal of ZnO:Zn phosphors as a function of the sample thickness for the void fractions of 0.995, 0.985, and 0.975. The slopes of the linear fit lines indicate the values of the extinction coefficient.

Table 3: Simulated optical properties derived from the Monte Carlo model: extinction coefficient β , scattering albedo ω , asymmetry factors of forward peak g_f and backward peak g_b , and scattering fraction α for different phosphors with various particle loading.

phosphors	void fraction, ε (-)	extinction coefficient, β (mm^{-1})	scattering albedo, ω (-)	asymmetry factor of forward peak, g_f (-)	asymmetry factor of backward peak, g_b (-)	forward scattering fraction, α (-)
ZnO:Zn	0.975	7.694	1.000	0.707	0.836	0.921
	0.985	4.719	0.991	0.797	0.605	0.886
	0.995	1.791	0.997	0.875	-0.203	0.550
BAM (F grade)	0.985	11.584	0.999	0.918	-0.273	1.000
	0.991	5.810	0.999	0.887	0.773	0.981
	0.995	3.466	0.998	0.889	0.914	0.984
BAM (N grade)	0.972	15.639	0.999	0.906	-0.594	1.000
	0.980	9.777	0.999	0.902	0.691	0.994
	0.990	4.398	0.997	0.852	-0.279	1.000

Figure 7 compares the experimental normalized signal results of ZnO:Zn phosphors with the modeling results as a function of the viewing angle for various sample thicknesses and void fractions. All samples presented a similar scattering behavior with the relationship of viewing angles. An observed strong peak at the viewing angle of 0° was caused by the strong unscattered light that directly passed through the thin sample and reached the signal sensor. The viewing angle significantly influenced the experimental signal intensity. Excluding the strong peak at 0° , the normalized signal intensity of the forward scattering decreased gradually when the viewing angle increased from 15° to 75° . As the viewing angle further increased to more than 90° , the backward scattering behavior dominated the radiation process, showing the rising normalized signal intensity in the backward direction from 105° to 165° . The data at the viewing angle of 90° was ignored because the light was blocked at this location.

Additionally, the large sample thickness led to a long optical path. Therefore, when increasing the sample thickness, the decline of the intensity peak at the viewing angle of 0° is caused by the reduced transmitted light that passes through the sample with a long optical path. However, on the other hand, the larger sample thickness could enhance the diffuse scattering behavior since more particles were in the path of the light beam. It can be supported by the increased backward scattering signal for the sample with the larger thickness shown in Figure 7.

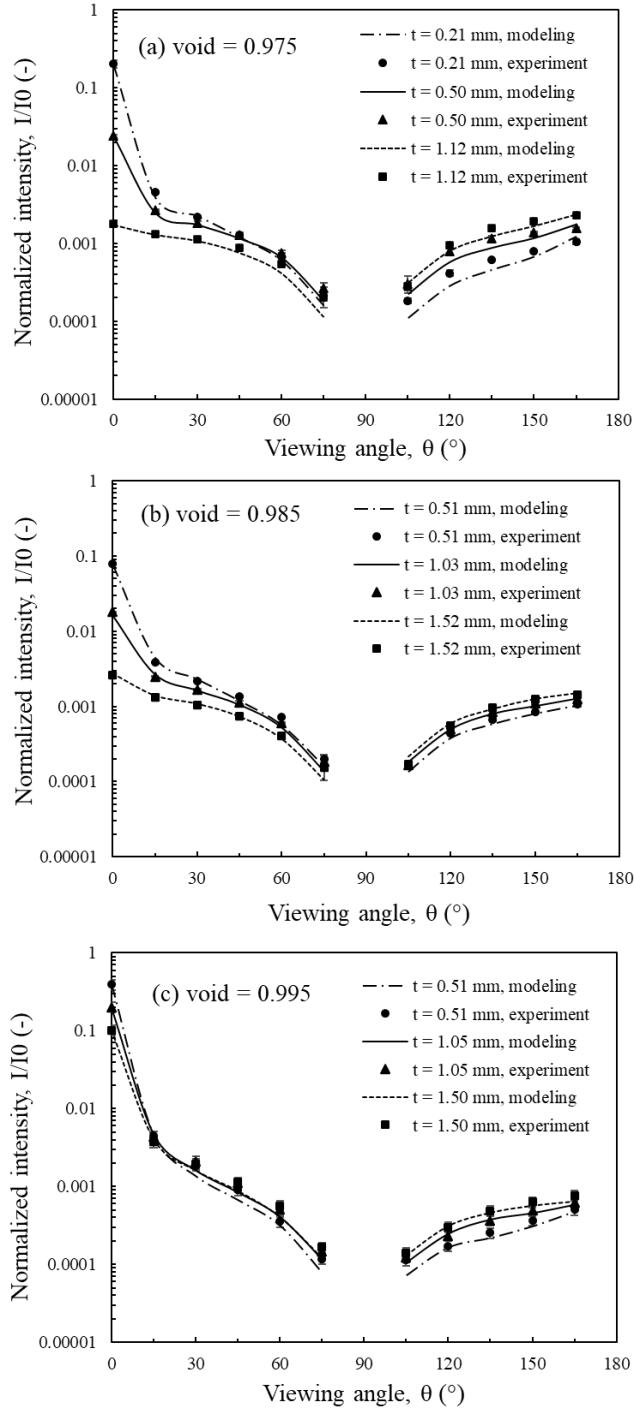


Figure 7: Experimental normalized signal of ZnO:Zn suspensions with various particle loadings ($\epsilon = 0.975$ to 0.995) and sample thicknesses ($t = 0.21$ to 1.50 mm) compared with numerical model results.

Figures 8 and 9 present the experimental and modeling normalized signal intensity results of BAM particle suspensions with different particle sizes, void fractions, and sample thicknesses. In general, BAM phosphors show a similar intensity relationship with viewing

angle as ZnO:Zn phosphors. However, it should be noted that the sample thicknesses of ZnO:Zn varied from 0.20 to 1.50 mm, while that of BAM varied only from 0.2 to 0.7 mm. Therefore, BAM phosphors presented more significant scattering behaviors than ZnO:Zn phosphors, and its scattering intensity depended more on the sample thickness than ZnO:Zn phosphors. A larger sample thickness led to a lower normalized intensity at the viewing angle of 0° but the higher intensities appeared at the following angles. This relationship became more obvious when increasing the void fraction. The good agreement between the experimental and modeling results shown in these figures further confirm the accuracy of the modeling approach in determining the optical properties.

Additionally, the accuracy of the experimental results was restricted by the detection limit of the power meter. When the scattering signal power was less than $0.1 \mu\text{W}$ whose corresponding normalized intensity was close or less than 0.0001, the detected signal was referred to as the noise level of the power meter. Consequently, a significant difference between the experiment results and modeling results could be observed at the viewing angles close to 90° where the scattering signals were relatively weak, and their corresponding normalized intensities fell to below 0.0001.

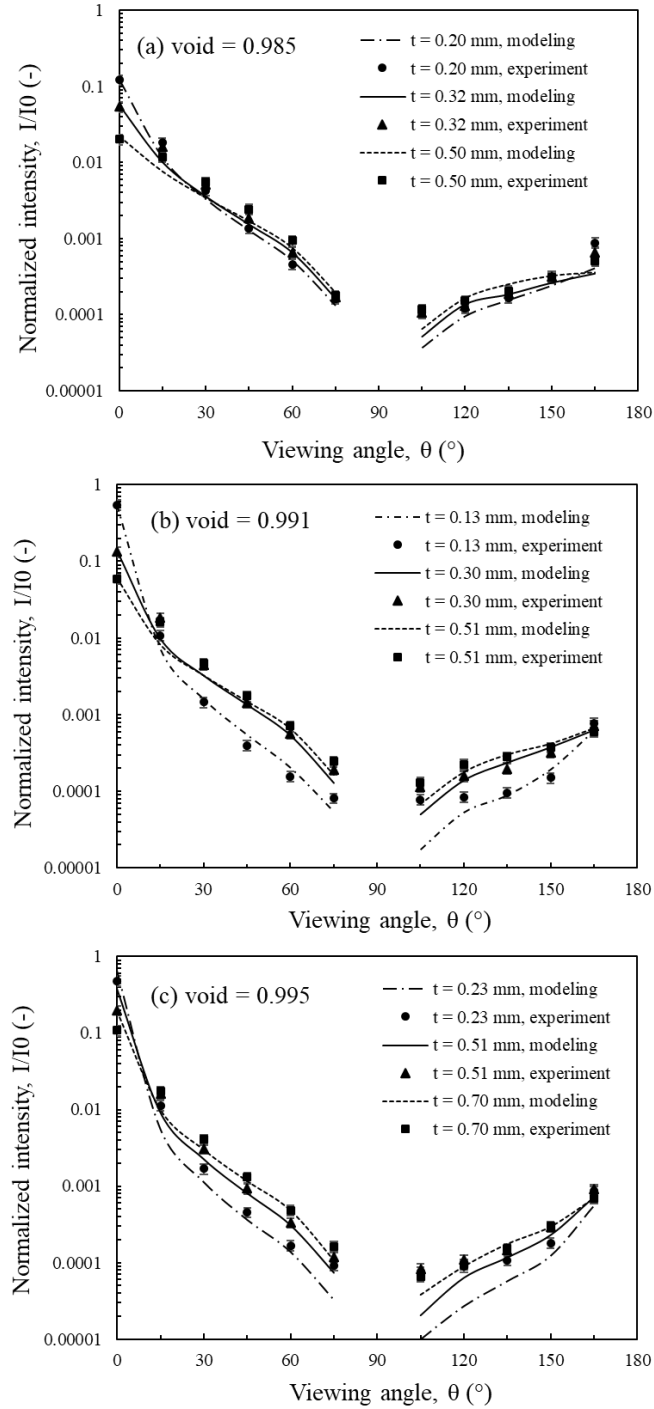


Figure 8: Normalized signal of F grade ($D = 4.8 \mu\text{m}$) BAM phosphor suspensions with various particle loadings ($\varepsilon = 0.985$ to 0.995) and sample thicknesses ($t = 0.20$ to 0.70 mm) compared with numerical model results.

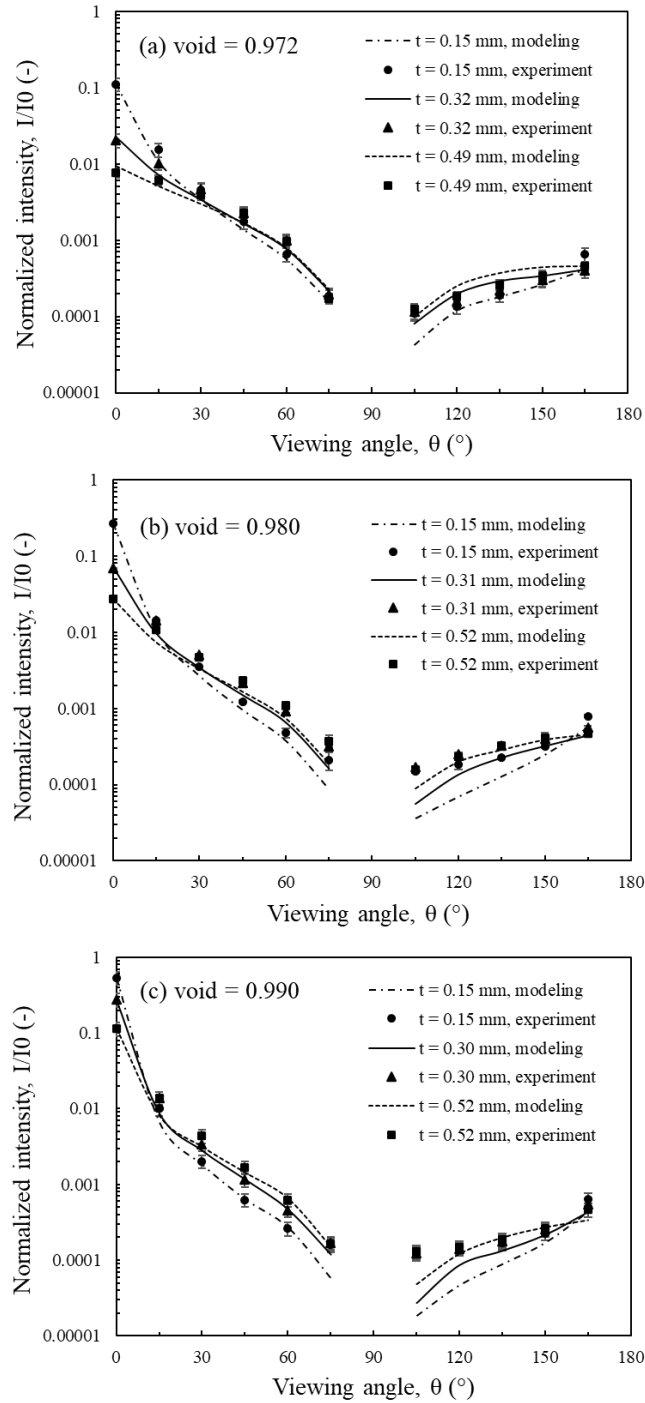


Figure 9: Normalized signal of N grade ($D = 9.2 \mu\text{m}$) BAM phosphor suspensions with various particle loadings ($\varepsilon = 0.972$ to 0.990) and sample thicknesses ($t = 0.15$ to 0.52 mm) compared with numerical model results.

Figure 10 shows the direct effect of particle loading on the detected scattering signal of ZnO:Zn phosphors and BAM phosphors (N grade). All samples' thicknesses were maintained

at around 0.5 mm. When increasing the void fraction from 0.97 to 0.99, ZnO:Zn phosphors presented a more obvious dependency of scattering behavior on particle loading than BAM phosphors. Except for the signal intensity at the viewing angle of 0° , BAM phosphors had a similar intensity between different particle loadings in both forward and backward directions. It was also supported by the similar scattering albedo values derived from the model. Besides, the total detected forward scattering signal intensity of BAM phosphors was slightly higher than that of ZnO:Zn phosphors. This behavior could be due to the increased extinction coefficient of BAM phosphors suspensions, which results in a larger scattering fraction.

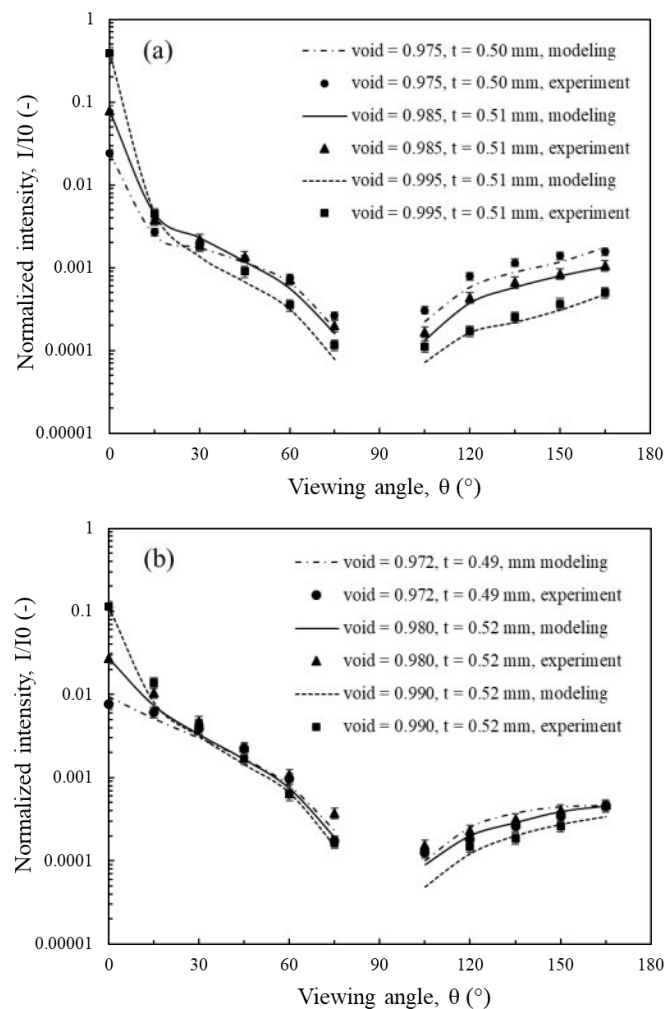


Figure 10: Comparison of the normalized signal between (a) ZnO:Zn and (b) BAM (N grade) phosphors with the same sample thickness around 0.50 mm when changing the particle loading.

Figure 11 presents the prediction of net radiation density along the direction of the light propagation path for ZnO:Zn and BAM phosphor suspensions ($\varepsilon = 0.98$). Its values were determined using the radiative transport equation (Eq. (2)) and Henyey–Greenstein (DHG) scattering phase function (Eq. (3)). The net radiation flux decreased along the light path due to the light absorbed by the particles and the accumulated scattering out of the light path. From the figure, it is observed that the net heat flux decrease of BAM phosphors is more significant than ZnO:Zn phosphors. For ZnO:Zn phosphors, around 70% of flux was scattered when the distance increases to 0.5, while for BAM phosphors, the same scattering behavior was found at the distance around 0.15. This significant scattering behavior of BAM phosphors was caused by its large extinction coefficient and large scattering fraction. Additionally, for BAM phosphors, the particles with two different sizes were selected to investigate the effect of sizes on scattering. From Figure 11(b), both particles had a very similar heat flux divergence curve, however, the particles with a smaller size presented a slightly lower net heat flux than large particles. It is evidence that smaller particles can produce more significant scattering to reduce the amount of radiation transported through the particle suspensions.

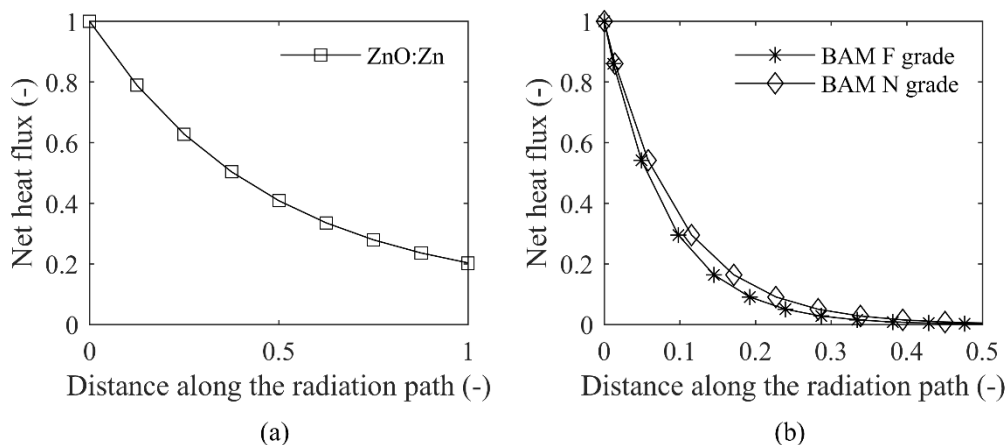


Figure 11: Net radiation density along the direction of the light path for ZnO:Zn and BAM phosphor suspensions ($\varepsilon = 0.98$).

5. Conclusion

A combination of experiments and numerical simulations was developed to investigate the optical properties of ZnO:Zn and BAM phosphors suspensions with various sample thicknesses and void fractions. The optical properties, including scattering albedo ω , asymmetry factors of forward peak g_f and backward peak g_b , and scattering fraction α , were derived from the developed collision-based Monte Carlo ray-tracing model. The simulation results were fitted by the experimental scattering radiation distributions which were measured from the viewing angle from 0° to 165° . The dependency between the wavelength of incoming light and the detected signal intensity was tested at four different wavelengths, namely 532 nm, 635 nm, 808 nm, and 980 nm, and no significant correlations between the normalized signal intensity and the light wavelength were observed. ZnO:Zn and BAM phosphors presented a similar scattering distribution, which had reduced forward scattering and increased backward scattering; however, the scattering of BAM phosphors was more dependent on solid loading. The extinction coefficient β was determined from the experimental results. With the void fraction around 0.98, the extinction coefficient of ZnO:Zn phosphors was 4.719, while that of F grade BAM phosphors and N grade BAM phosphors were 11.584 and 9.777, respectively. Thus, BAM phosphors had an extinction coefficient of about 50% higher than that of ZnO:Zn phosphors. In addition, BAM phosphors also had a higher scattering fraction ($\alpha = 0.99$) than ZnO:Zn phosphors ($\alpha = 0.88$). Due to the higher values of extinction coefficient and scattering fraction, BAM phosphors showed more significant scattering behavior than ZnO:Zn phosphors. In the prediction of radiation density transferred along the direction of the light path, 70% of net heat flux was scattered by ZnO:Zn phosphors when the light distance increased to 0.5, while for BAM phosphors, the same scattering behavior was found at the distance around 0.15. Stronger scattering behaviors were observed on the phosphors with a smaller size.

Acknowledgments

Support was received from the Australian Research Council (ARC) through the Discovery Project DP180102045.

References

1. Aldén, M.; Omrane, A.; Richter, M.; Särner, G., Thermographic phosphors for thermometry: A survey of combustion applications. *Progress in Energy and Combustion Science* **2011**, *37* (4), 422-461.
2. Abram, C.; Fond, B.; Beyrau, F., High-precision flow temperature imaging using ZnO thermographic phosphor tracer particles. *Optics Express* **2015**, *23* (15), 19453-68.
3. Jaber, A.; Zigan, L.; Sakhrieh, A.; Leipertz, A., Laser-induced Phosphorescence in Combustion Diagnostics Calibration at Extremely High Temperatures. In *11th Int. Conference on Combustion and Energy Utilization (ICCEU)*, Portugal 2012.
4. Ozkaynak, T.; Chen, J.; Frankenfield, T.; Dunii, K.; Toei, R., An experimental investigation of radiation heat transfer in a high temperature fluidized bed. *Fluidization (D Kunii, R Toei, eds.)*. *Engineering Foundation, New York* **1983**, 371-378.
5. Lee, J. C.; Han, G. Y.; Yi, C. K., Heat transfer in a high temperature fluidized bed. *Korean Journal of Chemical Engineering* **1999**, *16* (2), 260-264.
6. Kueh, K. C. Y.; Lau, T. C. W.; Nathan, G. J.; Alwahabi, Z. T., Non-intrusive temperature measurement of particles in a fluidised bed heated by well-characterised radiation. *International Journal of Multiphase Flow* **2018**, *100*, 186-195.
7. Kueh, K. C. Y.; Lau, T. C. W.; Nathan, G. J.; Alwahabi, Z. T., Single-shot planar temperature imaging of radiatively heated fluidized particles. *Optics Express* **2017**, *25* (23), 28764-28775.

8. Zhao, W.; Kueh, K. C. Y.; Nathan, G. J.; Alwahabi, Z. T., Temperature imaging of mobile BaMgAl₁₀O₁₇:Eu phosphor aggregates under high radiation flux. *Optics and Lasers in Engineering* **2021**, *137*, 106398.
9. Leung, V. Y. F.; Lagendijk, A.; Tukker, T. W.; Mosk, A. P.; Ijzerman, W. L.; Vos, W. L., Interplay between multiple scattering, emission, and absorption of light in the phosphor of a white light-emitting diode. *Optics Express* **2014**, *22* (7), 8190-8204.
10. Ma, Y.; Sun, J.; Luo, X., Multi-wavelength phosphor model based on fluorescent radiative transfer equation considering re-absorption effect. *Journal of Luminescence* **2019**, *209*, 109-115.
11. Kumar, M.; Seshagiri, T. K.; Mohapatra, M.; Natarajan, V.; Godbole, S. V., Synthesis, characterization and studies of radiative properties on Eu³⁺-doped ZnAl₂O₄. *Journal of Luminescence* **2012**, *132* (10), 2810-2816.
12. Mohapatra, M.; Seshadri, M.; Naik, Y. P.; Meena, G.; Kadam, R. M.; Singh, V., Radiative properties of 'intense' red emitting LiAl₅O₈:Eu phosphors. *Journal of Materials Science: Materials in Electronics* **2018**, *29* (9), 7778-7784.
13. Sarner, G.; Richter, M.; Alden, M., Investigations of blue emitting phosphors for thermometry. *Measurement Science and Technology* **2008**, *19* (12), 125304-125313.
14. Coquard, R.; Baillis, D., Radiative characteristics of opaque spherical particles beds: a new method of prediction. *Journal of Thermophysics and Heat Transfer* **2004**, *18* (2), 178-186.
15. Cunsolo, S.; Coquard, R.; Baillis, D.; Chiu, W. K. S.; Bianco, N., Radiative properties of irregular open cell solid foams. *International Journal of Thermal Sciences* **2017**, *117*, 77-89.
16. Zeghondy, B.; Iacona, E.; Taine, J., Determination of the anisotropic radiative properties of a porous material by radiative distribution function identification (RDFI). *International Journal of Heat and Mass Transfer* **2006**, *49* (17-18), 2810-2819.

17. Lopes , R.; Moura , L. M.; Baillis, D.; Sacadura , J. F., Directional Spectral Emittance of a Packed Bed: Correlation Between Theoretical Prediction and Experimental Data. *Journal of Heat Transfer* **2000**, *123* (2), 240-248.
18. Barreto, G.; Canhoto, P.; Collares-Pereira, M., Combined experimental and numerical determination of the asymmetry factor of scattering phase functions in porous volumetric solar receivers. *Solar Energy Materials and Solar Cells* **2020**, *206*, 110327.
19. Zhao, S.; Sun, X.; Que, Q.; Zhang, W., Influence of Scattering Phase Function on Estimated Thermal Properties of Al₂O₃ Ceramic Foams. *International Journal of Thermophysics* **2019**, *40* (1), 11.
20. Sacadura, J.; Baillis, D., Experimental characterization of thermal radiation properties of dispersed media. *International Journal of Thermal Sciences* **2002**, *41* (7), 699-707.
21. Liu, L.; Mishchenko, M. I., Effects of aggregation on scattering and radiative properties of soot aerosols. *Journal of Geophysical Research: Atmospheres* **2005**, *110* (D11), D11211.
22. Liu, L.; Mishchenko, M. I., Scattering and radiative properties of complex soot and soot-containing aggregate particles. *Journal of Quantitative Spectroscopy and Radiative Transfer* **2007**, *106* (1), 262-273.
23. Marti, J.; Roesle, M.; Steinfeld, A., Combined Experimental-Numerical Approach to Determine Radiation Properties of Particle Suspensions. *Journal of Heat Transfer* **2014**, *136* (9), 092701.
24. Coray, P.; Lipiński, W.; Steinfeld, A., Experimental and Numerical Determination of Thermal Radiative Properties of ZnO Particulate Media. *Journal of Heat Transfer* **2009**, *132* (1), 012701.
25. Modest, M. F., *Radiative heat transfer*. 3rd ed. ed.; Academic Press: New York, 2013.
26. Petrasch, J., A Free and Open Source Monte Carlo Ray Tracing Program for Concentrating Solar Energy Research. 2010; pp 125-132.

27. Toub Blanc, D., Henyey–Greenstein and Mie phase functions in Monte Carlo radiative transfer computations. *Applied Optics* **1996**, 35 (18), 3270-3274.
28. Marti, J.; Roesle, M.; Steinfeld, A., Experimental Determination of the Radiative Properties of Particle Suspensions for High-Temperature Solar Receiver Applications. *Heat Transfer Engineering* **2014**, 35 (3), 272-280.
29. Coray, P.; Lipiński, W.; Steinfeld, A., Spectroscopic goniometry system for determining thermal radiative properties of participating media. *Experimental Heat Transfer* **2011**, 24 (4), 300-312.
30. Moosmüller, H.; Sorensen, C. M., Small and large particle limits of single scattering albedo for homogeneous, spherical particles. *Journal of Quantitative Spectroscopy and Radiative Transfer* **2018**, 204, 250-255.
31. Singh, B.; Kaviany, M., Independent theory versus direct simulation of radiation heat transfer in packed beds. *International Journal of Heat and Mass Transfer* **1991**, 34 (11), 2869-2882.

Chapter 5

Contactless Thermal Diagnostics of Acoustically Levitated Biomass under Uniform High Flux Radiation

Statement of Authorship

Title of Paper	Contactless thermal diagnostics of acoustically levitated biomass under uniform high flux radiation
Publication Status	<input checked="" type="checkbox"/> Published <input type="checkbox"/> Accepted for Publication <input type="checkbox"/> Submitted for Publication <input type="checkbox"/> Unpublished and Unsubmitted work written in manuscript style
Publication Details	Wanxia Zhao, Zhiwei Sun, and Zeyad T. Alwahabi. (2020) Energy & Fuels, 34 (1), 530-534. DOI: 10.1021/acs.energyfuels.9b03367


Principal Author


Name of Principal Author (Candidate)	Wanxia Zhao		
Contribution to the Paper	Performed experiments, analysed results, interpreted data and wrote manuscript.		
Overall percentage (%)	75		
Certification:	This paper reports on original research I conducted during the period of my Higher Degree by Research candidature and is not subject to any obligations or contractual agreements with a third party that would constrain its inclusion in this thesis. I am the primary author of this paper.		
Signature		Date	03/07/20

Co-Author Contributions

By signing the Statement of Authorship, each author certifies that:

- the candidate's stated contribution to the publication is accurate (as detailed above);
- permission is granted for the candidate to include the publication in the thesis; and
- the sum of all co-author contributions is equal to 100% less the candidate's stated contribution.

Name of Co-Author	Zhiwei Sun		
Contribution to the Paper	Assisted in experiments, discussed experimental results and findings, and revised the manuscript.		
Signature		Date	08/07/20

Name of Co-Author	Zeyad T. Alwahabi		
Contribution to the Paper	Discussed experimental results and findings, supervised the research project, and revised the manuscript.		
Signature	 Digitally signed by Zeyad Alwahabi DN: cn=Zeyad Alwahabi, o=University of Adelaide, ou= email=zeyad.alwahabi@adelaide.edu.au, c=AU Date: 2020.07.21 21:56:48 +0930	Date	21/07/20

Contactless Thermal Diagnostics of Acoustically Levitated Biomass under Uniform High Flux Radiation

Wanxia Zhao,^{†,§} Zhiwei Sun,^{‡,§} and Zeyad T. Alwahabi^{*,†,§}

[†]School of Chemical Engineering and Advanced Materials, [‡]School of Mechanical Engineering, and [§]Centre for Energy Technology, The University of Adelaide, Adelaide, South Australia 5005, Australia

ABSTRACT: This study reports a contactless optical system developed for investigating the fast-thermal processes of biomass under high-flux radiation, particularly for understanding the synergy of renewable biomass and concentrated solar energy. A biomass tablet was successfully suspended using a home-built acoustic levitator in a well-controlled oxygen-lean atmosphere and was irradiated under uniform radiation with a high flux of approximately 1 MW/m², i.e., ~1000 suns. The biomass temperature profile was spatio and temporally recorded using an infrared thermographic camera. Several key thermal parameters of the biomass were determined, including the time-resolved heating rate and the ignition temperature. Three different thermal processes were identified from the temperature profiles. These are an initial fast-heating process, a following slow-heating process, and a final biomass ignition depending on the flux of radiation. At high flux, these three processes are merged, and only a steep linear increase in temperature was observed. The contactless apparatus provides the high-fidelity data of the heating rates of biomass and can benefit the understanding of the fast-thermal process associated with biomass under high flux concentrated solar radiation.

1. INTRODUCTION

Direct measurement of biomass temperature is urgently required for understanding the thermal processes of feedstocks to improve the efficiency of renewable biomass utilization. Biomass temperature plays a key role in the heat transfer processes related to its pyrolysis, gasification, and combustion.^{1,2} To simplify experimental conditions, single or bulk biomass particles were widely studied under well-controlled boundary conditions, e.g., fixing biomass on a sample holder.^{3–5} Such an experimental method mitigated the challenges in measurements and simplified the heat transfer and thermal processes compared with the investigation of particle flow. This method also showed advantages over others that reported for single particles, e.g., dropping or seeding a single particle into a hot gaseous environment. However, firmly positioning a biomass particle or a bulk on the holder can cause an undesired and complex heat conduction between the particle and the holder, together with potential catalytic effects, which give rise to large uncertainty. For example, Wu et al.⁶ reported the pyrolysis of biomass powders in a graphite crucible under concentrated solar radiation and found heat loss from the biomass samples to the crucible walls. Stenseng et al.⁷ also stated that the discrepancy between their experimental and modeling results could be due to the heat transfer and the thermal lag between the sample and the crucible/thermocouple, which was not considered in the model.

Therefore, a more reliable contactless method is critically required to free the particle from physical contact to avoid the influences of unnecessary heat transfer. A contactless method is also particularly required for studying the fast pyrolysis of biomass that is driven by concentrated solar radiation (CSR), in which a physical holder can also be heated to a high temperature by the solar radiation.^{8,9}

However, the contactless experimental method for studying biomass thermal processing is scarcely reported. In the limited

previous studies, electrodynamic balances had been used to suspend biomass particles by creating a dynamic electric field, but with the limited capability of levitating small particles, typically less than 300 μm .^{10–12} Moreover, an electrical field can potentially influence chemical reactions in which charge transfer is involved. Acoustic levitators are widely used for single particle and droplet suspensions.^{13,14} Compared to an electrodynamic balance, an acoustic levitator is relatively simple to fabricate and can be combined easily with an external heating source. However, the application of acoustic levitators for biomass suspension and thermal process investigation has not been reported.

Choosing a suitable heating source is equally important in studying the thermal processes of biomass. A high-flux radiation source with a well-characterized flux profile was generally used, e.g., high-power lamps, CO₂ laser at 10.6 μm , and Nd:YAG laser.^{15–17} Because of the high flux, typically at the order of MW/m² (~1000 suns), these powerful light sources are particularly beneficial in studying the fast pyrolysis of biomass under CSR. The synergy of biomass with CSR can not only reduce CO₂ emissions but also simplify the gas purification processes.^{18,19} However, these light sources also have a few limitations, e.g., long running-up time for lamps, spectral difference for CO₂ laser, and relatively low flux of Nd:YAG laser. Therefore, a more suitable powerful radiation source is still sought for studying the fast pyrolysis of biomass. In this study, a uniform and high-flux radiation, which was operated at 910 nm and delivered via an optical fiber probe, was used to heat the biomass.

Received: October 1, 2019

Revised: December 10, 2019

Published: December 17, 2019



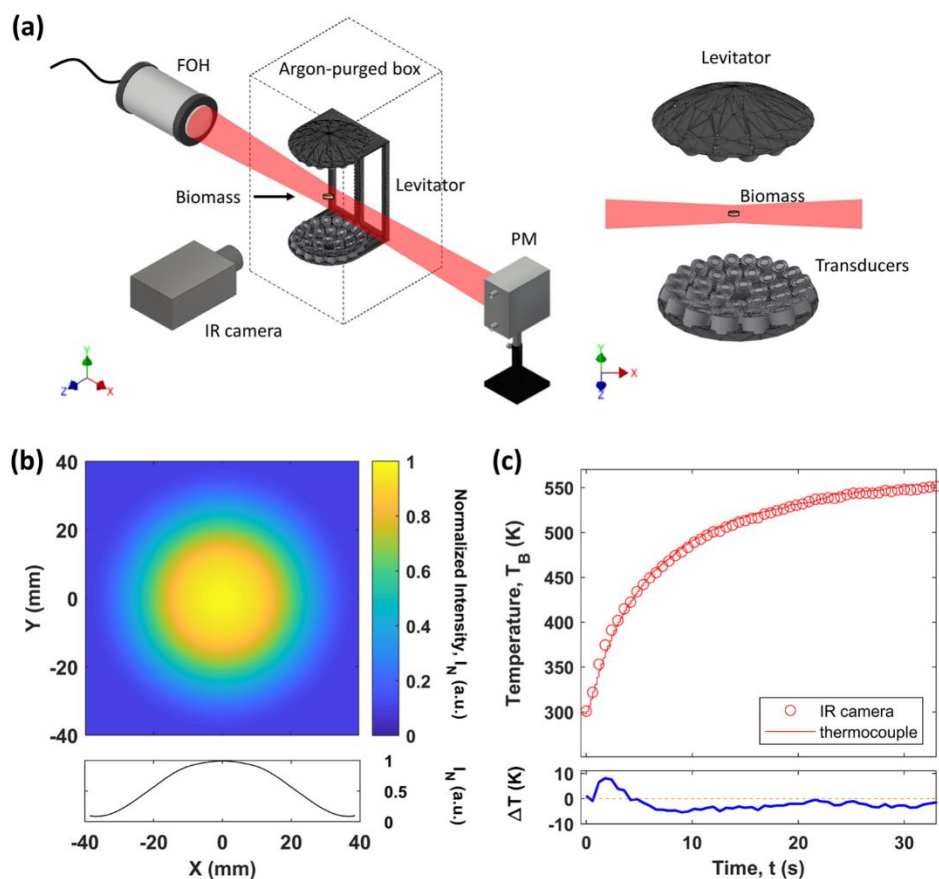


Figure 1. (a) Left: schematic diagram of the experimental setup. FOH: fiber-optic head of a concentrated solar simulator. PM: power meter. Right: The acoustic levitator with a suspended biomass tablet. (b) Normalized spatial intensity, I_N , profile of the radiation field at the measurement volume. The line presents the cross-section of the radiation field. (c) Biomass temperature, T_B , measured using an infrared and a thin thermocouple, together with the difference between the two measurements, ΔT .

We demonstrated an innovative contactless apparatus that was specifically developed for studying biomass thermal processes under high-flux radiation, together with a contactless method for biomass temperature imaging. Using this apparatus, biomass samples were levitated by acoustic force to avoid potential and complicated heat conduction between the sample and the contact system. Representative results are shown and discussed in this work with highlighting the temporally resolved biomass temperature and the heating rates under different high fluxes.

2. EXPERIMENTAL SECTION

Figure 1a shows the scheme of the contactless experimental setup, which consists of an acoustic levitator for particle suspension, the laser-based high-flux light source for biomass heating, and an infrared thermometry camera for temperature imaging. The radiation system is a collimated light source based on 41 near-infrared diode lasers centered at 910 nm with the typical full width at half-maximum (fwhm) of 3.3 nm and can provide a total power of 3.2 kW.²⁰ The radiation output can be flexibly delivered using a multifiber bundle onto the measurement volume, being notably able to provide a maximum flux of ~ 30 MW/m² within an area of 10 mm in diameter. A water-cooled power meter was placed along with the beam propagation direction after the levitator to record the radiation flux during the measurement. The acoustic levitator, originally designed by Marzo et al.,²¹ was home-assembled and used to levitate a biomass tablet. A total of 36 transducers were arranged at each top and the bottom plate of the levitator, respectively. All transducers were

operated at a frequency of 40 kHz and a DC voltage of 12 V to provide trapping forces to levitate a biomass tablet stably (but spinning, as discussed below) at several specific heights along the levitator axis. It was found that this levitator can levitate a biomass tablet of 3 mm in diameter with a density of around 1.5 g/cm³. The total power of the levitator is 7.2 W, significantly lower than that of radiation, and no temperature change was found on the levitated biomass tablet without radiation.

Figure 1b presents the radiation profile recorded at the focus plane, showing a wide and uniform region of ~ 20 mm where the first 20% of the peak flux locates. This light source, working as a solar simulator, has a run-up time of 15 ms and can rapidly provide constant flux to the biomass sample. The flux of radiation can be precisely and easily adjusted via the operating current of the diode lasers.

To avoid the fast combustion of biomass, the levitator was placed in an argon-purged box with a low gas flow rate, resulting in an oxygen-lean ($\sim 16\%$) environment. The argon-purged box is made of transparent plastic, and three round holes are opened for the heating beam and IR signals to avoid any obstacle along the optical path. Rice straw and almond husk biomass tablets were studied with similar chemical compositions. The rice straw contains 39.70% carbon, 5.71% hydrogen, 53.15% oxygen, 1.04% nitrogen, and $<0.40\%$ sulfur; while the corresponding elements are 42.49%, 5.88%, 50.01%, 1.22%, and $<0.40\%$ for the almond husk. Rice straw was first pulverized and sieved to fine particles ranging from 98 to 125 μm in size, while almond husk powder was approximately 500 μm . The biomass powders were then pelletized to form small tablets with a diameter of 3 mm and a thickness of 0.6 mm as shown in Figure 2. The area of uniform radiation is sufficiently broad to allow the small tablets to stay

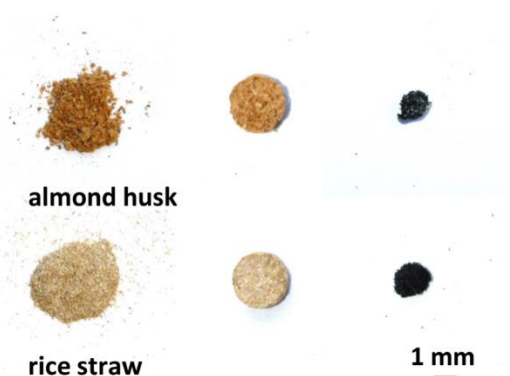


Figure 2. Biomass samples of almond husk (top) and rice straw (bottom). Left, raw powders; middle, compressed tablets for measurements; right, tablets after measurements.

under constant flux, as shown in Figure 1b. The biomass tablet was spinning along its central axis at a rate of approximately 7 rounds per second, corresponding to a velocity of ~ 0.07 m/s on the edge of the tablet. The spinning of the tablet mitigates the issue that only one side of the tablet can be irradiated. After pyrolysis or combustion processes, the biomass tablets were carbonized as char.

The biomass temperature was nonintrusively measured using an infrared thermographic camera (Jenoptik, VarioCAM HD) with a frame rate of 50 Hz, corresponding to a temporal resolution of 20 ms and a spatial resolution 0.5 mm per pixel. The spectral range of the infrared camera is from 7.5 to 14 μm . No interference of the heating laser radiation to the thermometry camera is observed. The biomass emissivity, one of the camera parameters, was set as 0.95.

To validate the accuracy of the infrared temperature measurement, a rice straw tablet was hung using a thin-wire thermocouple (~ 75 μm) and heated using the radiation source. The junction point of the thermocouple was attached inside of the biomass tablet, without any direct contact with the heating radiation, to eliminate the influence of incident radiation on thermocouple temperature measurement. Figure 1c shows a good agreement between the biomass temperatures measured using the camera and the thermocouple, confirming the high accuracy of temperature measurement using the camera, which is typically within ± 5 K, except at the early fast-rising stage with a difference of +8 K.

3. RESULTS AND DISCUSSION

Figure 3 shows representative images of an almond husk tablet under a radiation flux of 0.96 MW/m^2 , including two thermographic images and the corresponding direct visualizations simultaneously recorded using a digital camera. At 2.20 s after the radiation was turned on, the tablet temperature was around 410 K and no combustion phenomenon was observed from the corresponding visual image. At $t = 3.22$ s, a significantly higher temperature of 520 K was observed at the right-end side of the tablet, which is the light-incident side. Ignition phenomena were also clearly seen in the corresponding visual image. Figure 3a also shows a nonuniform profile of temperature along the light propagation direction. In data processing, the mean value of the five highest temperatures, which were read from five different pixels, was adopted as the evaluated temperature of the tablet.

Figure 4 presents the time-resolved temperatures measured for two tablets under different radiation fluxes. The flux value of radiation significantly influences the temperature profile of the tablets and the consequent combustion process. At low radiation flux, the biomass temperature only has a steep increase within the first second. Then the temperature

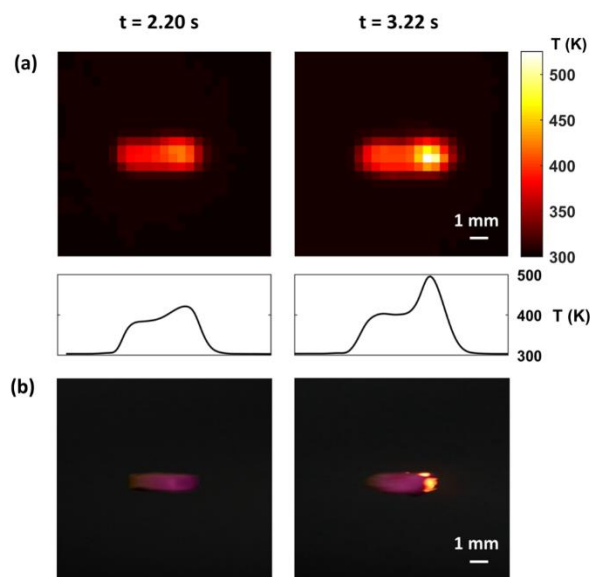


Figure 3. (a) Representative infrared thermographic images of an almond husk biomass tablet heated with high-flux radiation of 0.96 MW/m^2 and (b) direct visual images simultaneously recorded with a digital photographic camera. The black lines in (a) present the cross-section of particle temperature.

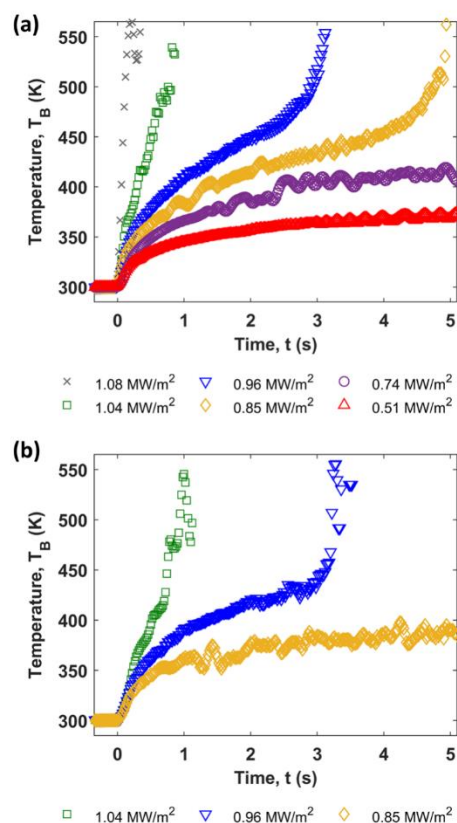


Figure 4. Temporal profiles of the temperature measured for (a) a rice straw and (b) an almond husk tablet under different radiation heat fluxes.

increases with a very slow rate without any significant change. Correspondingly, no ignition or combustion phenomenon was

observed in the visual images. At high radiation flux, not only a higher heating rate but also the ignition of biomass was observed. A second steep increase in tablet temperature appears as a result of the ignition, starting at $t = 3$ s under the 0.96 MW/m^2 radiation for the rich straw tablet. As the flux of radiation further increased, the tablets were quickly heated up and then ignited within a short time, showing fast linearly increasing profiles of the temperature, in which the three processes are hard to identify. It is also found that the rice straw tablets are ignited at around 450 K, which is slightly higher than that of the almond husk tablets, around 430 K. However, this does not mean that the almond husk tablets need a lower flux to ignite than rich straw. For example, the rice tablets can be ignited at the flux of 0.85 MW/m^2 , but almond husk cannot, as shown in Figure 4.

Figure 5a presents a direct comparison between the temporal profiles of temperature measured for two different

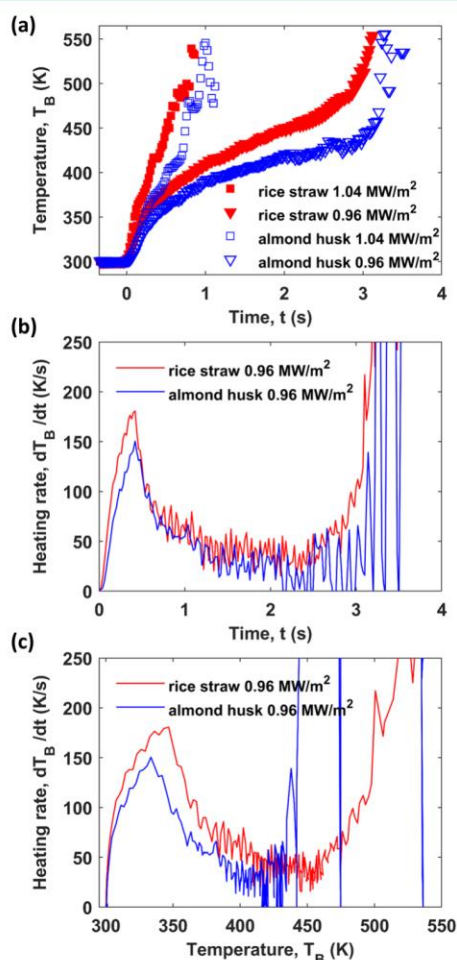


Figure 5. (a) Temperature of an almond husk and a rice straw tablet under two different radiation fluxes. The heating rates as a function of (b) time and (c) biomass temperature.

biomass tablets under the radiation fluxes of 0.96 MW/m^2 and 1.04 MW/m^2 . The times at which combustion starts are similar for the two tablets at 0.96 MW/m^2 , but the temporal profiles of the temperature are clearly different from each other, indicating different heating rates for these two kinds of biomasses. The heating rate, quantified as dT/dt , is very

sensitive to the magnitude of the radiation flux. As shown in Figure 5a, a slight increase in the flux from 0.96 to 1.04 MW/m^2 (i.e., an 8% increase) can significantly change the rising profiles of the temperatures and greatly shortens the ignition time from 3 to 1 s. Figure 5b,c presents the results of the heating rate as a function of the heating time and the biomass temperature, respectively. On the time scale, three regimes of the heating rate are clearly identified, i.e., the fast-heating process within 1 s, the slow-heating process from $t = 1$ to 3 s, and the combustion process starting at $t = 3$ s. While the heating rate of the almond husk is lower than that of rice straw, the two biomasses have consistent temporal profiles of the heating rate as shown in Figure 5b, confirming the similar ignition times. As a function of temperature, however, the profiles of the heating rate are significantly different for these two biomasses, as shown in Figure 5c, clearly indicating the different ignition temperatures. These temporal-resolved and temperature-resolved heating rates would be highly valuable for both understanding the thermal processes of biomass and developing reliable numerical models.

4. CONCLUSIONS

An innovative contactless apparatus, designed for understanding the fast-thermal processes of a single biomass particle under high-flux radiation, has been demonstrated. The temporal profiles of particle temperature were accurately measured using a thermographic camera with a high spatiotemporal resolution. The heating rate was evaluated from the temporal profile of the temperature measured, from which different thermal processes were reliably identified. The apparatus can be applied to other small tablets, e.g., solid wastes and liquid droplets, and has the potential to be combined with other measurement methods, e.g., a gas analyzer for biomass.

AUTHOR INFORMATION

Corresponding Author

*(Z.T.A.) E-mail: zeyad.alwahabi@adelaide.edu.au.

ORCID

Wanxia Zhao: 0000-0001-5916-9669

Zhiwei Sun: 0000-0001-7899-9676

Zeyad T. Alwahabi: 0000-0003-4831-7798

Notes

The authors declare no competing financial interest.

ACKNOWLEDGMENTS

Support was received from Australian Research Council (ARC) through the Discovery Project DP180102045 with Grant Number LE130100127.

REFERENCES

- (1) Sharma, A.; Pareek, V.; Zhang, D. Biomass pyrolysis—A review of modelling, process parameters and catalytic studies. *Renewable Sustainable Energy Rev.* **2015**, *50*, 1081–1096.
- (2) Zeng, K.; Minh, D. P.; Gauthier, D.; Weiss-Hortala, E.; Nzihou, A.; Flamant, G. The effect of temperature and heating rate on char properties obtained from solar pyrolysis of beech wood. *Bioresour. Technol.* **2015**, *182*, 114–119.
- (3) Al-Rahbi, A. S.; Onwudili, J. A.; Williams, P. T. Thermal decomposition and gasification of biomass pyrolysis gases using a hot bed of waste derived pyrolysis char. *Bioresour. Technol.* **2016**, *204*, 71–79.

- (4) Park, W. C.; Atreya, A.; Baum, H. R. Experimental and theoretical investigation of heat and mass transfer processes during wood pyrolysis. *Combust. Flame* **2010**, *157* (3), 481–494.
- (5) Yip, K.; Tian, F.; Hayashi, J. I.; Wu, H. Effect of alkali and alkaline earth metallic species on biochar reactivity and syngas compositions during steam gasification. *Energy Fuels* **2010**, *24* (1), 173–181.
- (6) Wu, H.; Gauthier, D.; Yu, Y.; Gao, X.; Flamant, G. Solar-thermal pyrolysis of mallee wood at high temperatures. *Energy Fuels* **2018**, *32* (4), 4350–4356.
- (7) Stenseng, M.; Jensen, A.; Dam-Johansen, K. Investigation of biomass pyrolysis by thermogravimetric analysis and differential scanning calorimetry. *J. Anal. Appl. Pyrolysis* **2001**, *58*, 765–780.
- (8) Bashir, M.; Yu, X.; Hassan, M.; Makkawi, Y. Modeling and performance analysis of biomass fast pyrolysis in a solar-thermal reactor. *ACS Sustainable Chem. Eng.* **2017**, *5* (5), 3795–3807.
- (9) Zeng, K.; Soria, J.; Gauthier, D.; Mazza, G.; Flamant, G. Modeling of beech wood pellet pyrolysis under concentrated solar radiation. *Renewable Energy* **2016**, *99*, 721–729.
- (10) Biagini, E.; Pintus, S.; Tognotti, L. Characterization of high heating-rate chars from alternative fuels using an electrodynamic balance. *Proc. Combust. Inst.* **2005**, *30* (2), 2205–2212.
- (11) Chan, M. N.; Choi, M. Y.; Ng, N. L.; Chan, C. K. Hygroscopicity of water-soluble organic compounds in atmospheric aerosols: amino acids and biomass burning derived organic species. *Environ. Sci. Technol.* **2005**, *39* (6), 1555–1562.
- (12) Tognotti, L.; Longwell, J. P.; Sarofim, A. F. The products of the high temperature oxidation of a single char particle in an electrodynamic balance. *Symp. (Int.) Combust., [Proc.]* **1991**, *23* (1), 1207–1213.
- (13) Andrade, M. A.; Bernassau, A. L.; Adamowski, J. C. Acoustic levitation of a large solid sphere. *Appl. Phys. Lett.* **2016**, *109* (4), 044101.
- (14) Contreras, V.; Valencia, R.; Peralta, J.; Sobral, H.; Meneses-Nava, M. A.; Martinez, H. Chemical elemental analysis of single acoustic-levitated water droplets by laser-induced breakdown spectroscopy. *Opt. Lett.* **2018**, *43* (10), 2260–2263.
- (15) Carlsson, P.; Lycksam, H.; Gren, P.; Gebart, R.; Wiinikka, H.; Iisa, K. High-speed imaging of biomass particles heated with a laser. *J. Anal. Appl. Pyrolysis* **2013**, *103*, 278–286.
- (16) Christodoulou, M.; Mauviel, G.; Lédé, J.; Beaurain, P.; Weber, M.; Legall, H.; Billaud, F. Novel vertical image furnace for fast pyrolysis studies. *J. Anal. Appl. Pyrolysis* **2013**, *103*, 255–260.
- (17) Kwon, G.-J.; Kuga, S.; Hori, K.; Yatagai, M.; Ando, K.; Hattori, N. Saccharification of cellulose by dry pyrolysis. *J. Wood Sci.* **2006**, *52* (5), 461–465.
- (18) Morales, S.; Miranda, R.; Bustos, D.; Cazares, T.; Tran, H. Solar biomass pyrolysis for the production of bio-fuels and chemical commodities. *J. Anal. Appl. Pyrolysis* **2014**, *109*, 65–78.
- (19) Nzihou, A.; Flamant, G.; Stanmore, B. Synthetic fuels from biomass using concentrated solar energy – A review. *Energy* **2012**, *42* (1), 121–131.
- (20) Alwahabi, Z. T.; Kueh, K. C.; Nathan, G. J.; Cannon, S. Novel solid-state solar thermal simulator supplying 30,000 suns by a fibre optical probe. *Opt. Express* **2016**, *24* (22), A1444–A1453.
- (21) Marzo, A.; Barnes, A.; Drinkwater, B. W. TinyLev: A multi-emitter single-axis acoustic levitator. *Rev. Sci. Instrum.* **2017**, *88* (8), 085105.

Chapter 6

Development and Characterization of a Grape Marc Hydrochar Slurry Fuel

Statement of Authorship

Title of Paper	Development and characterization of a grape marc hydrochar slurry fuel		
Publication Status	<input checked="" type="checkbox"/> Published	<input type="checkbox"/> Accepted for Publication	
	<input type="checkbox"/> Submitted for Publication	<input type="checkbox"/> Unpublished and Unsubmitted work written in manuscript style	
Publication Details	Wanxia Zhao, Jenny Howie, Zhiwei Sun, Philip Kwong, Zeyad T. Alwahabi. (2020) Energy & Fuels, 34 (11), 14215–14222. DOI: 10.1021/acs.energyfuels.0c02567		

Principal Author

Name of Principal Author (Candidate)	Wanxia Zhao		
Contribution to the Paper	Performed experiments, analysed results, interpreted data and wrote manuscript.		
Overall percentage (%)	70		
Certification:	This paper reports on original research I conducted during the period of my Higher Degree by Research candidature and is not subject to any obligations or contractual agreements with a third party that would constrain its inclusion in this thesis. I am the primary author of this paper.		
Signature		Date	03/07/20

Co-Author Contributions

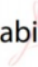
By signing the Statement of Authorship, each author certifies that:

- i. the candidate's stated contribution to the publication is accurate (as detailed above);
- ii. permission is granted for the candidate to include the publication in the thesis; and
- iii. the sum of all co-author contributions is equal to 100% less the candidate's stated contribution.

Name of Co-Author	Jenny Howie		
Contribution to the Paper	Assisted in experiments, analysed results, and interpreted data.		
Signature		Date	07/07/20

Name of Co-Author	Zhiwei Sun		
Contribution to the Paper	Assisted in experiments.		
Signature		Date	08/07/20

Name of Co-Author	Philip Kwong		
Contribution to the Paper	Discussed experimental results and findings, supervised the research project, and revised the manuscript.		
Signature		Date	20/07/20

Name of Co-Author	Zeyad T. Alwahabi		
Contribution to the Paper	Discussed experimental results and findings, supervised the research project, and revised the manuscript.		
Signature	 Zeyad Alwahabi <small>Digitally signed by Zeyad Alwahabi DN: cn=Zeyad Alwahabi, o=University of Adelaide, ou, email=zeyad.alwahabi@adelaide.edu.au, c=AU Date: 2020.07.21 21:56:48 +0930'</small>	Date	21/07/20


Development and Characterization of a Grape Marc Hydrochar Slurry Fuel

Wanxia Zhao, Jennifer Mary Howie, Zhiwei Sun, Chi Wai Kwong,* and Zeyad T. Alwahabi*

 Cite This: *Energy Fuels* 2020, 34, 14215–14222

 Read Online

ACCESS |

 Metrics & More

 Article Recommendations

ABSTRACT: The development and characterization of a grape marc hydrochar slurry fuel are reported. The slurry fuel was prepared by mixing finely milled solid hydrochar, derived from the hydrothermal carbonization of grape marc, with water and dispersants. The rheological properties of the hydrochar slurry were measured using a cone and plate rheometer. The characterization of the radiatively heated hydrochar slurry was investigated by suspending a single fuel droplet in space using an acoustic levitator and irradiating it under radiation fluxes of 1.92 and 0.74 MW/m². The higher heating value of solid hydrochar was found to be 26.0 MJ/kg, while 40 and 50 wt % hydrochar slurries had values of 10.4 and 13.0 MJ/kg, respectively. The flow behavior indexes of all slurry samples were less than unity. The temperature profiles of the suspended slurry droplets were temporally recorded. The maximum surface heating rate of the 50 wt % slurry droplet under radiation heating within the first 0.2 s was above 400 K/s. The maximum surface ignition time of suspended and irradiated hydrochar slurry droplets was measured at 0.37 ± 0.01 s, while the surface ignition temperature ($T_{\text{ig}}^{\text{surf}}$) was 375 ± 15 K, independent of heat flux. Employing the high-flux radiation system can efficiently heat the samples, and it is practical to simulate the heating behaviors of fuels in a real combustion environment. The attractive relatively low $T_{\text{ig}}^{\text{surf}}$ highlights the newly developed hydrochar slurry having great potential application as a liquid biofuel.

1. INTRODUCTION

A bioslurry fuel is similar to coal slurry and represents an alternative liquid biofuel product derived from sustainable biomass resources. Comparing with traditional solid fuels, it has the advantages of low operating cost, high energy density, ease of storage, and suitability for a wide range of applications such as boilers, gasifiers, and combustion engines.¹ Hydrothermal carbonization (HTC) is one method that can produce high energy density char products, which is the primary step for yielding bioslurry fuels. HTC is a thermal pretreatment technology, involving the decomposition of biomass in the presence of pressurized water, to convert the raw feedstock into a coal-like solid hydrochar product which has been successfully used as solid fuels.^{2,3} Typical operating temperature and pressure are maintained within the 453–523 K and 10–80 bar ranges depending on the reactor's temperature.⁴ Compared with other methods of char production, HTC requires significantly less energy and is well suited to a wider range of biomass, especially for moist feedstocks. By eliminating the extensive predrying treatment, which is necessary in other processes such as pyrolysis, HTC presents a feasible solution to process wet biomass feedstocks, such as grape marc, food waste, and bagasse.⁵

Bioslurry fuels, produced from biochar via biomass pyrolysis, have good fuel properties.^{6–8} Abdullah et al.⁶ produced the biochar slurry fuels from fast pyrolysis of mallee biomass and investigated their rheological properties. The biochar slurry produced exhibited non-Newtonian pseudo-plastic behavior showing the desired characteristics of liquid fuels. Liu et al.⁷ seeded algae with biochar particles to produce a new slurry fuel for combustion in diesel engines. The biochar was prepared by

the pyrolysis of pine sawdust. With appropriate biochar ratios, their slurry fuel presented good ignition and combustion qualities. However, the high ash content of biochar may cause fouling, corrosion, and slagging during slurry combustion.^{9,10} This limitation can be overcome when using the HTC-produced hydrochar. During hydrothermal treatment, it emerged that significant amounts of inorganics can be dissolved in water and removed from the formed char product.¹¹ Consequently, the hydrochar presents a considerable reduction in ash content when compared with pyrolyzed biochar, and its utilization can reduce ash-related issues during combustion.^{2,12}

Regarding the application of hydrochar, recent studies focused mainly on the direct combustion of solid products.^{12–15} Liu et al.¹² investigated the co-combustion behaviors of lignite and hydrochar which were produced from coconut fibers and eucalyptus leaves. These authors reported that fuel quality could be improved by using hydrochar because of its high energy density and low ash content. Tremel et al.¹⁵ undertook gasification studies on hydrochar derived from beech wood and found that pulverized hydrochar particles could promote fluidization during combustion. However, research on the application of hydrochar in the form of a

Received: July 31, 2020

Revised: October 20, 2020

Published: November 5, 2020



slurry is scarcely reported, and none of its fuel properties has been investigated for the potential application in boilers, gasifiers, or diesel engines.

The desired slurry fuels for energy applications should have high energy densities and good rheological properties.¹⁶ The rheological behavior is especially important to determine whether the bioslurry can be used as a liquid fuel. For applications of slurry fuels in existing technologies, the preferred liquid fuel requires non-Newtonian and pseudo-plastic flow behaviors.^{6,16,17} Desirable rheological properties include apparent viscosity of less than 700 mPa·s for gasifier use and below 1000 mPa·s for boiler use at a shear rate of 100 s⁻¹.⁶ For application in diesel engines, the apparent viscosity must be less than 300 mPa·s at a shear rate of 1000 s⁻¹.⁷

To characterize the slurry fuel under radiation heating conditions, selecting a suitable heat source is important. Traditional methods are based on the use of furnaces equipped with thermogravimetric analysis (TGA) systems.^{13,14} The heating rate with the TGA method was often limited by the heating element of the apparatus. TGA can be used to heat samples under non-isothermal conditions at a heating rate of around only 10–20 K/min,^{13,18} which makes it difficult to simulate the heating behavior of fuels in the real combustion environment. Here, the fuel particles can be immediately heated up to a reactor temperature of around 1000 K.¹⁹

Previous studies associated with fuel heating usually relied on the approach that a slurry/liquid droplet was suspended on the tip of a thin holder or fiber.^{20,21} However, the utilization of physical holders may induce unnecessary and complex heat transfer issues between the droplet and the holder and subsequently affect heating progresses. Therefore, a more reliable contactless levitation system has already been developed to minimize these issues and is used for both particles and droplets of biofuels.^{22–24} In this work, an acoustic levitator was used to suspend the hydrochar slurry droplets without physical contact. The hydrochar slurry droplets were then irradiated with well-controlled and homogeneous radiation.

Grape marc is one of the richest agriculture residuals, and it is available worldwide in abundance at a low cost. It is also a promising feedstock for renewable energy production because of its large amount of lignocellulosic compounds. However, technologies to exploit the advantages of grape marc have not been widely adopted. Currently, 50% of grape marc is disposed of in an open waste environment, which results in emissions to the surrounding area.²⁵

This study aims to: first, produce a homogenous hydrochar slurry that was prepared from grape marc using HTC technology and second, determine its key rheological properties and characterize its droplets under high-flux radiation heating. The influences of solid loading, particle size, and dispersant type on the rheological properties of the hydrochar slurry were investigated. A high-flux radiation heating source and an acoustic levitation system, which was previously used for research into biomass thermal processing,²³ served to study the fuel temperatures, fuel heating rates, surface ignition time, and surface ignition temperature ($T_{\text{ig}}^{\text{surf}}$) of a radiatively heated slurry droplet without any physical contact. The results from this study will guide the development of a hydrochar slurry derived from the HTC of grape marc for potential liquid fuel applications.

2. EXPERIMENTAL SECTION

2.1. Production of Hydrochar. The biomass sample selected for conversion to hydrochar was grape marc provided by Tarac Technologies, which is based in South Australia. The as-received grape marc at 50% moisture content was oven-dried to approximately 5 wt % moisture for storage. Before the HTC experiments, the dried grape marc samples with a particle size at around 1–2 mm were premixed with distilled water at a 50:50 volumetric ratio. The mixture was loaded into the laboratory-scale HTC reactor to produce hydrochar samples. This reactor's design and operation have been described in detail elsewhere.⁵ Briefly, the loaded HTC reactor was purged with nitrogen and heated to 513 K and maintained for 60 min. The pressure of the reactor was maintained above 21 bar during the HTC process to ensure water remained in a liquid state. The solid yield of the HTC process was at around 70%. After the reaction, the reactor was cooled down and the reactor pressure was then slowly released before products were emptied for filtration. The products were separated into liquid and solid by filtration. The hydrochar solid cakes that formed on the filter paper were air-dried at 378 K for >8 h to reduce the moisture level to <1%.

2.2. Preparation of the Hydrochar Slurry. The obtained dried hydrochar solids were ground using a high-energy mill (Fritsch, Pulverisette 7). Two stainless steel mill containers were run simultaneously, while each mill was loaded with around 4.2 g of hydrochar with 3 mm zirconia balls. Two different grinding times, 30 and 120 min, at a grinding speed of 350 rpm were selected to study the impact on particle size distribution. The milled hydrochar powder was sprayed with 5 mL of water to disperse the electrostatic charge and sieved with a 20 μm mesh. The particle size distributions were measured using a Mastersizer (Malvern, 2000).

Three dispersants, namely, sodium naphthalene sulphonate formaldehyde (NSF) (Weifang Beacon Chemical Building Materials Co. Ltd., China), sodium lignosulphonate (SL) (Dust-a-Side Australia, Australia), and 42% poly butadiene-maleic acid (PBMA) (Polysciences, Inc., United States) were chosen to produce the hydrochar slurry samples. The dispersant was mixed with premixed hydrochar powder and distilled water at 40 and 50 wt % solid loadings. The overall concentration of the dispersant in the final slurry samples was maintained at around 1 wt %. Then, the mixture was dispersed in an ultrasonic bath for 1 min to produce the final hydrochar slurry samples for experiments.

2.3. Hydrochar Properties. The elemental analysis of the hydrochar was carried out using a CHNS elemental analyzer (PerkinElmer, 2400 Series II CHNS/O). The analysis for C, H, N, S, and O was carried out following ASTM D5373, with the oxygen content being calculated by the difference. The higher heating value (HHV) was derived from the results for the elemental analysis using the Boie equation.²⁶ The shear stress and apparent viscosity were measured using a universal stress rheometer (Rheometric Scientific, SRS) using the cone and plate geometry. A sample volume of 1 mL was used for each measurement. The shear rate was varied to a maximum of 1000 s⁻¹ to determine its effect on apparent viscosity and shear stress. The measurement temperature was maintained at 298 K. The relationship between the variation of shear rate (up to 1000 s⁻¹) and shear stress was fitted with the power-law model, which can be expressed as

$$\tau = K\dot{\gamma}^n \quad (1)$$

where τ is the shear stress, $\dot{\gamma}$ is the shear rate, K is the rheological constant, and n is the flow behavior index. For $n = 1$, the equation reduces to the law for Newtonian viscosity and the flow is Newtonian. For $n > 1$, the flow is dilatant and for $n < 1$ flow is pseudo-plastic, which is desired for slurry fuel used in boiler, gasifier, and diesel engine application.⁶

2.4. Radiation Heating and Diagnostics. Figure 1 shows the schematic diagram of the experimental setup to investigate the radiatively heated hydrochar slurry droplets. The setup consists of an acoustic levitator for droplet suspending, a laser-based high-flux light source for intensive heating, a digital camera (Nikon, D5500) for

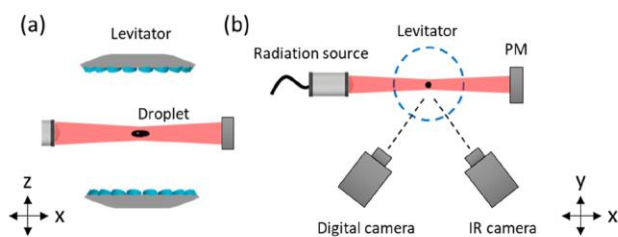


Figure 1. (a) Side-view and (b) top-view schematic diagram of the experiment setup. The red line indicates the beam path of the heating radiation. PM indicates the power meter.

visual imaging, and an infrared (IR) thermometry camera (Jenoptik, VarioCAM HD) for temperature measurement. High-flux heating radiation was provided by a collimated radiation source.²⁷ The light source was based on 41 near-IR diode lasers, whose wavelength is centered at 910 nm with a typical full width at half-maximum of 3.3 nm. The radiation is flexibly delivered through a multifiber bundle and able to provide a high heat flux (\sim MW/m²) in a small area with a diameter of 10 mm. Furthermore, the radiation source has a run-up time of 15 ms and can quickly provide constant flux to the slurry droplet.

An acoustic levitator originally designed by Marzo et al.²⁸ was used to levitate the hydrochar slurry droplet. A total of 72 transducers were arranged at the top and bottom surfaces of the 3D printed levitator frame in a hexagonal pattern and operated at 40 kHz. They transformed the electrical input signal into acoustic waves and generated enough trapping force to levitate droplets. The higher voltage of the excitation signal was required to levitate the denser droplet. However, the high trapping force resulting from the high voltage could cause the breakup of the levitated droplet. Thus, in this present study, with the objective of providing stable and continuous trapping force for a long period, the power voltage was maintained at 9 V. Doing so ensured stable levitation of a small droplet with a density up to 3.5 g/mL. The slurry droplet was introduced into the acoustic pressure field using a microliter pipette, and the droplet volume was around 10 μ L. The droplet was suspended and spanned along the center axes of the levitator with a rotational frequency of 7 rounds/s. By using this acoustic levitation system, the heat transfer to the levitated droplet was only caused by the presence of heating radiation and ambient air.

Time-resolved temperature and visual imaging of the suspended and irradiated slurry droplet were measured using an IR thermographic camera and a digital camera with a macro lens (Tamron, F017), respectively. The frame rate of the thermographic camera and the digital camera is 20 ms. The focal length of the visual camera is 90 mm. The emissivity of black slurry droplets was assumed to be 0.98 according to a previous work²³ and the appearance of droplet samples. The accuracy of temperature measurement using the IR camera has been assessed,²³ which is typically within \pm 5 K in the temperature range of 300–800 K. The droplet's temperatures and the visual behavior were continuously recorded. The surface temperature (T^{surf}) of the slurry droplet was evaluated from the average value of five pixels, which had the highest temperatures. The change in the visual images reveals the surface ignition time. The surface ignition time was defined as the recording time of the image where the first ignition occurring on the droplet surface was observed.

3. RESULTS AND DISCUSSION

3.1. Particle Size Distribution of Hydrochar. Figure 2 illustrates the particle size distributions of the dried hydrochar particles processed with different grinding times. The particle size distribution approaches a log-normal distribution with a mean diameter of 11.5 μ m for 30 min grinding time and 8.1 μ m for 120 min grinding time. Even though the increase in grinding time leads to a decrease in particle size, the extended grinding time only elicited a limited impact on further

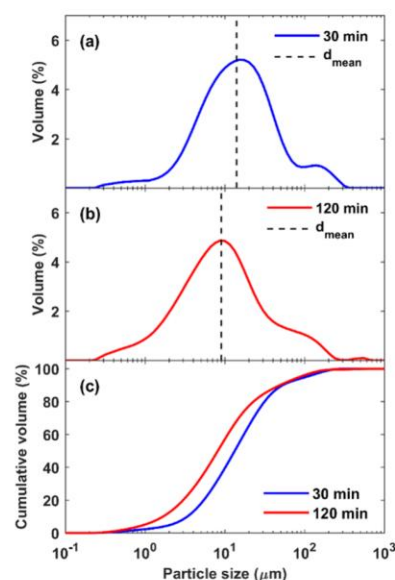


Figure 2. Particle size distributions of hydrochar particles at (a) 30 min and (b) 120 min of grinding time, and (c) their respective cumulative size distribution volumes.

reduction in particle size distribution. Only around 3 μ m in mean particle size reduction was observed with an additional 90 min grinding time. Therefore, 30 min grinding time would be considered sufficient for slurry fuel production with the desired particle size between 10 and 15 μ m.

3.2. Heating Value of the Hydrochar and Hydrochar Slurry.

Table 1 presents the ultimate analysis of hydrochar

Table 1. Ultimate Analysis and HHV of Hydrochar

ultimate analysis (wt %)	
C	64.3
H	5.8
N	2.4
O (by difference)	27.6
HHV (MJ/kg)	
hydrochar	26.0
hydrochar slurry with 50 wt % solid loading	13.0
hydrochar slurry with 40 wt % solid loading	10.4

that was produced at a HTC reaction temperature of 513 K. Based on the elemental composition of the hydrochar, the HHV of the hydrochar was found to be 26.0 MJ/kg, which is comparable to the HHV of sub-bituminous coal at 17–25 MJ/kg.²⁹ This indicates that the heating value of hydrochar is desirable for fuel applications. With 50 and 40 wt % hydrochar slurries, the HHVs were found to be 13.0 and 10.4 MJ/kg, respectively.

3.3. Rheological Properties of the Hydrochar Slurry.

Figure 3 shows the rheological behavior at 298 K of the hydrochar slurry samples with two solid loadings (40 and 50 wt %) and three different dispersants (SL, NSF, and PBMA). It should be noted that the slurry sample did not behave as a liquid when the solid loading was higher than 50 wt % even when dispersants were being used. Therefore, the maximum achievable solid loading of the slurry samples was 50 wt %. From Figure 3, it was discovered that the apparent viscosity was increased with higher solid loading. The apparent

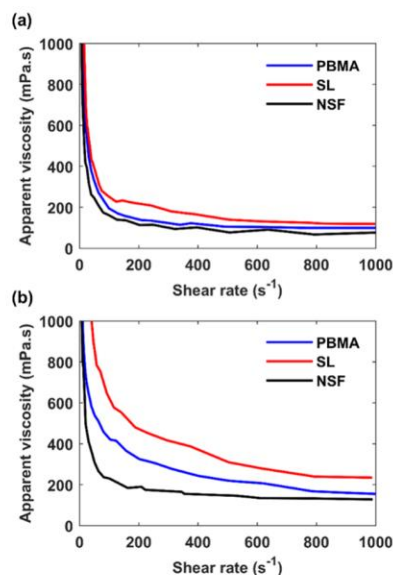


Figure 3. Effect of three dispersants, i.e. SL, NSF, and PBMA, at 1 wt % loading on the apparent viscosity of hydrochar–water slurry fuels with increasing shear rate at (a) 40 wt % solid loading and (b) 50 wt % solid loading.

viscosities of the slurry samples for 40 wt % solid loading at 100 s^{-1} shear rate were around 260, 180, and 160 mPa·s with the use of SL, PBMA, and NSF as the dispersant, respectively. Meanwhile, the apparent viscosities of slurry samples for 50 wt % solid loading at the same shear rate were around 750, 420, and 220 mPa·s with SL, PBMA, and NSF respectively. Notably, the apparent viscosities of both solid loadings were below 800 mPa·s. Furthermore, at 1000 s^{-1} shear rate, the apparent viscosity was below 200 mPa·s for 40 wt % solid loading, while for 50 wt % solid loading, its value was from 130 to 230 mPa·s and within the viscosity range for diesel engine applications (<300 mPa·s).⁷

On the other hand, varying the type of dispersants affected the apparent viscosity at an increasing shear rate. NSF had the most significant effect on the reduction of apparent viscosity followed by PBMA and then SL. PBMA is an amphiphilic polymer containing both hydrophobic groups ($-\text{CH}_2-$) and hydrophilic groups ($-\text{COOH}$). SL and NSF were also amphiphilic with hydrophilic groups such as sulfonic, carboxyl, and phenolic hydroxyl. When dispersants were mixed with the multiphase slurry samples, the hydrophilic groups adsorb onto the hydrophobic surface of hydrochar particles through hydrophobic interaction. Once adsorption was completed the hydrophilic groups could change their orientation to the water and change the hydrophobic surface of the hydrochar to a hydrophilic one. This could cause a steric and electrostatic repulsion between the hydrochar particles, resulting in a reduction in surface tension followed by apparent viscosity.³⁰ Compared with SL and PBMA, NSF appeared to have the best functional groups and adsorption onto the hydrochar surface for the reduction in apparent viscosity.

Table 2 below summarizes the flow behavior indexes of hydrochar slurry samples with 40 and 50 wt % solid loadings, which were stabilized by different dispersants. The indexes were derived from the power-law model in eq 1 and fitted to the shear stress with respect to the shear rate in Figure 4. From Table 2, it was found that the flow behavior indexes of all

Table 2. Flow Behavior Index of the Hydrochar Slurry

solid loading (wt %)	flow behavior index, n		
	SL	NSF	PBMA
40	0.50	0.57	0.47
50	0.55	0.62	0.57

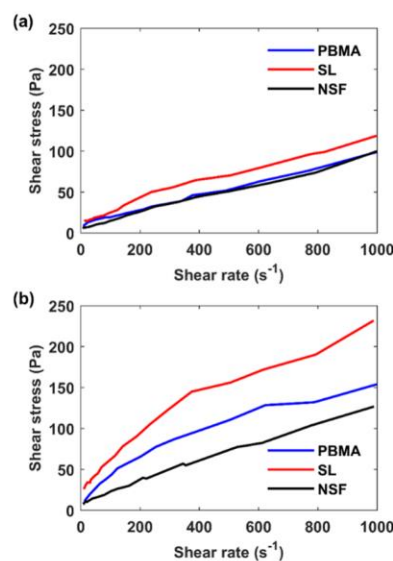


Figure 4. Effect of three dispersants, that is, SL, NSF, and PBMA, at 1 wt % loading on the shear stress of hydrochar–water slurry fuels with the increasing shear rate for (a) 40 wt % solid loading and (b) 50 wt % solid loading.

slurry samples were less than unity. This means that the flow is pseudo-plastic in character and this flow property is desirable for slurry fuel applications in boilers, gasifiers, and diesel engines.^{6,28}

3.4. Characterization of Hydrochar Slurry Droplets under Radiation Heating.

Figure 5 depicts the representative images of heated hydrochar slurry droplets with the NSF dispersant at different solid loadings under the radiation of 1.92 and 0.74 MW/m². To characterize the slurry droplets under radiation heating, the hydrochar particles milled for 30 min were used to prepare the hydrochar slurry. Based on this figure, it is observed that the ignition first happened on the droplet surface, which is highlighted in a red circle. The samples with 50 wt % solid loading were found to be ignited faster and required a lower flux to ignite compared to the samples with 40 wt % solid loading. For example, under a radiation flux of 1.92 MW/m², a surface ignition was first observed at about 0.38 s for the sample with 50 wt % solid loading, while for 40 wt % solid loading, the surface ignition time was delayed to about 0.9 s. Apart from this, under a flux radiation of 0.74 MW/m², only 50 wt % slurry can be ignited, as shown in Figure 5c,d. The increasing surface ignition time of the 40 wt % slurry was because of the larger heat capacity of water than solid fuels. According to Glushkov et al.,³¹ the heat required in water vaporization is 10 times higher than the heat required in the devolatilization of solid fuels. Therefore, the higher water content could reduce the heating rate of the hydrochar slurry and extend the surface ignition time. It should be noted that the accuracy of time measurement was affected by the imaging delay of the digital camera. Because of the maximum imaging delay of the visual camera being 0.02 s, the

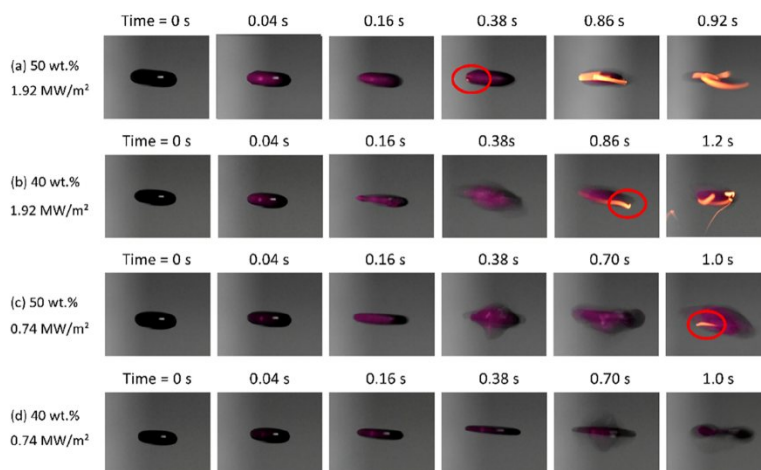


Figure 5. Representative time-resolved imaging of the levitated hydrochar slurry droplets with 50 and 40 wt % solid loadings irradiated by radiation of 1.92 and 0.74 MW/m². The special positions of the surface ignition are indicated by red circles.

uncertainty in the surface ignition time could be ± 0.01 s before the first ignition image was recorded. For example, for the droplet with 50 wt % solid loading under a radiation flux of 1.92 MW/m², the surface ignition was first recorded at 0.38 s. Considering the imaging delay, its surface ignition time can be further determined at 0.37 ± 0.01 s.

Additionally, the ignition was always first observed on the left-hand side of the slurry samples, as circled in Figure 5a, located at the radiation-incident side. The shape of the slurry was changed along with the heating process. This change in shape might be caused by the decrease in the surface tension. The surface tension of water fell by about 15% for every temperature increase of 100 K,³² which permitted the slurry droplet to be flattened into a thin sheet, as shown in the images after 0.16 s. When the slurry temperature rose further the shape oscillation was observed, resulting in the unsteady spinning of the droplet. This oscillatory spin tended to be enhanced by further reducing surface tension and water evaporation.³²

Figure 6a shows the time-resolved surface temperature (T^{surf}) measured for 40 and 50 wt % hydrochar slurries samples under the radiation fluxes of 1.92 and 0.74 MW/m². The radiation flux and solid loading both influenced the temperature increases and subsequent heating processes. Three heating processes, that is, (I) the initial fast-heating process within the first 0.2 s, (II) the following transition heating process, and (III) the final heating process caused by surface ignition, are clearly defined in the figure. Once the radiation was turned on, the slurry temperature experienced the first step increase within the first 0.2 s, which was caused by water vaporization, then the temperature's rate of increase declined. With the prolonged heating time, a second step increase of the slurry temperature was observed once the water contained in the slurry completely vaporized and the surface ignition occurred immediately after that. It should be noted that the 50 wt % slurry droplets were quickly ignited under a high radiation flux, and therefore, the transition heating process is much shorter than others and hard to identify.

Figure 6b,c shows the heating rates of slurry droplets as a function of time and temperature, respectively, for 50 and 40 wt % slurry droplets under different heating fluxes. The heating rates were derived from the temperature profiles shown in Figure 6a. According to Figure 6b, a slight change in the flux

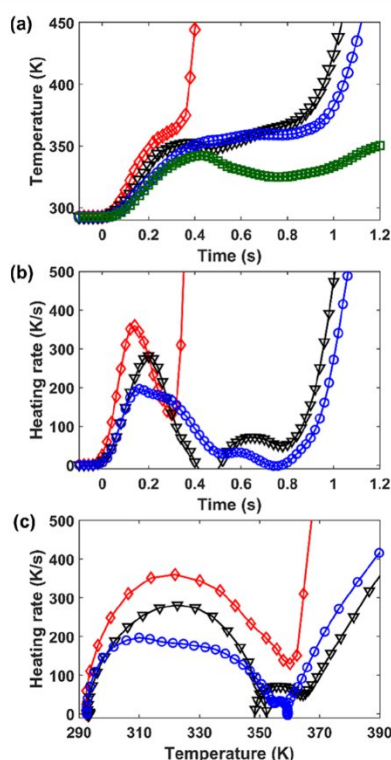


Figure 6. (a) Time-resolved temperature profiles of levitated hydrochar slurry droplets under the radiation fluxes of 1.92 and 0.74 MW/m²; The heating rates of the droplets under radiation as a function of (b) time and (c) droplet temperature. —◇— 50 wt %, 1.92 MW/m², —○— 50 wt %, 0.74 MW/m², —▽— 40 wt %, 1.92 MW/m², and —□— 40 wt %, 0.74 MW/m².

can significantly influence the heating rate of fuels. The surface heating rate (k^{surf}) was measured to be 400 and 200 K/s using the heating flux of 1.92 and 0.74 MW/m², respectively. Comparing the 50 and 40 wt % droplets under the same radiation flux, the decline in moisture content led to an obvious increase in the heating rate within the first fast-heating process because of the HHV values increasing. The rising rate

of heating under radiation heating can promote the following thermal decomposition of the hydrochar slurry.

Figure 6c depicts the relationship between the heating rate and surface temperature of the droplet (T^{surf}). According to the change in the heating rate, the temperature region of each heating process can be identified. The initial fast-heating process ranged from room temperature to around 320 K. The transition heating process was identified as existing between 320 and 360 K, where the heating rate declined as the temperature increased. The final heating process was observed after 360 K. The heating rate's steep increase in this process was caused by the heating of solid hydrochar and following surface ignition. As the change in the heating rate for different droplets occurred at similar positions, the identified temperature region for each heating process is independent of solid loading and heat flux.

Figure 7 shows a typical example of the association between representative visual images that appear in Figure 5, with the

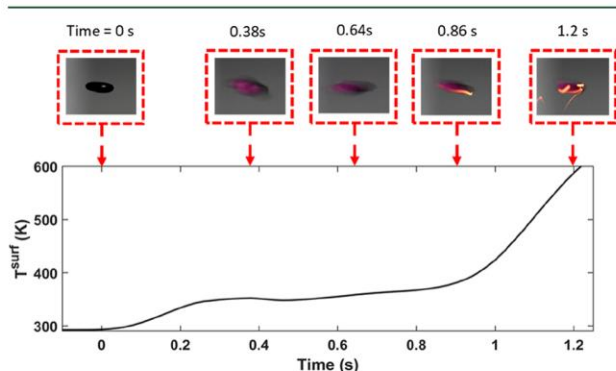


Figure 7. Typical example of the time-resolved temperature profile, with corresponding optical images, of levitated slurry droplets (40 wt %) and irradiated with a radiation flux of 1.92 MW/m².

corresponding time-resolved temperature profile in Figure 6a based on heating time. The example shown in Figure 7 is for a 40 wt % hydrochar slurry droplet heated under a radiation flux of 1.92 MW/m². In the visual image, the first surface ignition was observed at around 0.86 s, only tens of milliseconds after the beginning of the second step increase, and its corresponding temperature was determined to be 375 ± 15 K in the temperature profile. Therefore, this second step increase in the temperature profiles can be used to identify the $T_{\text{ig}}^{\text{surf}}$ of the droplet. According to Figure 6a, the second step

increase in different droplets occurred at a similar position; thus, the $T_{\text{ig}}^{\text{surf}}$ of hydrochar slurry droplets can be further confirmed at around 375 K, independent of heat flux. The accuracy of the surface temperature measurement was affected by the spatial resolution of the IR camera.

Table 3 compares the viscosity and ignition parameters under external heating of different types of fuels, including hydrochar slurry, coal, solid hydrochar, heavy fuel oil, coal–water slurry, and biochar–water slurry. From this table, the $T_{\text{ig}}^{\text{surf}}$ of the hydrochar slurry is very similar to heavy oil but slightly lower than that of the coal–water slurry. This phenomenon could be triggered by the high volatile matter contents in hydrochar and heavy oil.³³ Because volatile matters are released after water vaporization and produce combustible gases during combustion, the fuel with a high volatile matter content can be easily ignited and with a high burning rate. Similar behavior has been observed in other studies.^{33,34} Besides, compared with solid fuels, such as coal and hydrochar, the presence of water can decrease the ignition temperature of slurry fuels. This is because the thermochemical interaction between solid fuels and water vapor can support the combustion of carbon residues.^{21,31} The lower $T_{\text{ig}}^{\text{surf}}$ of hydrochar slurry provides evidence of its high fuel reactivity, which can reduce the O₂ concentration required during combustion.³⁴ The mixing of the hydrochar slurry with low volatile content fuels can also be expected to reduce the ignition temperature and assist the ignition, especially for the fuels which require an ignition enhancer during combustion.

On the other hand, the IR camera was used to detect the temperature on the exposed surface of droplets. Therefore, the $T_{\text{ig}}^{\text{surf}}$ measured in this work might be lower than the ignition temperature measured using thermocouples or TGA methods, which relied on the average ignition temperature of the bulk samples.³⁴

The heating rate of the fuel is limited by the heating source. The maximum heating rate of hydrochar slurry droplets under radiation heating was estimated at 400 K/s, which was much higher than that heated by TGA or hot air in reactors. This outcome suggests that high-flux radiation heating is more efficient at heating samples. Using a high-flux radiation system is a practical way to simulate the heating behaviors of fuels in a real combustion environment, where the fuel samples can be immediately heated up to a temperature around 1000 K in reactors.¹⁹

Additionally, the faster surface ignition of the hydrochar slurry observed in this work might also be caused by spinning

Table 3. Comparison of Viscosities and Ignition Parameters Under External Heating of the Hydrochar Slurry, Coal, Solid Hydrochar, Heavy Fuel Oil, Coal–Water Slurry, and Biochar–Water Slurry

fuel	fuel loading (%)	viscosity at shear rate of 100 s ⁻¹ (mPa·s)	HHV (MJ/kg)	surface ignition temperature (K)	surface ignition time (s)	heating rate of fuel (K/s)	heating source	refs
hydrochar slurry	50	220	13	375	0.4–1	100–400	laser radiation (~1 MW/m ²)	This work
coal	100	N/A ^a	22	>375	n.d. ^b	<1	TGA (15 K/min)	34
solid hydrochar	100	N/A ^a	31	>375	n.d. ^b	<1	TGA (15 K/min)	33,34
heavy fuel oil	100	~1000	43	351–381	n.d. ^b	n.d. ^b	boiler (800 K)	31,35,36
coal–water slurry	50	100	16	385–400	7.9	~100	hot air in chamber (600–1000 K)	21,31,37
biochar–water slurry	50	<485	15	n.d. ^b	3.0	n.d. ^b	hot air in electric furnace (1023 K)	6,16,20

^aViscosity is not applicable for solid fuels. ^bNot determined.

the droplets. Because the droplet was spanned along the center axis in the levitator during radiation heating, it could mix with the surrounding air efficiently. The enhanced mixing of air with the hydrochar slurry droplets could lead to a significant increase in the surface O₂ concentration and as a result promote droplet ignition.

4. CONCLUSIONS

A hydrochar slurry has been developed by mixing hydrochar derived from the HTC of grape marc with water and dispersants. The experiment determined the rheological properties and the characterization of radiatively heated hydrochar slurry droplets under high-flux radiation. The HHV of hydrochar was measured to be 26.0 MJ/kg, which is similar to that of sub-bituminous coal and indicates its feasibility in fuel applications. With the 50 and 40 wt % hydrochar slurries, the HHVs were 13.0 and 10.4 MJ/kg, respectively. Compared with the dispersant of SL and PBMA, NSF had the best properties for the surface tension reduction of hydrochar particles and thus demonstrated the lowest apparent viscosity among the slurry samples investigated here. The flow behavior index of the hydrochar slurry was derived from the power-law model and determined to be less than unity for all samples. These low index values imply that the hydrochar slurry is pseudo-plastic, in which the flow property is desirable for liquid fuel applications. For the characterization of the hydrochar slurry under radiation heating, representative images of the hydrochar slurry droplets with 50 and 40 wt % solid loadings were recorded under the high-flux radiation of 1.92 and 0.74 MW/m². Three thermal processes, that is, initial fast-heating process, the subsequent transition heating process, and final heating process, were identified from the temporal temperature profiles, which were measured using an IR camera. A maximum surface heating rate (k^{surf}) of 50 wt % slurry droplets was measured above 400 K/s before ignition, and its surface ignition time was observed at 0.37 ± 0.01 s. The surface ignition temperature ($T_{\text{ig}}^{\text{surf}}$) of the hydrochar slurry was around 375 ± 15 K, independent of heat flux. These results suggest that the hydrochar slurry is a highly reactive biofuel. The use of the high-flux radiation system can efficiently heat the samples and is practical for stimulating the heating behaviors of fuels in a real combustion environment.

■ AUTHOR INFORMATION

Corresponding Authors

Chi Wai Kwong – School of Chemical Engineering and Advanced Materials, The University of Adelaide, Adelaide, South Australia 5005, Australia; Email: philip.kwong@adelaide.edu.au

Zeyad T. Alwahabi – School of Chemical Engineering and Advanced Materials and Centre for Energy Technology, The University of Adelaide, Adelaide, South Australia 5005, Australia; orcid.org/0000-0003-4831-7798; Email: zeyad.alwahabi@adelaide.edu.au

Authors

Wanxiang Zhao – School of Chemical Engineering and Advanced Materials and Centre for Energy Technology, The University of Adelaide, Adelaide, South Australia 5005, Australia; orcid.org/0000-0001-5916-9669

Jennifer Mary Howie – School of Chemical Engineering and Advanced Materials, The University of Adelaide, Adelaide, South Australia 5005, Australia

Zhiwei Sun – School of Mechanical Engineering and Centre for Energy Technology, The University of Adelaide, Adelaide, South Australia 5005, Australia; orcid.org/0000-0001-7899-9676

Complete contact information is available at:
<https://pubs.acs.org/10.1021/acs.energyfuels.0c02567>

Notes

The authors declare no competing financial interest.

■ ACKNOWLEDGMENTS

Support was received from the Australian Research Council (ARC) through the Discovery Project DP180102045. The authors would also like to acknowledge Dr. Philip van Eyk for providing the HTC facility and technical assistance.

■ REFERENCES

- (1) Benter, M. M.; Gilmour, I. A.; Arnoux, L. Biomass-oil slurry fuels: an investigation into their preparation and formulation. *Biomass Bioenergy* **1997**, *12*, 253–261.
- (2) Libra, J. A.; Ro, K. S.; Kammann, C.; Funke, A.; Berge, N. D.; Neubauer, Y.; Titirici, M.-M.; Fühner, C.; Bens, O.; Kern, J.; Emmerich, K.-H. Hydrothermal carbonization of biomass residuals: a comparative review of the chemistry, processes and applications of wet and dry pyrolysis. *Biofuels* **2011**, *2*, 71–106.
- (3) Kambo, H. S.; Dutta, A. A comparative review of biochar and hydrochar in terms of production, physico-chemical properties and applications. *Renew. Sustain. Energy Rev.* **2015**, *45*, 359–378.
- (4) Titirici, M.-M.; Funke, A.; Kruse, A. Hydrothermal Carbonization of Biomass. In *Recent Advances in Thermo-Chemical Conversion of Biomass*; Pandey, A., Bhaskar, T., Stöcker, M., Sukumaran, R. K., Eds.; Elsevier: Boston, 2015; pp 325–352.
- (5) Lane, D. J.; Truong, E.; Larizza, F.; Chiew, P.; de Nys, R.; van Eyk, P. J. Effect of Hydrothermal Carbonization on the Combustion and Gasification Behavior of Agricultural Residues and Macroalgae: Devolatilization Characteristics and Char Reactivity. *Energy Fuels* **2018**, *32*, 4149–4159.
- (6) Abdullah, H.; Mourant, D.; Li, C.-Z.; Wu, H. Bioslurry as a Fuel. 3. Fuel and Rheological Properties of Bioslurry Prepared from the Bio-oil and Biochar of Mallee Biomass Fast Pyrolysis. *Energy Fuels* **2010**, *24*, 5669–5676.
- (7) Liu, P.; Zhu, M.; Leong, Y.-K.; Zhang, Y.; Zhang, Z.; Zhang, D. An experimental study of the rheological properties and stability characteristics of biochar–algae–water slurry fuels. *Energy Sources, Part A* **2017**, *39*, 1581–1586.
- (8) Trinh, T. N.; Jensen, P. A.; Dam-Johansen, K.; Knudsen, N. O.; Sørensen, H. R.; Szabo, P. Properties of slurries made of fast pyrolysis oil and char or beech wood. *Biomass Bioenergy* **2014**, *61*, 227–235.
- (9) Abdullah, H.; Mediaswanti, K. A.; Wu, H. Biochar as a Fuel: 2. Significant Differences in Fuel Quality and Ash Properties of Biochars from Various Biomass Components of Mallee Trees. *Energy Fuels* **2010**, *24*, 1972–1979.
- (10) Yip, K.; Xu, M.; Li, C.-Z.; Jiang, S. P.; Wu, H. Biochar as a Fuel: 3. Mechanistic Understanding on Biochar Thermal Annealing at Mild Temperatures and Its Effect on Biochar Reactivity. *Energy Fuels* **2011**, *25*, 406–414.
- (11) Funke, A.; Ziegler, F. Hydrothermal carbonization of biomass: A summary and discussion of chemical mechanisms for process engineering. *Biofuels, Bioprod. Biorefin.* **2010**, *4*, 160–177.
- (12) Liu, Z.; Quek, A.; Kent Hoekman, S.; Srinivasan, M. P.; Balasubramanian, R. Thermogravimetric investigation of hydrochar-lignite co-combustion. *Bioresour. Technol.* **2012**, *123*, 646–652.
- (13) Islam, M. A.; Kabir, G.; Asif, M.; Hameed, B. H. Combustion kinetics of hydrochar produced from hydrothermal carbonisation of Karanj (*Pongamia pinnata*) fruit hulls via thermogravimetric analysis. *Bioresour. Technol.* **2015**, *194*, 14–20.

- (14) He, C.; Giannis, A.; Wang, J.-Y. Conversion of sewage sludge to clean solid fuel using hydrothermal carbonization: Hydrochar fuel characteristics and combustion behavior. *Appl. Energy* **2013**, *111*, 257–266.
- (15) Tremel, A.; Stemann, J.; Herrmann, M.; Erlach, B.; Spliethoff, H. Entrained flow gasification of biocoal from hydrothermal carbonization. *Fuel* **2012**, *102*, 396–403.
- (16) Liu, P.; Zhu, M.; Zhang, Z.; Leong, Y.-K.; Zhang, Y.; Zhang, D. Rheological behaviour and stability characteristics of biochar-water slurry fuels: Effect of biochar particle size and size distribution. *Fuel Process. Technol.* **2017**, *156*, 27–32.
- (17) Natarajan, V. P.; Suppes, G. J. Rheological studies on a slurry biofuel to aid in evaluating its suitability as a fuel. *Fuel* **1997**, *76*, 1527–1535.
- (18) Di Nola, G.; de Jong, W.; Spliethoff, H. TG-FTIR characterization of coal and biomass single fuels and blends under slow heating rate conditions: Partitioning of the fuel-bound nitrogen. *Fuel Process. Technol.* **2010**, *91*, 103–115.
- (19) Shen, L.; Wu, J.; Xiao, J.; Song, Q.; Xiao, R. Chemical-Looping Combustion of Biomass in a 10 kWth Reactor with Iron Oxide As an Oxygen Carrier. *Energy Fuels* **2009**, *23*, 2498–2505.
- (20) Zhu, M.; Zhang, Z.; Zhang, Y.; Liu, P.; Zhang, D. An experimental investigation into the ignition and combustion characteristics of single droplets of biochar water slurry fuels in air. *Appl. Energy* **2017**, *185*, 2160–2167.
- (21) Kijo-Kleczkowska, A. Combustion of coal–water suspensions. *Fuel* **2011**, *90*, 865–877.
- (22) Brenn, G.; Deviprasath, L. J.; Durst, F.; Fink, C. Evaporation of acoustically levitated multi-component liquid droplets. *Int. J. Heat Mass Transfer* **2007**, *50*, 5073–5086.
- (23) Zhao, W.; Sun, Z.; Alwahabi, Z. T. Contactless Thermal Diagnostics of Acoustically Levitated Biomass under Uniform High Flux Radiation. *Energy Fuels* **2020**, *34*, 530–534.
- (24) Saha, A.; Kumar, R.; Basu, S. Infrared thermography and numerical study of vaporization characteristics of pure and blended bio-fuel droplets. *Int. J. Heat Mass Transfer* **2010**, *53*, 3862–3873.
- (25) Benetto, E.; Jury, C.; Kneip, G.; Vázquez-Rowe, I.; Huck, V.; Minette, F. Life cycle assessment of heat production from grape marc pellets. *J. Cleaner Prod.* **2015**, *87*, 149–158.
- (26) Boie, W. Fuel technology calculations. *Energietechnik* **1953**, *3*, 309–316.
- (27) Alwahabi, Z. T.; Kueh, K. C. Y.; Nathan, G. J.; Cannon, S. Novel solid-state solar thermal simulator supplying 30,000 suns by a fibre optical probe. *Opt. Express* **2016**, *24*, A1444–A1453.
- (28) Marzo, A.; Barnes, A.; Drinkwater, B. W. TinyLev: A multi-emitter single-axis acoustic levitator. *Rev. Sci. Instrum.* **2017**, *88*, 085105.
- (29) Roy Choudhury, P. Slurry fuels. *Prog. Energy Combust. Sci.* **1992**, *18*, 409–427.
- (30) Huang, J.; Xu, J.; Wang, D.; Li, L.; Guo, X. Effects of Amphiphilic Copolymer Dispersants on Rheology and Stability of Coal Water Slurry. *Ind. Eng. Chem. Res.* **2013**, *52*, 8427–8435.
- (31) Glushkov, D. O.; Syrodoy, S. V.; Zhakharevich, A. V.; Strizhak, P. A. Ignition of promising coal-water slurry containing petrochemicals: Analysis of key aspects. *Fuel Process. Technol.* **2016**, *148*, 224–235.
- (32) Basu, S.; Saha, A.; Kumar, R. Criteria for thermally induced atomization and catastrophic breakup of acoustically levitated droplet. *Int. J. Heat Mass Transfer* **2013**, *59*, 316–327.
- (33) Muthuraman, M.; Namioka, T.; Yoshikawa, K. Characteristics of co-combustion and kinetic study on hydrothermally treated municipal solid waste with different rank coals: A thermogravimetric analysis. *Appl. Energy* **2010**, *87*, 141–148.
- (34) Saqib, N. U.; Baroutian, S.; Sarmah, A. K. Physicochemical, structural and combustion characterization of food waste hydrochar obtained by hydrothermal carbonization. *Bioresour. Technol.* **2018**, *266*, 357–363.
- (35) Barroso, J.; Barreras, F.; Ballester, J. Behavior of a high-capacity steam boiler using heavy fuel oil. *Fuel Process. Technol.* **2004**, *86*, 89–105.
- (36) Yaghi, B. M.; Al-Bemani, A. Heavy Crude Oil Viscosity Reduction for Pipeline Transportation. *Energy Sources* **2010**, *24*, 93–102.
- (37) Mishra, S. K.; Senapati, P. K.; Panda, D. Rheological Behavior of Coal-Water Slurry. *Energy Sources* **2002**, *24*, 159–167.


Chapter 7

Emissivity and Absorption Function Measurements of Al₂O₃ and SiC Particles at Elevated Temperature for the Utilization in Concentrated Solar Receivers

Statement of Authorship

Title of Paper	Emissivity and absorption function measurements of Al ₂ O ₃ and SiC particles at elevated temperature for the utilization in concentrated solar receivers
Publication Status	<input checked="" type="checkbox"/> Published <input type="checkbox"/> Accepted for Publication <input type="checkbox"/> Submitted for Publication <input type="checkbox"/> Unpublished and Unsubmitted work written in manuscript style
Publication Details	Wanxia Zhao, Zhiwei Sun, Zeyad T. Alwahabi. (2020) Solar Energy, 207, 183-191. DOI: 10.1016/j.solener.2020.06.079


Principal Author

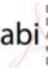
Name of Principal Author (Candidate)	Wanxia Zhao		
Contribution to the Paper	Performed experiments, analysed results, interpreted data and wrote manuscript.		
Overall percentage (%)	75		
Certification:	This paper reports on original research I conducted during the period of my Higher Degree by Research candidature and is not subject to any obligations or contractual agreements with a third party that would constrain its inclusion in this thesis. I am the primary author of this paper.		
Signature		Date	03/07/20

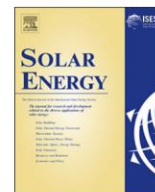
Co-Author Contributions

By signing the Statement of Authorship, each author certifies that:

- the candidate's stated contribution to the publication is accurate (as detailed above);
- permission is granted for the candidate to include the publication in the thesis; and
- the sum of all co-author contributions is equal to 100% less the candidate's stated contribution.

Name of Co-Author	Zhiwei Sun		
Contribution to the Paper	Assisted in experiments, discussed experimental results and findings, and revised the manuscript.		
Signature		Date	08/07/20

Name of Co-Author	Zeyad T. Alwahabi		
Contribution to the Paper	Discussed experimental results and findings, supervised the research project, and revised the manuscript.		
Signature	 Zeyad Alwahabi <small>Digitally signed by Zeyad Alwahabi DN: cn=Zeyad Alwahabi, o=University of Adelaide, ou, email=zeyad.alwahabi@adelaide.edu.au, c=AU Date: 2020.07.21 21:56:48 +0930'</small>	Date	21/07/2020



Emissivity and absorption function measurements of Al₂O₃ and SiC particles at elevated temperature for the utilization in concentrated solar receivers



Wanxia Zhao^{a,c}, Zhiwei Sun^{b,c}, Zeyad T. Alwahabi^{a,c,*}

^a School of Chemical Engineering and Advanced Materials, The University of Adelaide, SA 5005, Australia

^b School of Mechanical Engineering, The University of Adelaide, SA 5005, Australia

^c Centre for Energy Technology, The University of Adelaide, SA 5005, Australia

ARTICLE INFO

Keywords:

Optical properties
Solar particles
High temperature
Absorption function
Emissivity
Concentrated solar radiation

ABSTRACT

Solar thermal receivers collect and can store concentrated solar radiation using solid particles. Solid ceramic particles have shown to be a practical and efficient heat transfer media in solar-particle receivers, however, their emissivity and absorptivity at high temperatures are scarcely reported. This gap has led to large uncertainties in the assessment of solar thermal receivers' efficiency. In this work, an experimental method was developed to measure the emissivity and absorption function of solar particles at elevated temperatures up to 1200 K. Two types of solar particles, aluminum oxide (Al₂O₃, ~95% purity) and silica carbide (SiC, ~99% purity), were studied, particularly aiming to understand the dependence of emissivity and absorption function on temperature. Using a heat transfer model, the emissivity of particles was evaluated based on the fitting of the cooling rate, while the particle absorption function was obtained by fitting of the heating rate, following a well-controlled heating radiation at 910 nm. It was found that the emissivity values of the two particles are independent of temperature, showing constant values of 0.75 ± 0.015 and 0.92 ± 0.012 for Al₂O₃ and SiC respectively, in the temperature from 300 to 1200 K. The absorption function was found to be increased nonlinearly with temperature for Al₂O₃, while that of SiC dropped slightly. These absorption functions are specified for 910 nm. Using the evaluated experimental values of emissivity and absorption function, the maximum temperature and the temperature rise time of micro-sized particles (hundreds of micrometers) under different radiation fluxes were simulated taking into account the effect of particle diameter.

1. Introduction

Solid particles have been proposed as media for the absorption of concentrated solar radiation and the storage of heat. Examples of this are falling particle receivers (Ho et al., 2014), vortex particle receivers (Chinnici et al., 2015), fluidized-bed receivers (Zhang et al., 2015), and obstructed particle receivers with porous media (Lee et al., 2015). The usage of particles tolerant of high temperatures can increase the operating temperature of concentrated solar power (CSP) plants to above 800 °C, thus improving energy efficiency and lowering the cost of energy storage (Behar et al., 2013). In numerical assessments of the thermal efficiency of a receiver under design, the optical properties of particles including absorptivity and emissivity are of crucial importance since they are controlling factors in solar radiation harvesting and heat loss, respectively. However, the absorptivity and emissivity of typical solar particles at high temperature have been rarely reported and remain the main sources of uncertainty in numerical simulation of

concentrated solar-particle receivers.

Röger et al. (2011) and Gobereit et al. (2015) evaluated numerically the performance and efficiency of a falling particle receiver system. The emissivity of dark-grey colored particles was assumed to be 0.93, independent of wavelength or temperature. Chen et al. (2006) modeled the thermal behavior of gas-particle flow inside a solid particle receiver. The emissivity of solid particles was treated as a constant value of 0.8, independent of temperature. Flamant (1982) measured the total emissivity (spectrally averaged) of fluidized beds of different micro-sized particles (diameter = 250 μm) under solar radiation, including zirconia, silica carbide, silica sand, and chamotte. Diago et al. (2018) investigated the optical properties of sand and evaluated the performance of concentrated solar particle receivers. The results indicated that emissivity decreases with increasing temperature. Compared with experimental results, their numerical values show obvious underestimation, particularly when the equilibrium temperature is higher than 573 K.

* Corresponding author at: School of Chemical Engineering and Advanced Materials, The University of Adelaide, SA 5005, Australia.

E-mail address: zeyad.alwahabi@adelaide.edu.au (Z.T. Alwahabi).

<https://doi.org/10.1016/j.solener.2020.06.079>

Received 18 March 2020; Received in revised form 16 June 2020; Accepted 21 June 2020

0038-092X/ © 2020 International Solar Energy Society. Published by Elsevier Ltd. All rights reserved.

Nomenclature		u	velocity of air with respect to the particle (m/s)
A_p	particle surface area (m ²)	<i>Subscripts</i>	
C_{abs}	absorption cross section of the particle (m ²)	abs	absorption
c_p	specific heat capacity of the particle (J/kg·K)	conv	convection
d	particle diameter (m)	p	particle
$E(m)$	absorption function	rad	radiation
\bar{h}	average convection heat transfer coefficient between air and particle (W/m ² ·K)	max	maximum
k	thermal conductivity (W/m·K)	<i>Greek letters</i>	
m	mass of the particle (kg)	$\frac{\partial T}{\partial t}$	temperature gradient with time (K/s)
\bar{Nu}	Nusselt number	ε	material emissivity
Pr	Prandtl number	μ_∞	dynamic viscosity of air at room temperature (kg/m·s)
q_{abs}	heat absorption rate by the particle (W)	μ_p	dynamic viscosity of air at particle surface temperature (kg/m·s)
$q_{conv,loss}$	heat loss rate from the particle by air convection (W)	ν	kinematic viscosity of air (m ² /s)
$q_{rad,loss}$	heat loss rate from the particle by hot surface radiation (W)	σ	Stefan-Boltzmann constant, 5.67×10^{-8} (W/m ² ·K ⁴)
Re	Reynolds number	Φ	heat flux (MW/m ²)
T_p	particle surface temperature (K)		
$T_{p,max}$	maximum particle temperature (K)		
T_∞	ambient temperature of the air, 296 (K)		

Regarding particle absorptivity, Klein et al. (2007) modeled the heat transfer process within a directly irradiated solar receiver using relatively small carbon black particles. They used Mie theory to calculate the absorption efficiency factor in which the complex refractive index of carbon black particles was assumed as that of soot particles at room

temperature (Dalzell & Sarofim, 1969). Röger et al. (2011) estimated the absorptance of particle curtain based on the reflectance (R) of the particle cloud and transmittance (T). The absorptance could be calculated with $1-(R + T)$, where R was assumed as a constant of 0.06, and T was dependent on the incidence angle of solar radiation. However, the

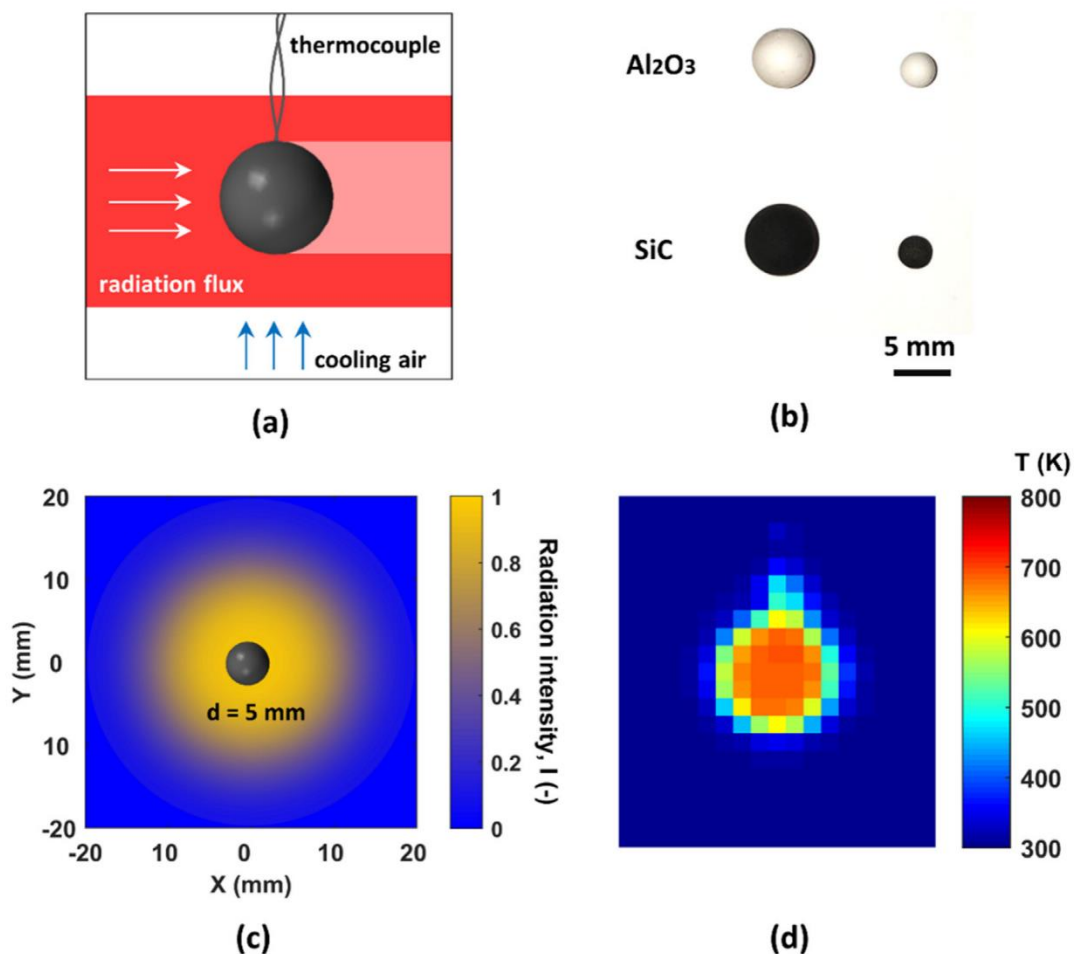


Fig. 1. (a) Schematic diagram of the experimental setup, (b) optical images of the particles studied, (c) illustration of a spherical particle under the uniform radiation, and (d) the uniform surface temperature of the particle imaged using an infrared camera.

effect of temperature on the particle optical properties was neglected. Ordóñez et al. (2014) investigated numerically the optimal optical properties of solar particles at high temperature in a non-homogeneous slab of particle dispersion that is composed of two-layers. They found that the optimized real part of the reflective index is 2, while the optimized imaginary part is spectrally dependent. The authors counted the non-uniform temperature field along light propagation but provided no information regarding the dependence of particle optical properties on temperature.

Different particles have been proposed and investigated under high operating temperatures in CSP particle receivers (Hellmann and McConnell, 1986; Siegel et al., 2014). Among these potential particles, ceramic particles show high absorptance, are low cost, and have long tolerance time (Ho, 2016). Aluminum oxide (Al_2O_3) and silica carbide (SiC) particles are two types of ceramic particles that are widely used in CSP plants because of their excellent thermal properties and high refractoriness (Tan and Chen, 2010). They have also been used as media in numerical simulation of CSP (Chen et al., 2006; Gomez-Garcia et al., 2017). However, no accurate emissivity or absorptivity data at high temperatures has been reported for these two materials.

Previously, solid particles from hundreds of micrometers to a few millimeters were chosen in experimental and numerical studies, e.g. 280 μm and 697 μm in falling particle receivers (Ho et al., 2017; Kim et al., 2009; Siegel et al., 2010), 1 mm in rotating kiln/centrifugal receivers (Wu et al., 2014), 250 μm in fluidized particle receivers (Flamant, 1982), and relatively large particles 1–3 mm in quartz-tube solid particle receivers (Zhang et al., 2015). Smaller particles are not preferable, likely due to safety concerns with particle egress or the high manufacture cost of fine particles. It is particularly important but very challenging to directly measure the thermal behaviors of these small particles (hundreds of micrometers) suspended in air and under high radiation flux. However, this information can be numerically accessible based on the heat-transfer model once the emissivity and the absorption function are accurately measured.

The absorption and emission properties of the particles' surface may change at high temperatures due to oxidation, material transformation, or both (Wang et al., 2015). The main objective of this work is to measure the absorption and emission properties of Al_2O_3 and SiC particles at high temperatures (up to 1200 K) to provide reliable values of emissivity and absorption function for the numerical modeling of CSP receivers. An experimental methodology was developed based on a heat transfer model of single particles in the presence of high radiation. The temperature rise time and equilibrium temperature (i.e. the achievable maximum temperature) of micro-sized (200 – 1000 μm) particles were also evaluated.

2. Experimental

Fig. 1(a) shows a schematic diagram of the experimental setup. A single spherical particle (approximately 3 and 5 mm) was hung using a thin thermocouple wire. The thin thermocouple wire had a small diameter of 76 μm (Omega, P13R-002) to minimize the heat loss through it, also enabling fast response for temperature measurements. The

accuracy of the thermocouple was within $\pm 0.25\%$. The junction tip of the thermocouple was glued into a small hole on the surface of the spherical particle with a depth of approximately 1 mm. The high flux radiation was provided by a solid-state radiation system using multiple diode lasers (Alwahabi et al., 2016). This solid-state radiation system provided a collimated laser beam peaking at a wavelength of 910 nm with a typical full width at half-maximum of 3.3 nm. The radiation system has a quick turn-on time of 15 ms, which is much shorter than the time scale at which particle temperature changes occur (see sections below) and the start-up time of most powerful lamps used in concentrated solar radiation simulators (Dong et al., 2015). The radiation field is uniform over an area of 10 mm in the central region. This area is larger than the size of the particles, ensuring that the entire spherical particle was irradiated under a uniform flux. The total radiation power was monitored, in real-time, by a power meter (Gentec model, HP100A-4KW-HE) located behind the measurement volume. The heat flux irradiated on the particle was calculated from the reduction of power when a particle was loaded on the measurement volume and the cross-section of the particle. The particle temperature was recorded at 50 Hz using a temperature data logger (Pico Technology, TC-08). An upward laminar airflow was supplied to provide a well-controlled boundary condition with different laminar gas velocities ranging from 0.35 to 2.13 m/s.

Fig. 1(b) shows the optical images of the particles studied in the present work (Latech Scientific Supply in Singapore), while Table 1 lists their physical properties and the specific heat capacities used in the following heat-transfer calculations. Fig. 1(c) presents the spatial profile of the radiation field related to an illustration of a 5 mm particle, showing that the radiation field is large enough to provide a uniform flux on the particle.

To verify the particle temperature is homogeneous, an infrared (IR) thermographic camera (VarioCAM HD, Jenoptik) was also employed to measure the surface temperature of the particle. The accuracy of temperature imaging with the infrared camera has been assessed in a previous work (Zhao et al., 2019), which is typically within $\pm 5\text{ K}$ in the temperature range of 300 to 800 K. As the spectral response range of the camera is from 7.5 to 14 μm , negligible interference is expected from the laser heating source to the infrared camera.

Fig. 1(d) presents an image of particle surface temperature measured using the infrared camera, showing a uniform temperature on the particle surface. Considering that only half of the particle surface was irradiated by the high-flux radiation, it is reasonable to assume that the particle is thermally equilibrated.

3. Derivation of emissivity and absorption function

Fig. 2 outlines a flowchart of the derivation process for the emissivity and absorption function. Briefly, the emissivity is derived from a fitting process conducted on the temperature profile of the particle under cooling after irradiation (i.e. the radiation was off). In the cooling process, the convection ($q_{\text{conv,loss}}$) and thermal radiation ($q_{\text{rad,loss}}$) are included in the heat transfer model. Then, the absorption function ($E(m)$) was derived from the heating process in which an absorption term

Table 1
Properties of the spherical particles used in the present investigation.

	SiC	Al_2O_3
Purity	> 99%	> 95%
Visual color	Dark grey to black	White
Particle diameter (mm)	2.60 and 5.83	3.13 and 4.90
Density (g/cm^3)	3.15	3.89
Thermal conductivity ($\text{W}/\text{m}\cdot\text{K}$)	120	35
Specific heat capacity ($\text{J}/\text{kg}\cdot\text{K}$)	$1026 + 0.20T - 3.66e^{-7}T^{-2a}$	$-40.9 + 4T - 5e^{-3}T^2 + 2.9e^{-6}T^3 - 6.2e^{-10}T^{4b}$

^a Karditsas and Baptiste (1995).

^b Touloukian and Buyco (1970).

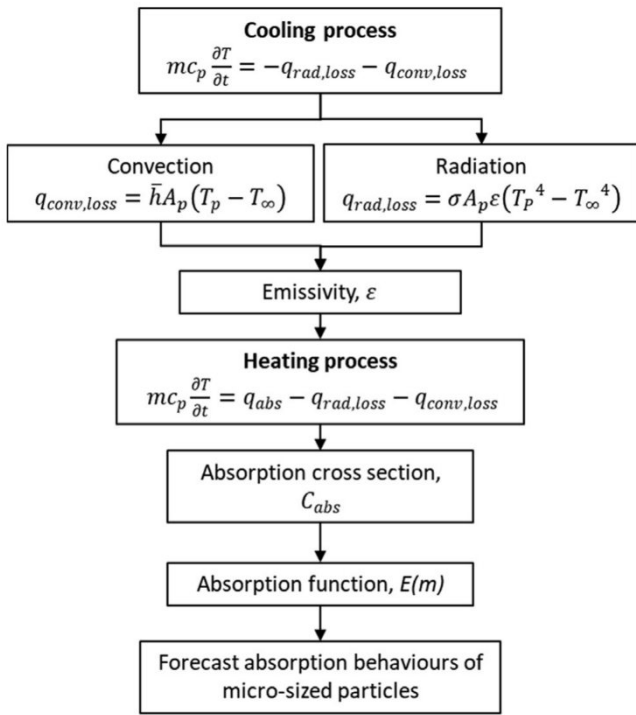


Fig. 2. Flowchart of the derivation process for the emissivity and absorption function of particles.

(q_{abs}) is also included in the heat transfer model.

For the cooling process, the energy balance can be described as follows (Holman, 2010):

$$mc_p \frac{\partial T}{\partial t} = -q_{rad,loss} - q_{conv,loss} \quad (1)$$

in which the convection heat loss, $q_{conv,loss}$, can be calculated using:

$$q_{conv,loss} = \bar{h}A_p(T_p - T_\infty) \quad (2)$$

The average convection heat transfer coefficient, \bar{h} , based on the surface area of the particle can be calculated by:

$$\bar{h} = \bar{Nu} \left(\frac{k}{d} \right) \quad (3)$$

For a spherical particle surrounded by a laminar flow, Whitaker (Whitaker, 1972) developed a single equation to calculate the Nusselt number, \bar{Nu} , as follows:

$$\bar{Nu} = 2 + (0.4Re^{1/2} + 0.06Re^{2/3})Pr^{0.4} \left(\frac{\mu_\infty}{\mu_p} \right)^{1/4} \quad (4)$$

where Pr equals 0.708 for air at ambient temperature. The equation (4) above is valid for a broad range of Re and Pr ($3.5 < Re < 8 \times 10^4$ and $0.7 < Pr < 380$). It is applied for the present investigation because all the air flows are laminar with Re values less than 665. The value of \bar{Nu} varies between 4 and 14 for the air flow rates in the present work. It is also noted that the temperature dependence of μ_p causes \bar{Nu} to be temperature-dependent according to Eq. (4).

The average convection heat transfer coefficient, \bar{h} , is determined between 49 and 109 W/m²·K depending on the velocity of cooling air. In addition, the Biot number was calculated for the particles studied in the present work using the physical property values shown in Table 1.

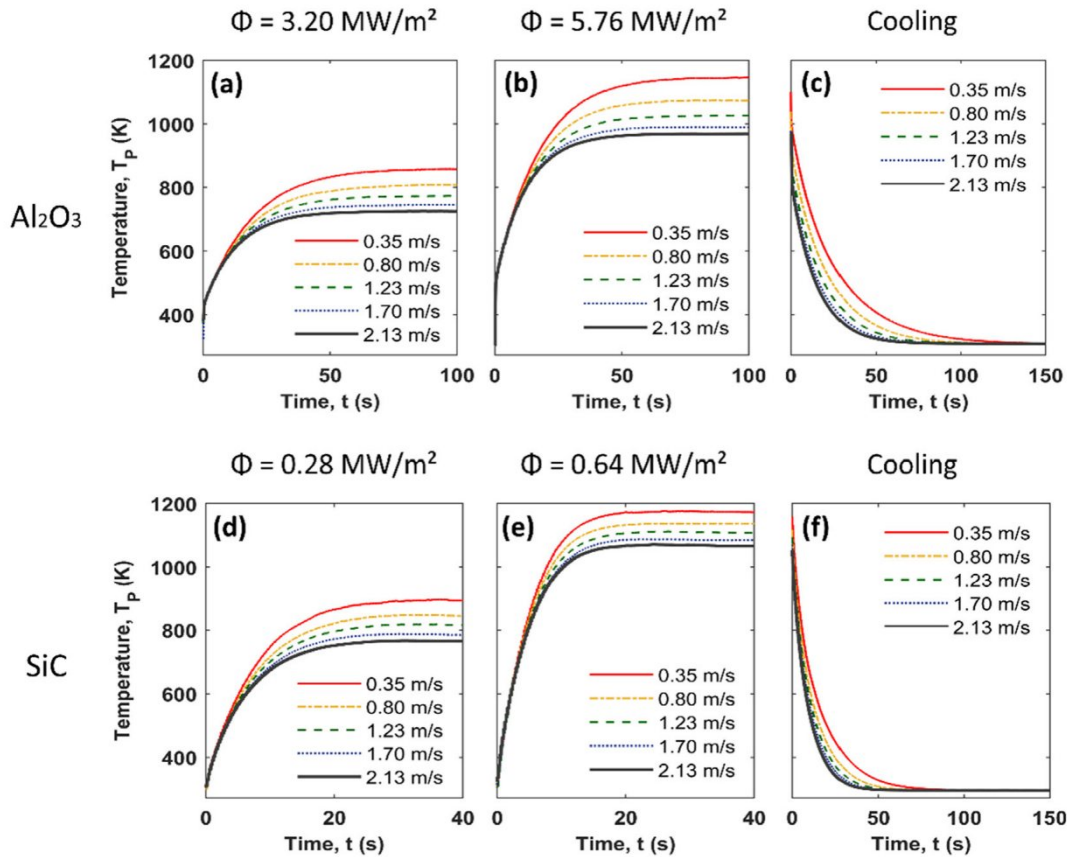


Fig. 3. Representative temperature profiles of Al₂O₃ and SiC particles measured using a thermocouple under the heating and cooling processes. Different airflow rates were supplied. The particle diameter is 3.13 mm and 2.60 mm for the Al₂O₃ and SiC particles, respectively.

The Biot number is from 0.001 to 0.005 for SiC particles and from 0.004 to 0.014 for Al₂O₃ particles, which are all much less than 0.1, further confirming the homogeneous temperature of the particles (Terekhov and Pakhomov, 2002; Souza-Santos, 2008).

The heat loss rate through thermal radiation, $q_{rad, loss}$, can be calculated using:

$$q_{rad, loss} = \sigma A_p \varepsilon (T_p^4 - T_{so}^4) \quad (5)$$

The value of emissivity ε can be derived by minimizing the divergence between the modeled and measured temperature profiles in the cooling process based on Eqs. (1)–(5).

An additional term, q_{abs} , is added into the energy balance equation (Eq. (1)) to count for the radiation absorption in the heating process:

$$mc_p \frac{\partial T}{\partial t} = q_{abs} - q_{rad, loss} - q_{conv, loss} \quad (6)$$

The radiation absorption rate can be expressed as (Bohren and Huffman, 2008):

$$q_{abs} = C_{abs} \Phi \quad (7)$$

According to Eqs. (6) and (7), the absorption cross section, C_{abs} , can be calculated as:

$$C_{abs} = (mc_p \frac{\partial T}{\partial t} + q_{rad, loss} + q_{conv, loss}) \times \frac{1}{\Phi} \quad (8)$$

in which the values of $\frac{\partial T}{\partial t}$ can be extracted from the measured temperature profile, while the values of $q_{rad, loss}$ and $q_{conv, loss}$ are calculated from the cooling process.

For the spherical particles studied, the criterion of $\pi d/\lambda \gg 1$ is fully met and the absorption cross section can be calculated as follow (Bohren and Huffman, 2008):

$$C_{abs} = \pi d^2 E(m) \quad (9)$$

From Eq. (9), the absorption function $E(m)$ can be calculated, which is a material-specific parameter and independent of the particle diameter.

The measurement uncertainties of emissivity and absorption were derived from (1) the standard deviation of the values measured at different radiation fluxes, (2) the uncertainty of the thermocouple ($\pm 0.25\%$), and (3) the R² values from the fitting of temperature profiles.

4. Results and discussion

4.1. Particle temperature evolution

Fig. 3 presents the time-resolved temperature profiles of the two particles measured using the thermocouple under different radiation fluxes and air flows. It can be seen that the maximum temperature (i.e. equilibrium temperature) and the temperature rise time are both sensitive to the radiation flux, the air flow rate, and the material. A high signal-to-noise ratio was also achieved for the measured temperatures. This suggests the methodology is very sensitive to the experimental parameters that were controlled. A significant difference between the two materials is the radiation flux needed to achieve a high temperature. The white Al₂O₃ particle needs a flux of approximately one order of magnitude higher than that of the black SiC particle to achieve the same maximum temperature, suggesting that SiC has a much higher absorptivity than Al₂O₃. However, the two particles exhibited similar cooling rates although those of the SiC particle were faster. This suggests the emissivity between the two materials is not significantly different. The temperature of the Al₂O₃ particle rose rapidly over 400 K (within 1 s) immediately after the radiation was turned on. This may be attributed to the non-thermal equilibrium of the particle under a shock of high flux radiation. This small part of the experimental data was excluded in the fitting process for evaluating $E(m)$. This rapid rising phenomenon was found to be negligible for SiC particles because of the use of significantly lower fluxes. The temperature evolution curves are repeatable in the measurement, while Al₂O₃ particle showed a slightly higher temperature when it was heated up to a higher temperature for the first time.

4.2. Particle emissivity, ε

Fig. 4 shows the measured and modeled temperatures of two particles cooling down from different maximum temperatures under different air flow rates. The maximum temperatures were used as an input in the modeling. An excellent agreement can be seen between the measured and modeled results, validating the accuracy of the methodology developed in the present work. Particularly noting that it was assumed that the emissivity is constant and independent of temperature in the modeling. Fig. 4 validates this assumption because the modeled results agree well with those measured over a large temperature range from room temperature up to 1000 K.

Fig. 5 shows the values of emissivity for Al₂O₃ and SiC particles derived from the cooling process starting from different maximum

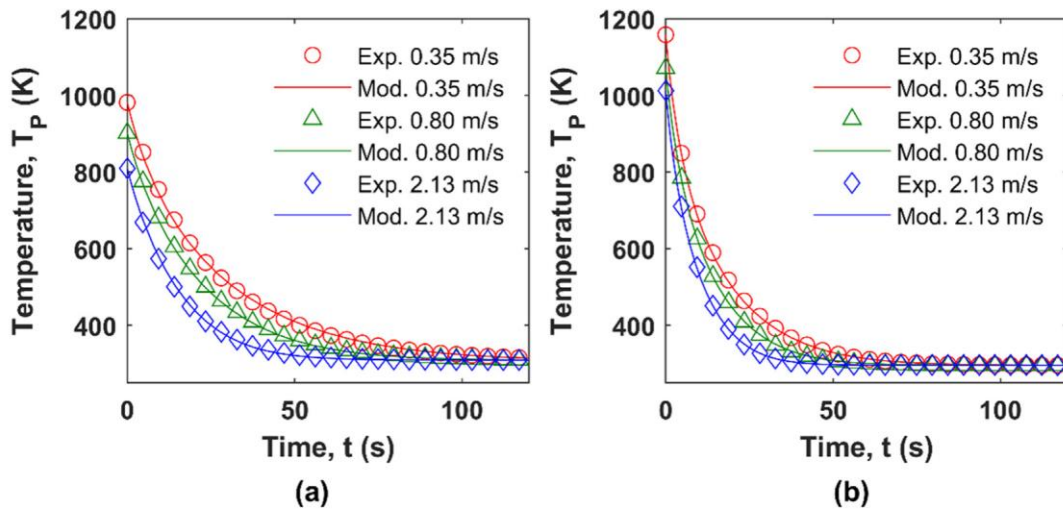


Fig. 4. Representative measured and modeled temperature profiles of (a) an Al₂O₃ ($d = 3.13$ mm) particle and (b) a SiC ($d = 2.60$ mm) particle under the cooling process from different maximum temperatures and at different surrounding air flow rates.

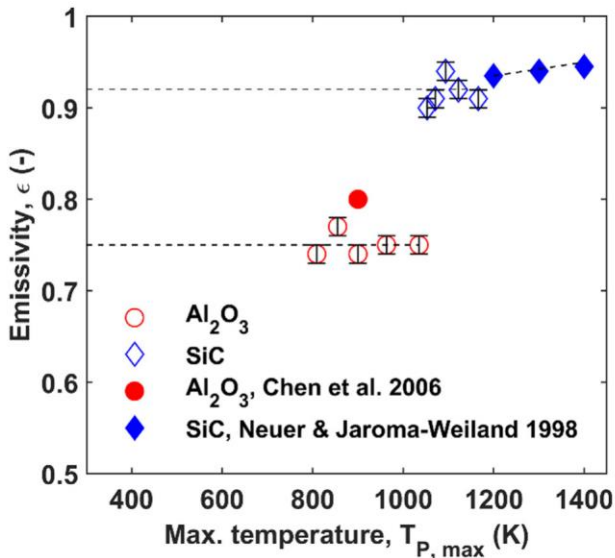


Fig. 5. Emissivity of Al₂O₃ and SiC measured at high temperature.

temperatures (Fig. 3(c) and (f)). While the values of emissivity are plotted as a function of the particle maximum temperature in Fig. 5, it should be noted that these values are valid for all the temperatures from $T_{p, \max}$ to room temperature, as discussed above. The values of emissivity derived from different maximum temperatures agree well with each other as shown in Fig. 5, further confirming that the material emissivity is independent of temperature up to 1200 K. An average value of 0.75 ± 0.015 and 0.92 ± 0.012 was calculated for Al₂O₃ and SiC, respectively. These values agree with results reported previously (Chen et al., 2006; Neuer and Jaroma-Weiland, 1998) which are also shown in Fig. 5.

4.3. Particle absorption function, $E(m)$

Fig. 6 presents the absorption cross sections (C_{abs}) measured for the particles at different radiation fluxes. It can be found that the values of C_{abs} are consistent for each particle at different temperatures,

corresponding to different radiation fluxes. Interestingly, the two materials exhibit significantly different dependencies of C_{abs} on temperature. For Al₂O₃, the values of C_{abs} remain approximately constant in the temperature range below 700 K and increases greatly with the temperature until 1200 K. Conversely, C_{abs} for SiC decreases slightly with increasing temperature. These results indicate that it is highly necessary to consider the effect of temperature on particle absorption capabilities in the assessment of radiation harvesting. It should also be noted that the values of C_{abs} for white Al₂O₃ are lower than those of black SiC by more than one order of magnitude.

Fig. 7 presents the values of $E(m)$ as a function of temperature. The values were calculated from the results shown in Fig. 6 based on Eq. (10). The values measured for two particles with different diameters agree well with each other, validating the d^2 law for light absorption by spherical particles (see Eq. (9)). The absorption function of the black SiC is approximately 10 times larger than that of Al₂O₃. A polynomial fit applied to the results shown in Fig. 7 results in the following temperature-dependent absorption function for the two materials:

$$\text{Al}_2\text{O}_3: E(m) = 3.49 \times 10^{-15}T_p^4 + 9.74 \times 10^{-3} \tag{10}$$

$$\text{SiC}: E(m) = 5.28 \times 10^{-8}T_p^2 - 1.3 \times 10^{-4}T_p + 0.27 \tag{11}$$

The absorption functions are determined with a confidence level of 95%. The coefficient of determination, R-squared, is 0.993 for the absorption equation of Al₂O₃ particles and 0.921 for the absorption equation of SiC particles. It should be noted that these absorption functions are not spectrally integrated but specified for 910 nm. However, the values may be still applicable in the relevant applications as the solar irradiance are dominant in visible and near-infrared regions. In addition, these measurements clearly demonstrate the significant dependence of the absorption function on temperature.

Fig. 8 presents representative measured and modeled temperature profiles of Al₂O₃ and SiC particles during the heating process at three different radiation fluxes. Good agreement between the measured and modeled temperature profiles validate the accuracy of the absorption functions derived in the present work. It also validates the accuracy of the heat transfer model, which was then used to predict the thermal behaviors (the temperature rise time and maximum temperature) of micro-sized spherical particles under high flux radiation (Section 4.4 below).

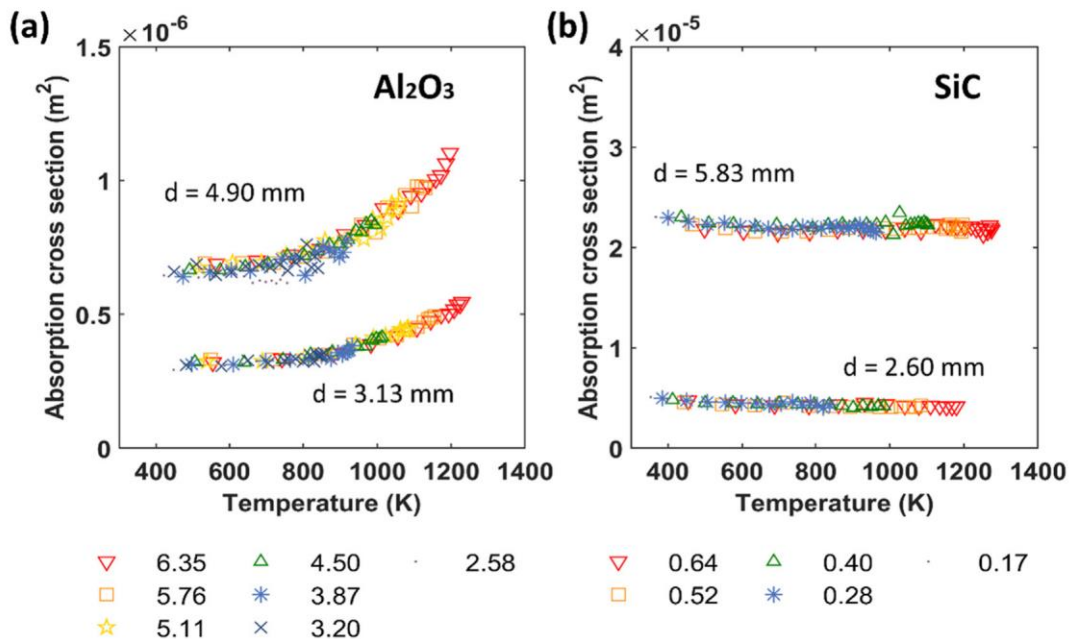


Fig. 6. Absorption cross section of (a) Al₂O₃ and (b) SiC particles at two different diameters as a function of temperature under different radiation fluxes in units of MW/m². The airflow velocity was kept as constant (0.05 m/s).

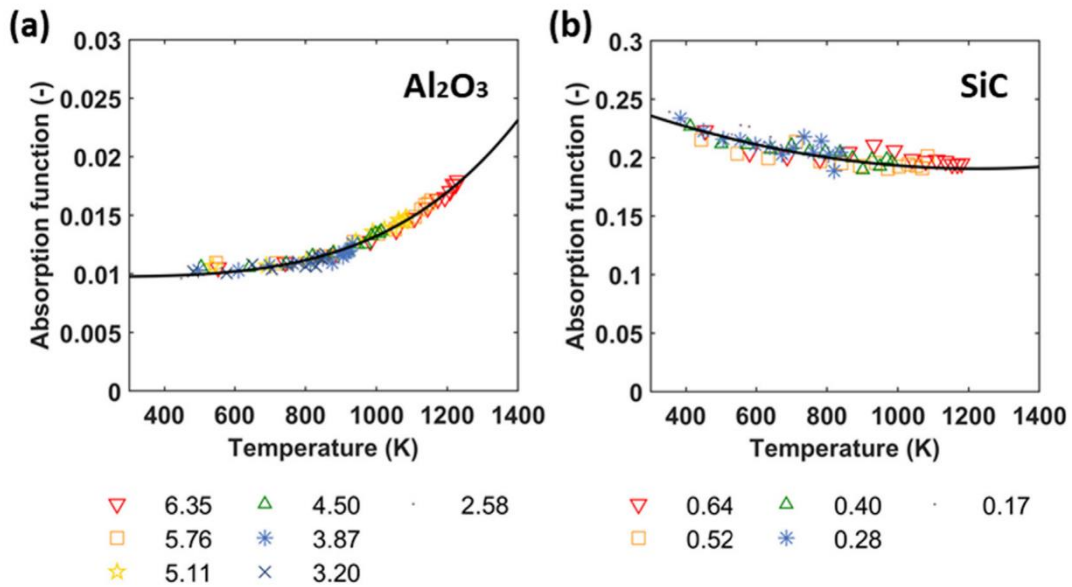


Fig. 7. Absorption function $E(m)$ of (a) Al_2O_3 and (b) SiC as a function of temperature. Symbols are experimental results measured at different radiation fluxes (MW/m^2) and a constant airflow velocity of 0.05 m/s , while the black lines are polynomial fits of the experimental results.

4.4. Thermal behaviors of micro-sized particles under high flux radiation

Fig. 9 shows the maximum temperature and temperature rise time of micro-sized ($200\text{--}1000 \mu\text{m}$) particles under different radiation fluxes. For these small particles, the thermal behaviors are challenging to be measured and no result has been reported. Therefore, they are numerically evaluated based on the emissivity and absorption function derived from the millimeter-sized particles (*c.a.* 3 and 5 mm) above.

Fig. 9(a) and (c) show a consistent trend of the maximum temperature as functions of radiation flux and particle size ($200\text{--}1000 \mu\text{m}$). A higher maximum temperature is more easily achieved for large particles than small particles under the same radiation flux. In addition, just like millimeter-sized particles, micro-sized SiC particles only need approximately 10% of the radiation flux to reach a similar maximum temperature as micro-sized Al_2O_3 particles with the same diameter. This is because SiC has much higher $E(m)$ values than Al_2O_3 , while there is no significant difference in specific heat capacity and emissivity between these two materials.

However, significantly different trends were found between the

temperature rise time as shown in Fig. 9(b) and (d). This rise time is defined as the time needed to heat the micro-sized particle to 98% of the maximum temperature. Interestingly, the temperature rise time changes differently as a function of radiation flux for micro-sized Al_2O_3 and SiC particles. Micro-sized Al_2O_3 particles prefer a low radiation flux to quickly reach their maximum temperatures. Conversely, micro-sized SiC particles prefer a high radiation flux to quickly achieve their maximum temperatures. This different trend is mainly due to the different absorption properties of the two materials (Fig. 7), where SiC has a higher probability to absorb heat. It should be clarified that Fig. 9(b) does not mean micro-sized Al_2O_3 particles can be heated up faster at a low flux than at a high flux because the maximum temperature varies with the radiation flux.

5. Conclusions

The emissivity and absorption function of Al_2O_3 and SiC at high temperature were experimentally studied to provide reliable fundamental optical data of these two materials in the modeling of solar-

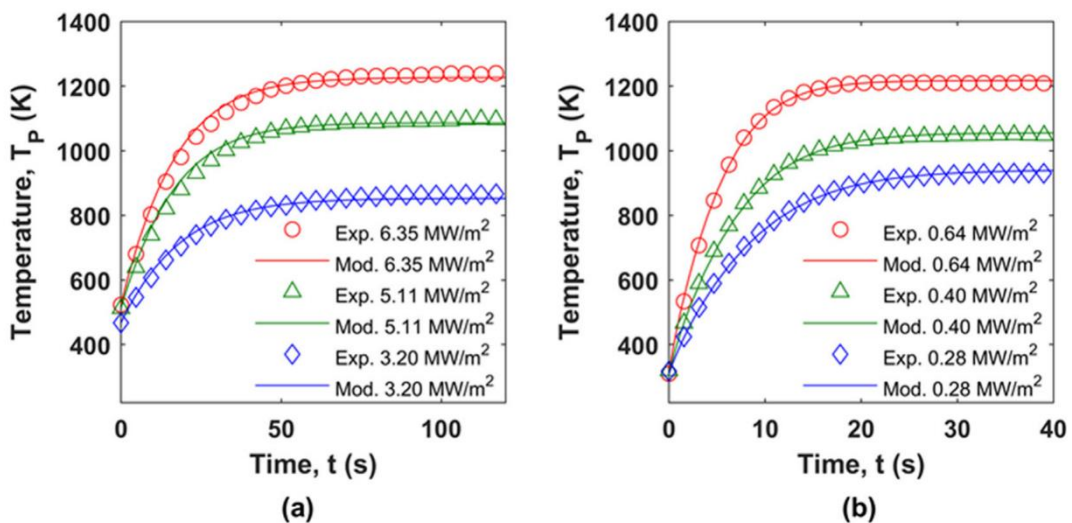


Fig. 8. Representative measured and modeled temperature profiles for (a) an Al_2O_3 ($d = 3.13 \text{ mm}$) particle and (b) a SiC ($d = 2.60 \text{ mm}$) particle under the heating process at different radiation fluxes. The airflow velocity was kept constant as 0.05 m/s .

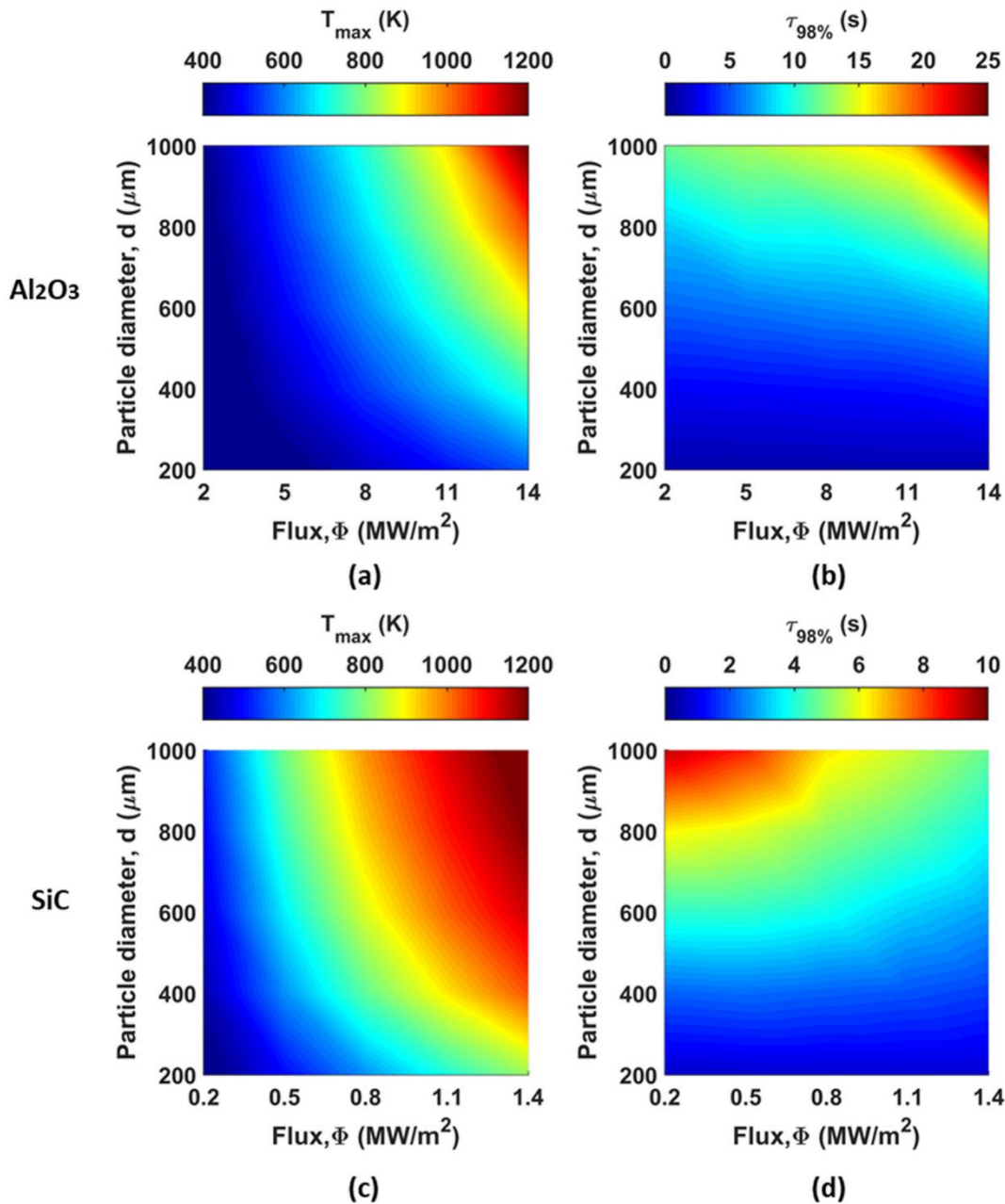


Fig. 9. (a) and (c) maximum temperature achievable for micro-sized Al_2O_3 and SiC particles of different diameters; (b) and (d) the time that is needed to heat the particles above 98% of the corresponding maximum temperature.

particle receivers. It was found that emissivity is insensitive to temperature for both materials and values of 0.75 ± 0.015 for Al_2O_3 and 0.92 ± 0.012 for SiC are applicable for a broad temperature range from room temperature to around 1200 K. However, the absorption function $E(m)$, which is specified for 910 nm, varies with temperature for both materials, but the dependencies are different. The absorption function of Al_2O_3 increases significantly with temperature when it is over 800 K, while that of SiC only slightly decreases with temperature. In addition to the value of $E(m)$ results obtained, it was shown that the temperature dependence of particle absorptivity must be considered in modeling solar-particle receivers at high temperature, rather than simply assuming a single value. The modeling results of micro-sized particles indicate that the temperature rise time (heating rate) of the two materials have significantly different dependencies on the radiation flux, which is attributed to their different absorption capabilities.

Declaration of Competing Interest

The authors declare that they have no known competing financial interests or personal relationships that could have appeared to influence the work reported in this paper.

Acknowledgments

This research is supported by the Australian Research Council (ARC) through a Discovery Project (DP180102045).

References

- Alwahabi, Z.T., Kueh, K.C., Nathan, G.J., Cannon, S., 2016. Novel solid-state solar thermal simulator supplying 30,000 suns by a fibre optical probe. *Opt. Express* 24 (22), 1444–1453.
- Behar, O., Khellaf, A., Mohammedi, K., 2013. A review of studies on central receiver solar

- thermal power plants. *Renew. Sustain. Energy Rev.* 23, 12–39.
- Bohren, C.F., Huffman, D.R., 2008. *Absorption and Scattering of Light by Small Particles*. John Wiley & Sons, New York.
- Chen, H., Chen, Y., Hsieh, H.-T., Siegel, N., 2006. Computational fluid dynamics modeling of gas-particle flow within a solid-particle solar receiver. *J. Sol. Energy Eng.* 129 (2), 160–170.
- Chinnici, A., Arjomandi, M., Tian, Z.F., Lu, Z., Nathan, G.J., 2015. A novel solar expanding-vortex particle reactor: influence of vortex structure on particle residence times and trajectories. *Sol. Energy* 122, 58–75.
- Dalzell, W.H., Sarofim, A.F., 1969. Optical constants of soot and their application to heat-flux calculations. *J. Heat Transfer* 91 (1), 100–104.
- Diago, M., Iniesta, A.C., Soum-Glaude, A., Calvet, N., 2018. Characterization of desert sand to be used as a high-temperature thermal energy storage medium in particle solar receiver technology. *Appl. Energy* 216, 402–413.
- Dong, X., Nathan, G.J., Sun, Z., Gu, D., Ashman, P.J., 2015. Concentric multilayer model of the arc in high intensity discharge lamps for solar simulators with experimental validation. *Sol. Energy* 122, 293–306.
- Flamant, G., 1982. Theoretical and experimental study of radiant heat transfer in a solar fluidized-bed receiver. *AIChE J.* 28 (4), 529–535.
- Gobereit, B., Amsbeck, L., Buck, R., Pitz-Paal, R., Röger, M., Müller-Steinhagen, H., 2015. Assessment of a falling solid particle receiver with numerical simulation. *Sol. Energy* 115, 505–517.
- Gomez-Garcia, F., Gauthier, D., Flamant, G., 2017. Design and performance of a multi-stage fluidised bed heat exchanger for particle-receiver solar power plants with storage. *Appl. Energy* 190, 510–523.
- Hellmann, J.R., McConnell, V.S., 1986. *Characterization of Spherical Ceramic Particles for Solar Thermal Transfer Media: A Market Survey*. Sandia National Labs, Albuquerque, NM.
- Ho, C., Christian, J., Gill, D., Moya, A., Jeter, S., Abdel-Khalik, S., Sadowski, D., Siegel, N., Al-Ansary, H., Amsbeck, L., Gobereit, B., Buck, R., 2014. Technology advancements for next generation falling particle receivers. *Energy Procedia* 49, 398–407.
- Ho, C.K., 2016. A review of high-temperature particle receivers for concentrating solar power. *Appl. Therm. Eng.* 109, 958–969.
- Ho, C.K., Christian, J.M., Romano, D., Yellowhair, J., Siegel, N., Savoldi, L., Zanino, R., 2017. Characterization of particle flow in a free-falling solar particle receiver. *J. Sol. Energy Eng.* 139 (2), 021011.
- Holman, J.P., 2010. *Heat Transfer*, 10th ed. McGraw-Hill series in mechanical engineering, New York.
- Karditsas, P.J., Baptiste, M.-J., 1995. *Thermal and structural properties of fusion related materials*. UKAEA Government Division, Fusion, Culham, UK.
- Kim, K., Siegel, N., Kolb, G., Rangaswamy, V., Moujaes, S.F., 2009. A study of solid particle flow characterization in solar particle receiver. *Sol. Energy* 83 (10), 1784–1793.
- Klein, H.H., Karni, J., Ben-Zvi, R., Bertocchi, R., 2007. Heat transfer in a directly irradiated solar receiver/reactor for solid-gas reactions. *Sol. Energy* 81 (10), 1227–1239.
- Lee, T., Lim, S., Shin, S., Sadowski, D.L., Abdel-Khalik, S.I., Jeter, S.M., Al-Ansary, H., 2015. Numerical simulation of particulate flow in interconnected porous media for central particle-heating receiver applications. *Sol. Energy* 113, 14–24.
- Neuer, G., Jaroma-Weiland, G., 1998. Spectral and total emissivity of high-temperature materials. *Int. J. Thermophys.* 19 (3), 917–929.
- Ordóñez, F., Caliot, C., Bataille, F., Lauriat, G., 2014. Optimization of the optical particle properties for a high temperature solar particle receiver. *Sol. Energy* 99, 299–311.
- Röger, M., Amsbeck, L., Gobereit, B., Buck, R., 2011. Face-Down Solid Particle Receiver Using Recirculation. *J. Sol. Energy Eng.* 133 (3), 031009.
- Siegel, N., Gross, M., Ho, C., Phan, T., Yuan, J., 2014. Physical properties of solid particle thermal energy storage media for concentrating solar power applications. *Energy Procedia* 49 (1), 1015–1023.
- Siegel, N.P., Ho, C.K., Khalsa, S.S., Kolb, G.J., 2010. Development and evaluation of a prototype solid particle receiver: on-sun testing and model validation. *J. Sol. Energy Eng.* 132 (2).
- Souza-Santos, M.L.d., 2008. *Analytical and Approximate Methods in Transport Phenomena*. CRC Press, Boca Raton.
- Tan, T., Chen, Y., 2010. Review of study on solid particle solar receivers. *Renew. Sustain. Energy Rev.* 14 (1), 265–276.
- Terekhov, V.I., Pakhomov, M.A., 2002. Numerical study of heat transfer in a laminar mist flow over a isothermal flat plate. *Int. J. Heat Mass Transf.* 45 (10), 2077–2085.
- Touloukian, Y., Buyco, E., 1970. *Thermophysical properties of matter, the TPRC data series vol. 5, specific heat: nonmetallic solids*. IFI/Plenum, New York, Washington.
- Wang, F., Cheng, L., Xie, Y., Jian, J., Zhang, L., 2015. Effects of SiC shape and oxidation on the infrared emissivity properties of ZrB₂-SiC ceramics. *J. Alloy. Compd.* 625, 1–7.
- Whitaker, S., 1972. Forced convection heat transfer correlations for flow in pipes, past flat plates, single cylinders, single spheres, and for flow in packed beds and tube bundles. *AIChE J.* 18 (2), 361–371.
- Wu, W., Amsbeck, L., Buck, R., Waibel, N., Langner, P., Pitz-Paal, R., 2014. On the influence of rotation on thermal convection in a rotating cavity for solar receiver applications. *Appl. Therm. Eng.* 70 (1), 694–704.
- Zhang, Y., Bai, F., Zhang, X., Wang, F., Wang, Z., 2015. Experimental study of a single quartz tube solid particle air receiver. *Energy Procedia* 69, 600–607.
- Zhao, W., Sun, Z., Alwahabi, Z.T., 2019. Contactless thermal diagnostics of acoustically levitated biomass under uniform high flux radiation. *Energy Fuels* 34 (1), 530–534.

Chapter 8

Conclusions and Future Works

8.1 Conclusions

In conclusion, a uniform and well-controlled radiation flux, provided by the multi-diode laser system, has been successfully utilized to investigate the thermal characteristics, heat transfer, and optical properties of particles, tablets, aggregates, and droplets. These targets were suspended in space using a variety of techniques, including fluidization, acoustic levitation, and hanging on very thin thermocouples. Furthermore, epoxy has been used for non-thermal scattering investigation of BAM and ZnO:Zn phosphors suspensions.

Fluidized beds can be utilized to suspend a large number of small particles and aggregates whose sizes are in micron ranges. They provide rapid and uniform mixing of particles in the reactors. However, the particles loading in the fluidized bed is difficult to control. As the particles can constantly moving, their residence time is short. Epoxy resin can be used to suspend particles homogeneously. The particle loading can be well-controlled. The transparent nature of epoxy allows the radiation to pass through the suspended particles. Although this method is practical to investigate the non-thermal radiation scattering of static particle suspensions, it cannot be used in studies related to radiation heating or mobile particles. Acoustic levitators are efficient to suspend both solid particles and droplets in space. Any physical contact can be avoided to eliminate the influences of unnecessary conductive heat transfer. They are relatively simple to fabricate and can be easily combined with an external heating source. However, its levitation ability is limited by the power supply voltage. In this thesis, the acoustic levitator was successfully to suspend objects with a diameter less than 4 mm and a density up to 2.2 g/cm³. Furthermore, once levitated, the particle will be continuously spinning in space around the vertical axis with an angular frequency of approximately 7 rounds per second. This spin might also cause the shape oscillation of small droplets under radiation heating. To suspend particles with higher density, thin thermocouple wires attached to the particles may be utilized. These thin wires, less than

100 μm in diameter, enable fast response for temperature measurements under high-flux radiation. Their small diameters can minimize the heat loss through the thermocouple during radiation heating. However, this method can only be used to perform non-spatial temperature measurements of static solid targets. Besides, the heat transfer between the thermocouple and targets cannot be eliminated. The measurement accuracy is affected by the thermal conductivity of the materials.

Chapter 3 investigated the *in-situ* temperature imaging of fluidized BAM phosphor aggregates under high flux radiation. To perform the non-intrusive temperature measurements of suspended aggregates in a multiphase flow, the planar laser-induced phosphorescence technique was employed to record the single-shot temperature imaging of fluidized BAM aggregates under high-flux radiation using an ICCD camera. The average temperature of mobile BAM aggregates was found to vary from 404 to 723 K as the heat flux was increased from 4.48 to 28.87 MW/m^2 . The maximum temperature of single aggregates of 1063 K was found to be much higher than the maximum temperature of 650 K that was recorded using ZnO:Zn phosphors. The averaged and maximum aggregates temperature increased linearly with increasing the radiation flux by a factor of 14.7 and 25.5, respectively. The probability distribution of all measured aggregate temperatures over 300 images was described by gamma distribution under each flux. The dependence of aggregates temperature to heat flux was consistent with expected trends, thus providing further confidence that the temperature imaging method reported in this paper is reliable to measure the temperature of mobile particles in multiphase flow.

Chapter 4 investigated the non-thermal radiation trapping of BAM and ZnO:Zn phosphor suspensions at room temperature using a combined experimental and numerical approach. The accurate characterization of optical properties and scattering distributions are required to understand the heat transfer within particle-suspension flows. Optical properties

also play an important role in the modeling of scattering and secondary heating of the processes. In this work, the optical properties, including scattering albedo, asymmetry factors of each forward and backward peak, and scattering fraction, were derived from the developed collision-based Monte Carlo ray-tracing model. The experimental results of scattering distribution showed good agreement with the Monte Carlo ray-tracing model. With the void fraction around 0.98, the extinction coefficient of ZnO:Zn phosphors was 4.719, while that of F grade BAM phosphors and N grade BAM phosphors were 11.584 and 9.777, respectively. In addition, BAM phosphors also had a higher scattering fraction ($\alpha = 0.99$) than ZnO:Zn phosphors ($\alpha = 0.88$). Due to the higher values of extinction coefficient and scattering fraction, BAM phosphors had more significant scattering behavior than ZnO:Zn phosphors. In the prediction of radiation density transferred along the direction of the radiation path, 70% of net heat flux was scattered by ZnO:Zn phosphors when the radiation distance increases to 0.5, while for BAM phosphors, the same scattering behavior was found at the distance around 0.15. Stronger scattering behaviors were observed on the particles with smaller sizes. The method and optical properties presented in this study can be applied to investigate the radiative heat transfer in other different particle-suspension-involved systems.

Chapter 5 investigated the time-resolved temperature profiles of acoustically levitated biomass tablets under high-flux radiation. To overcome the limitation of complex heat conduction between the sample and the holder in traditional methods, an acoustic levitator was employed in this thesis to suspend biomass tablets in space and to avoid any undesired conductive heat transfer caused by physical contact. Time-resolved temperature profiles of radiatively-heated biomass particles were accurately measured using a thermographic camera with a high spatio-temporal resolution. Three different thermal processes were reliably identified, which are the initial fast-heating process within 1 s, the secondary slow-heating process from 1 to 3 s, and the final ignition starting at 3 s. The

heating rate was evaluated from the temporal profile of the temperature measured. The ignition temperature of biomass tablets was around 430 to 450 K. The acoustic levitation system can also be applied to other small tablets, e.g., solid wastes and liquid droplets, and has the potential to be combined with other measurement methods, e.g., a gas analyzer for biomass.

Chapter 6 investigated the characterization of radiatively-heated hydrochar slurry droplets which were derived from hydrothermal carbonization of grape marc. Its rheological properties were measured experimentally. Its combustion properties under high-flux radiation were determined by suspending the droplets in space using an acoustic levitator. The higher heating value of hydrochar was measured to be 26.0 MJ/kg, which is similar to that of sub-bituminous coal. The flow behavior index of hydrochar slurry was determined to be less than unity for all samples. The low index values imply that the hydrochar slurry is pseudo-plastic and desirable for liquid fuel applications. Representative images of hydrochar slurry samples with 50 wt.% and 40 wt.% solid loadings were recorded under the high-flux radiation of 1.92 and 0.74 MW/m². Three thermal processes were identified from the temporal temperature profiles. The maximum heating rate of 50 wt.% slurry droplets were measured above 400 K/s before ignition and its surface ignition time was observed at 0.37 ± 0.01 s. The surface ignition temperature of hydrochar slurry was around 375 ± 15 K. The results imply that hydrochar slurry is a highly reactive biofuel. The use of the high-flux radiation system can efficiently heat the samples and is practical to simulate the heating behaviors of fuels in the real combustion environment.

In **Chapter 7**, the emissivity and absorption function of Al₂O₃ and SiC particles at high temperature have been determined. The emissivity and absorption function of Al₂O₃ and SiC particles were experimentally studied in this thesis to provide reliable fundamental optical data for solar-particle receivers. The values of emissivity were determined to be 0.75 ± 0.015 for Al₂O₃ and 0.92 ± 0.012 for SiC from room temperature to around 1200 K,

independent of temperature. The absorption function $E(m)$, which was specified for 910 nm, of Al_2O_3 increased significantly with temperature when it was over 800 K, while that of SiC only slightly decreased with temperature. The modeling results of micro-sized particles indicate that the temperature rise-time of the two materials have significantly different dependencies on the radiation flux, which is attributed to their different absorption capabilities.

Table A1 shown in **Appendix** summarizes all techniques and parameters used in each measurement, together with the measured properties and key results that have already been placed in our papers for publication.

In summary, the multi-diode laser system, which provides a uniform and well-controlled radiation flux, has been successfully applied to demonstrate the radiation heating of particles, aggregates, tablets, and droplets. Laser, optical, and conventional techniques are utilized to reliably record the temperature change in the target bodies, determine the thermal characteristics such as heating rates, and investigate the heat transfer process and optical properties of the selected targets. The outcomes obtained from these works offer the fundamental knowledge to the studies of heat-related processes and advance the understanding of heat transfer involved in high-temperature reactions.

8.2 Future works

Although considerable contributions have been made to knowledge in the application of well-controlled radiation with thermal and optical diagnostics, the following aspects could still be suggested in further research.

Firstly, the application of the multi-diode laser system utilized in this thesis can be extended to other thermal processes that require intense heat as energy sources. For example, the solar thermochemical process of hydrogen production is a high-temperature endothermic reaction derived from a concentrated solar reaction. The thermodynamic analysis of such processes can be investigated in the future to evaluate their thermal and chemical efficiencies. In addition, for high-temperature reactors, the main drawback of the fluidized bed utilized in this thesis is the short residence time of particles, which is caused by the short moving path of particles within the heating region. Also, the particles can easily escape from the system with air, leading to a decreasing in mass loading in the experiment. Therefore, using vortex reactors can be considered in further works. With the design of their rotating cavity and small aperture, particles in the reactor can reach both an extended residence time and a higher temperature as a result of the longer moving path and the more concentrated radiation compared to the fluidized bed. The long residence time also makes the particles feasible to meet the high-temperature requirement within a shorter time. The closed cavity also avoids the undesired particle loss in the experiment.

Secondly, the acoustic levitation system has the potential to be applied to other small objects and combined with different diagnostic techniques for *in-situ* element analysis. For example, laser-induced breakdown spectroscopy (LIBS) is a suitable option to simultaneously detect multi-elements on the surface of the targets. As an acoustic levitator can be easily combined with an external laser and well control the position of the targets, it is applicable to assisting the LIBS elements detection and increasing the measurement accuracy. This technique can be applied to both liquid and solid objects. It is especially important for applications that require fast chemical element analysis with limited sample volumes.

Finally, computational modeling and calculation can be introduced to simulating the morphological changes of targets under radiation heating and characterizing the related thermal effects. As the total volume and mass of the solid biomass tablets decrease during gasification, the shrinking of biomass may affect the heating and cooling rates of the table layers, the reaction time, and the production yields. Furthermore, clear shape oscillations have been observed on acoustically levitated fuel droplets in this thesis, which are caused by the reducing surface tension and water evaporation during radiation heating. This shape oscillation can be modeled by taking various liquid properties, such as viscosity, aspect ratio, and Bernoulli pressure, into consideration. Therefore, developing kinetic models for shape changes, coupled with the heat transfer model, has the potential to improve the understanding of the overall progress of complex thermal reactions such as gasification in future research. It is also important in the design of industrial units.

Appendix

Table A1: Thesis summary

<i>Research targets</i>	<i>Suspension methods</i>	<i>Radiation parameters (wavelength/flux)</i>	<i>Measurement techniques</i>	<i>Measured quantities</i>	<i>Key findings</i>	<i>Paper number</i>
Phosphor aggregates (BAM)	Fluidized bed	910 nm / 0 - 28.87 MW/m ²	<ul style="list-style-type: none"> Planar laser-induced phosphorescence ICCD camera 	<ul style="list-style-type: none"> Single-shot temperature image Average and maximum aggregates temperature Temperature probability distribution 	<ul style="list-style-type: none"> Maximum temperature of single aggregates: 1063 K The average temperature under high flux: 723 K The linear increasing factor of temperature against radiation flux: 14.7 for average aggregates temperature; 25.5 for maximum aggregates temperature The particle temperature distribution under heating flux: Gamma distribution The factors determining temperature distribution: Temperature of cooling air, the surface of aggregates, and airflow inside the fluidized bed 	Paper I: Chapter 3
Phosphors (BAM and ZnO:Zn)	Epoxy resin	No heating	<ul style="list-style-type: none"> Spectro-goniometric scattering Monte Carlo ray-tracing model 	<ul style="list-style-type: none"> Scattering albedo Extinction coefficient Scattering phase function Scattering radiation distribution 	<ul style="list-style-type: none"> Extinction coefficient: 4.719 (ZnO:Zn), 11.584 (F grade BAM), 9.777 (N grade BAM) Scattering fraction: 0.88 (ZnO:Zn), 0.99 (BAM) The distance of 70% net heat flux scattered: 0.5 (ZnO:Zn), 0.15 (BAM) 	Paper II: Chapter 4
Biomass tablets	Acoustic levitation	910 nm / 0.51 – 1.08 MW/m ²	<ul style="list-style-type: none"> IR thermometry 	<ul style="list-style-type: none"> Time-resolved temperature profile Heating rate Ignition time Ignition temperature 	<ul style="list-style-type: none"> Identification of three different thermal processes Ignition temperature: 430 to 450 K Ignition time: 3 s 	Paper III: Chapter 5
Hydrochar slurry droplets	Acoustic levitation	910 nm / 0.74 and 1.92 MW/m ²	<ul style="list-style-type: none"> IR thermometry 	<ul style="list-style-type: none"> Time-resolved temperature profile Time-resolved heating rate Ignition time Ignition temperature Combustion behavior image 	<ul style="list-style-type: none"> Higher Heating Values: 26.0 MJ/kg The maximum heating rate of 50 wt.% slurry: 400 K/s Surface ignition time: 0.37 ± 0.01 s Ignition temperature: 375 ± 15 K 	Paper IV: Chapter 6
Solid particles (Al ₂ O ₃ and SiC)	Hanged by thin thermocouples	910 nm / 0.17 – 6.35 MW/m ²	<ul style="list-style-type: none"> Thin thermocouple Heat transfer model 	<ul style="list-style-type: none"> Time-resolved temperature profile Emissivity Absorption function Maximum temperature of micro-sized particles Temperature rise-time of micro-sized particles 	<ul style="list-style-type: none"> Emissivity of Al₂O₃: 0.75 ± 0.015 Emissivity of SiC: 0.92 ± 0.012 The change of absorption function with temperature: Significant increase for Al₂O₃; Slight decrease for SiC Temperature rising time of micro-sized particles: Opposite behaviors shown by Al₂O₃ and SiC 	Paper V: Chapter 7